Rare-Event Searches with Bolometers

by

Alexander Friedrich Sebastian Leder

B.S., Louisiana State University and Agricultural and Mechanical College (2012)

Submitted to the Department of Physics
in partial fulfillment of the requirements for the degree of

Doctor of Philosophy

at the

MASSACHUSETTS INSTITUTE OF TECHNOLOGY

June 2018

Author ..... Signature redacted .....
Department of Physics
May 24,2018

Certified by..... Signature redacted .....
Lindley Winslow
Assistant Professor
Thesis Supervisor

Certified by... Signature redacted .....
Joseph Formaggio
Professor
Thesis Supervisor

Accepted by ..... Signature redacted .....
Scott A. Hughes
Interim Associate Department Head

Rare-Event Searches with Bolometers

by

Alexander Friedrich Sebastian Leder

Submitted to the Department of Physics
on May 24,2018, in partial fulfillment of the
requirements for the degree of
Doctor of Philosophy

Abstract

Rare-event searches have played an integral part in the pursuit of physics beyond the Standard Model, offering us the chance to bridge the disparity between our current understanding and observed phenomena such as Dark Matter (DM) or the nature of neutrino masses. Over the last 30 years, these experiments have grown larger and more sophisticated, allowing us to probe new and exciting theories of the universe. At the same time, we have started to apply the technologies and techniques used in rare-event searches to areas of applied physics, for example; reactor monitoring using Coherent Elastic Neutrino Nucleon Scattering (CEνNS) with Ricochet. In this thesis, I will discuss the hardware and analysis techniques required to design, construct, and extract results from these low background, rare-event searches. In particular, I will discuss the hardware and analysis related to the Cryogenic Dark Matter Search (CDMS), CEνNS detection with Ricochet and the measurement of the effective nuclear quenching factor g_a via shape analysis of the highly forbidden In-115 beta spectrum. The latter measurement has far reaching consequences for all neutrino-less double beta decay experiments, independent of isotope.

Thesis Supervisor: Lindley Winslow
Title: Assistant Professor

Thesis Supervisor: Joseph A. Formaggio
Title: Professor

Acknowledgments

They say it takes a village to finish a PhD and as I have been a part of three different experiments/collaborations throughout my time at MIT, I daresay I have stretched this expression quite far. Modern physics collaborations are often huge apparatuses with many support staff, graduate students, post-docs, researchers, PIs etc.... who together make all this research possible. Despite the large size of these collaborations, I never felt like just another name on a list and was always able to find a group of colleagues to whom I could turn to with my questions and discussions. I would need to a full thesis chapter to fully write up all the ways that all of you have made this thesis possible, but in short I am deeply indebted to all the people who helped me get to this point.

Firstly to all my advisors, thank you for taking me on, letting me work on all these different projects and learn from you all the while having faith in me, even when I did not always have it on hand. To Enectali Figueroa-Feliciano, the lessons I learned from you during those long nights on Waldorf have put me on a firm foundation that I will reap the rewards of for a long time to come. To Joesph Formaggio, your wisdom helped me tremendously throughout grad school, I would have never learned so much about neutrons in Geant4 without your help. To Lindley Winslow, thank you for trusting me with putting together Olaf and keeping me moving forward on all my various projects and for putting me on the right track to take the lead on the LIS analysis. I would not have been able to finish this thesis without your encouragement. I also want to thank the efforts of other facility members including Janet Conrad, Boleslaw Wyslouch and Krishna Rajagopal among others who mentored and advised me throughout my time at MIT.

A special acknowledgment also needs to go out to all the researchers and colleagues I had the pleasure of working with over these past six years. Starting with Julien Billard and Adam Anderson, no matter what group I end up in I will always strive to recreate that special mix of crazy, driven but always good hearted dynamic that we had. I learned so much during our "french-style" hour+ long lunch breaks, but most importantly I learned to always strive for that final ultimate goal of "physika!" no matter what the project/task at hand. I also want to say thank you to the CDMS/CDMSlite teams including Ritoban Basu Thakur, Mark Pepin, Dan Bauer and Paul Brink among many others for all their help and patience in getting me up and running. To our Micro-X neighbors next door in building 37: Sarah Trowbridge Heine, Meredith Danowski and David Goldfinger thank you for putting up with our antics, letting us "liberate" KF flanges (among other things...) and for always dispensing sage advice about cryogenics when things were about to take a turn for the worst. On the other side of the Atlantic, I wish to thank the Orsay CUORE/CUPID-Mo Group including Andrea Giuliani, Valentina Novati, Emiliano Olivieri, Denys Poda and Anastasiia Zolotarova for hosting me in Paris in 2016/2017 and for all their help in getting the LIS analysis off the ground, let me know if any of you want me to cook up another "American-style" thanksgiving for you all. To all the members of the Winslow group, from Diana Gooding sing-asking me if I wanted to build a snowman

every winter to Joe Johnston reintroducing me to Magic:The Gathering (I still refuse to play blue...) including Suzannah Fraker; Laura Gladstone;Julieta Gruszko and Chiara Salemi, I will deeply miss you all. In particular, I want to thank our post-doc, Jonathan Ouellet, for his guidance in getting me through all the intricacies of CUORE/Diana software and for making sure that I always accounted for all the errors in my analysis. There are also many many undergraduate researchers across all the various groups that I have worked in that helped make all this work possible including: Bridget Bohlin, Nick Deporzio, Eleanor Graham, Radha Mastandrea, Elise Newman, Mgcini Keith Phuthi, Chandler Schlupf, Lucy Zhang, good luck in all your future endeavors and thanks for always encouraging me with your unbridled enthusiasm for our work!

My friends during my time in graduate school were beyond amazing and in short I have never owed as much to a group of people as I owe them. The whole get-physical class of 2012 (Tom (good and bad), Jenny, Cody, Boris, James, Keaton, Alex among many others) I could not have made it through grad school without you and I will dearly miss you all. I am also so thankful for my experimental friends Gabriel, Nancy, John as well as my theoretical friends Lina and Jasmine who were always around with a helpful ear when things got rough and were always willing to try my cooking even when I might have added too much adobo sauce that one time... I have been fortunate to have had a long string of housemates and others at Ashdown who became good friends over the years: Junru, Mila, Stephen,Jason, Arghavan, Olivia and Andrea you all helped turn 3084 into a home. To my Louisiana friends: Nicole, Claire, James, Glynis, Sam and Snigdha y'all were always there when I had to complain to someone about the lack of good southern cooking up here in Boston. During my time here I have also been a part of two amazing organizations, the Tech Model Railroad Club and the Annihilation Operators Ice Hockey Team. Thank you for giving me an oasis when I needed to leave the lab to unwind, relax amongst friends and get pelted by hockey pucks/discuss the technical merits of Wagner verses Witte-type smoke deflectors on German steam locomotives.

I want to also thank the people who got me started on the path that has cumulated with this thesis. Wolfgang, who took me under his wing and brought me to my first physics colloquium at KIT (back then still called the University of Karlsruhe) and showed me that physics was so much more than just equations on a chalk board. Finally, to my parents whom I can not thank enough for always being there for me throughout my time here at MIT. You taught me to never stop asking questions and to always find the silver lining in any situation, this thesis is dedicated to you.

Contents

List of Figures

List of Tables

Chapter 1

Introduction to Rare-Event Searches

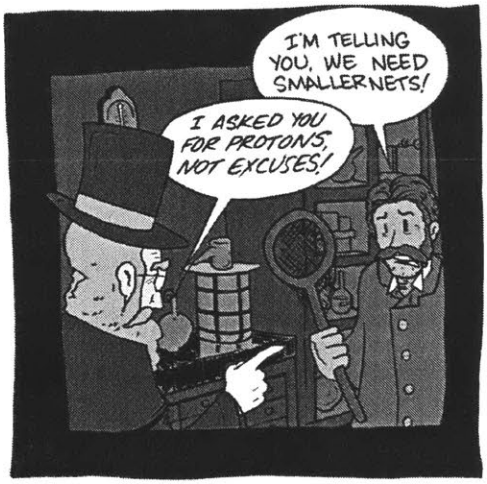

Particle physics has come a long way since the 1700s.

by Zach Weinersmith, smbc-comics.com, reproduced with permission

How does one detect a particle physics event? What sort of net should one use? Once you have caught a particle, how does one then go about proving that you understand what just happened inside your net? These are the questions that any experiment must answer. Fundamentally, one must first understand the hardware, specifically your detector, and how it responds to different physics events. Extracting just a single neutrino event, as shown in Figure 1-1, requires a deep understanding of the backgrounds that mask your signal coupled with the detector effects that can distort your signal.

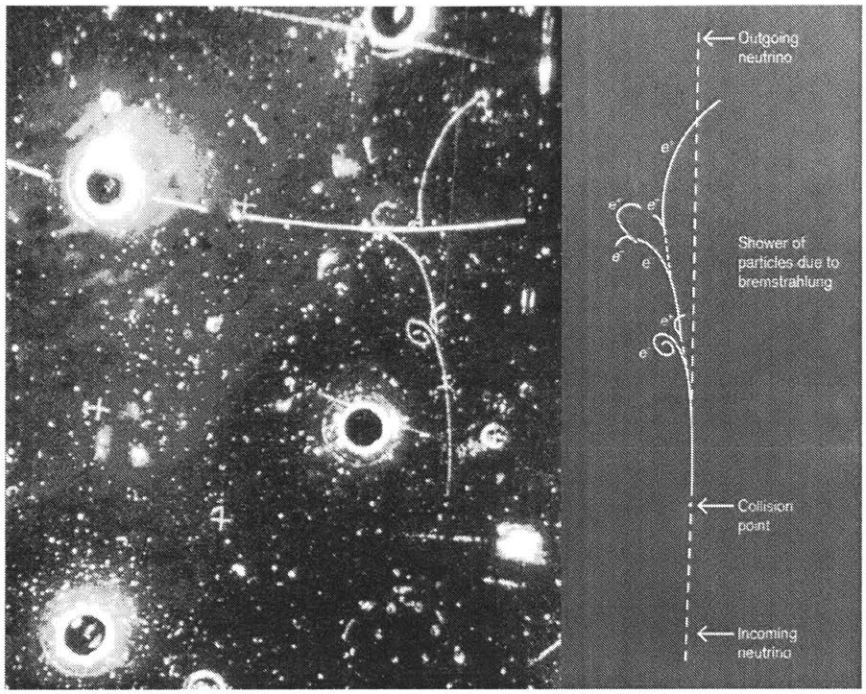

Figure 1-1: Raw image together from the Gargemelle experiment with a fitted tracks pertaining to a neutrino interaction. The original incoming neutrino remained unobserved, but its induced shower can be clear seen, amidst the background of other spurious background events seen crossing horizontally across the neutrino event. These events provided the first evidence for neutral current interactions, an important milestone in neutrino physics. From [1]

Once you understand the processes at play inside your detector you can begin to optimize your detector running to match the needs of the experiment. There is no such thing as the perfect experiment with a perfect detector that can perform all possible searches at once, compromises must be struck. Certain experiments emphasize a faster readout to ensure that they catch every possible event, while others may opt for smaller slower "nets", which take longer to readout, but give you a clearer idea of what happened at that given time. Rare-event searches, as their name implies, focus on phenomena that occur on timescales ranging from a few times a day all the way up to the age of the universe and beyond. Most of our everyday experiences occur at faster timescales, reflecting the fact that there are far more physics background processes that can occur at higher event rates. This is the predominant challenge that faces every rare-event search. Therefore, when we capture a particle in our "nets"

we must be absolutely sure that it is a signal, as the next signal event might take a long time or could get confused with a background event. At the same time, these rare-event searches often present challenges in scale since the bigger they are the more "die rolls"/chances you get to see your signal. At the same time, as experiments grow in scale their sensitivity to all background processes grows as well (sometimes faster than the signal sensitivity). This prompts other experiments to focus on building build smaller more specialized detectors that have a heightened sensitivity to signal events. What is the advantage of waiting so long for such a rare event? Rare-event searches can probe new processes that govern physics at the highest energies and densities mimicking the conditions found in the early universe.

In this thesis, we will examine the three experiments that I have worked on over my graduate career: dark matter searches with CDMS/CDMSlite, neutrino scattering with Ricochet and nuclear physics modeling with CUPID-LIS. All these experiments are linked together by their detector technologies, cryogenic bolometers, which they all employ in order to achieve low threshold high resolution spectra of their respective signal processes. The diversity of their physics goals also showcases the utility of using cryogenic bolometers in rare-event searches. Regardless of the physics goal, there were three questions at the center of all our discussions (especially during our long "French-Style" lunch breaks): "How can we maximize the probability of seeing our rare signal event?", "What are the backgrounds that can mask our signal?" and "How can our detector distort our signal event?" Luckily for us, we had some really good nets...

Chapter 2

Introduction to Bolometers

"Measure what can be measured, and make measureable what cannot be measured."

— Galileo Galilei (1564 - 1642)

I have worked on three different experiments (CDMS/CDMSlite, Ricochet and CUORE-LIS) and I have had the opportunity to learn the techniques and thought processes that have gone into extracting the physics results from each of these experiment. Each of these experiments seeks to answer very different physics questions and therefore undergoes a different set of optimizations in order to maximize the signal readout probability, while also minimizing the impact of all possible backgrounds in the signal region of interest. The item that ties all these experiments together comes in the form of their detector hardware. All these experiments utilize cryogenic bolometers that convert a particle interaction inside the detector volume into a usable heat signal that can then be read out by your readout electronics.

In recent years, there has been amazing progress in the fields of detector construction, cryogenic infrastructure and readout which have opened the door for experiments to probe ever deeper into new parameter space[1]. There are many different particle properties that one can measure depending on what physics you want to extract out

[1]One important piece of terminology that I will attempt to keep straight throughout this thesis is the difference between *parameter* and *phase* space. Parameter space encompasses different theoretical models that predict different particle properties than can be tested by experiment. Phase space deals with the various intermediate states of a physical system, this is usually integrated over within a particle physics theory to generate the parameter space of said theory

of your experiment. In particular particle identification, energy, event position and direction are among the most important quantities that one attempts to extract, each of which play a different role depending on what you are trying to measure. A lot of work goes into optimizing each of these components to allow for maximizing the experiment's sensitivity to the particular physics phenomena that you are attempting to measure. For example, in CUORE, the main goal of the experiment is to measure the the $0\nu\beta\beta$ decay of Tellurium-130, with a Q-value of 2.5 MeV which means that low energy background (keV level) processes are not factored in the overall design of the experiment. It is the energy resolution at 2.5 MeV that is critical for determining the sensitivity reach of CUORE. On the other hand, the sensitivity reach of CDMS is driven by the $\approx$ keV threshold of the experiment, setting it as low as possible while rejecting as much background through multi-channel readout. Often optimizing a rare-event detector/experiment for one specific phenomena, means compromises have to be made that make it unsuitable other rare event searches. This is why the physics community has not just constructed one single massive rare-event detector that performs all possible searches simultaneously. In the following chapter, I will discuss some of the considerations that go into designing low-background rare event searches in terms of the hardware that makes these experiments possible and the backgrounds that must be taken into account.

2.1 Detector Readout Basics

At the most basic level all cryogenic bolometer-style detectors operate on the same principal. First, either a particle or some type of radiation interacts with your detector crystal depositing at most all its energy (E_{dep}) into the crystal volume. The detector will then convert this initial E_{dep} into one of three channels heat, charge or light. The exact physics of how this conversion occurs depends greatly on the individual setup as well as environmental factors such as the operating temperature or crystal impurities, but also on the exact energy/topology of the initial interaction. All experiments fall somewhere on the "readout triangle" shown in Fig. 2-1. An ideal experiment

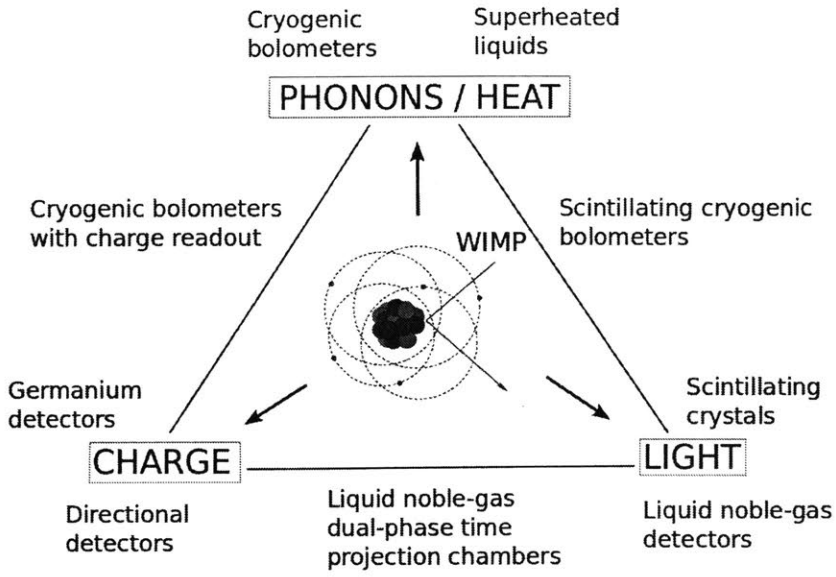

Figure 2-1: All experiments operate somewhere on this readout triangle and/or take advantage of position reconstruction that can be performed using any one of the readout channels. CDMS operates using dual ionization/phonon readout, while CUORE and Ricochet operate using a single readout channel (phonon/heat), but seek to take advantage of better position reconstruction in order to discriminate between background and signal events. Taken from [2]

would read out phonons, light and charge simultaneously with perfect energy and location accuracy in order to reconstruct the complete event that occurred within your detector. In practice, however; compromises must be made between various detector technologies and their limitations and this is where your physics goals must be taken into account. An important 4th side to the triangle, not shown in Fig. 2-1, comes in the form of event position reconstruction, a technique that can be applied regardless of the readout technology employed.

As a general rule being able to use two or more sides of this "hypertriangle", known in some circles as a tetrahedron, allows one to more effectively discriminate between signal and background events. This is especially true as you lower the threshold of your detector and it becomes more difficult to tell the difference between noise, background and signal events. This is because different physics event topologies will generate either different ratios of the energy quantities outlined in Figure **??** or have a

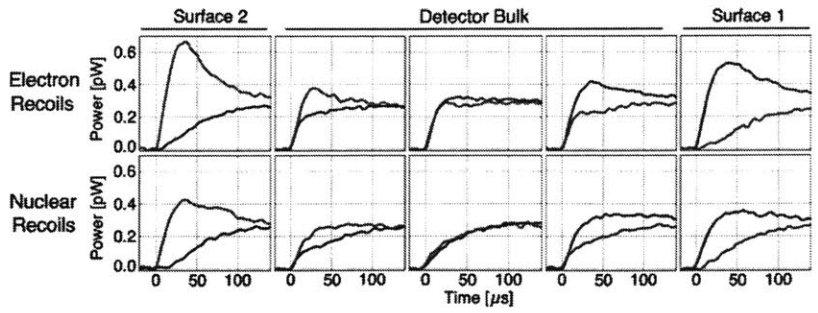

Figure 2-2: Example CDMS pulses to highlight the power of position reconstruction with pulse shape discrimination. The blue and red lines represent the summed amplitude of all the phonon readout channels on the top and bottom of the CDMS detectors. All events here show approximately 50 keV E_{dep} events. Taken from [3]

unique spatial distribution throughout your detector. To highlight the power of using two channels to discriminate between various event topologies, consider a high energy γ that deposits energy inside a CDMS-style bolometer. This event will generate more charge due to the strong coupling between the γ and the charge carriers and the relative inefficiency of converting that energy into phonons/heat. Therefore if you see a small signal on the phonon channel and no signal in the charge channel, then it must be a nuclear recoil induced by a DM particle or a neutron. If the reverse is true, and you see a large spike in the ionization detector, then you would deduce that the origin of this signal had a strong EM component and could not be dark matter.

Now consider an α particle that interacts within your detector volume after being generated somewhere in the surrounding volume, basic physics tells us that this α will only travel a short distance into your detector before getting stopped and depositing all its energy into the detector. This means that if you can reconstruct the position of every event inside your detector with perfect accuracy you should see an increase in the number of events that occurs near the surfaces of your detectors [2]. If you then go and define a skin thickness to your detectors, where if an event occurs within this skin you disregard it as background and only look at events that occur inside the bulk of your detector, this process is known as "fidualization". One way to determine

[2]It is this fact that results in the old adage that within the rare-event community, "Sensitivity increases with volume, while problems increase with surface area"

where inside your detector an event occurred is to look at the timing information provided by your readout. The closer to your readouts your event occurs the faster the signal pulse will rise since your energy carriers have a shorter distance to travel - see Figure 2-2. This figure also highlights the ability of pulse shape discrimination to perform as an extra handle on determining the yield of a specific event, you can see by eye the slight difference in pulse shape between the electron and nuclear recoils. On the other hand, your signal events (in the above case WIMP induced nuclear recoils), have a uniform probability of occurring anywhere within the detector volume.

It should also be noted that within the literature there is a lot of experiment/detector specific parlance which can make direct comparison between experiments difficult. For example, "ballistic phonons" can be defined by the fact that these are phonons that come directly from the interaction site and have not scattered off of a surface or interacted with other phonons. It can also refer to a specific range of phonon energies regardless of their production mechanism. I will try to steer clear of as much experiment specific parlance as possible, but this is something important to bear in mind. Also a lot of the physics that I will be describing here has an explicit temperature/material dependence so the exact proportion/magnitude of each of these processes will vary from experiment to experiment and from setup to setup. That all being said, I will attempt to describe in general terms some of the basic processes that allow for the detectors that I have worked with to turn an event interaction into a usable signal.

With all the warnings out of the way, we can now discuss the process of converting the initial E_{dep} into either phonons, charge carriers, scintillation or even quasiparticles in superconductors. We will briefly summarize the main four ways that the initial E_{dep} gets converted into energy carriers.

- Phonons (heat carriers) are the collective excitation/vibration of a crystal lattice, they do not constitute a particle per-say, but are often treated as such. These carriers mostly carry off the heat energy generated by an event, the exact physics of the transport and excitation of these phonons is still an active area of research and beyond the scope of this thesis. For a broad overview of

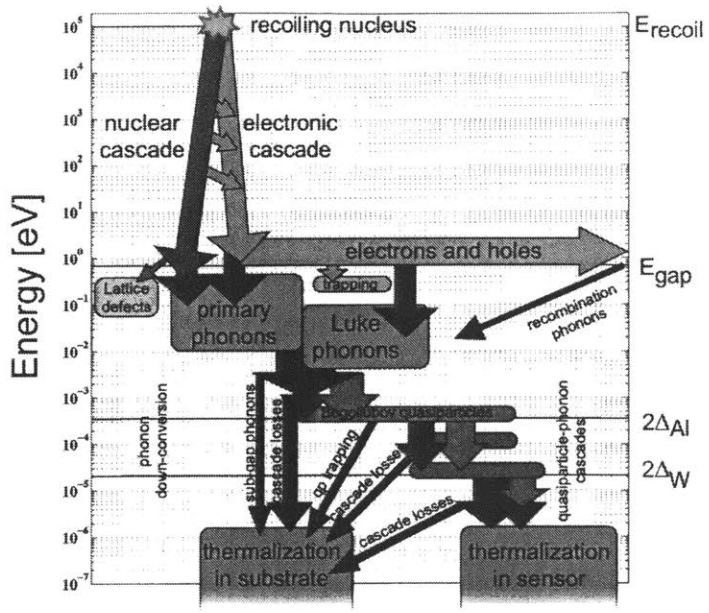

Figure 2-3: A figure detailing all phonon processes that occur within a CDMS detector starting from the initial recoil down to the final thermalization in the substract/sensor. Note that the processes that occur above $\approx$ 1 meV are crystal/material dependent and can be applied to phonon processes in most bolometers. All the processes that occur below this threshold are CDMS specific and pertain to the exact physics used to convert the phonon signal into a usable electronic signal via Transisition Edge Sensors (TES) - the exact physics of which are discussed in Section 2.4.1. Taken from [3]

all the processes involved in phonon transport in CDMS I direct you to [3].

1. Primary Recoil Phonons: Once the event energy is converted into heat, or more exactly lattice vibrations, this sets off the initial primary recoil phonons. For nuclear recoils the phonons are created by the physical movement of the nucleus within the crystal lattice. In the case where the E_{dep} is deposited more on the electrons surrounding the nucleus, these primary phonons are generated by the excitation of these electrons to higher energy states.

2. Luke-Naganov Phonons: Some fraction of the initial E_{dep} will be deposited onto the electrons surrounding the nucleus and some electrons will be freed (or ionized) and begin to drift through the crystal. The exact proportion

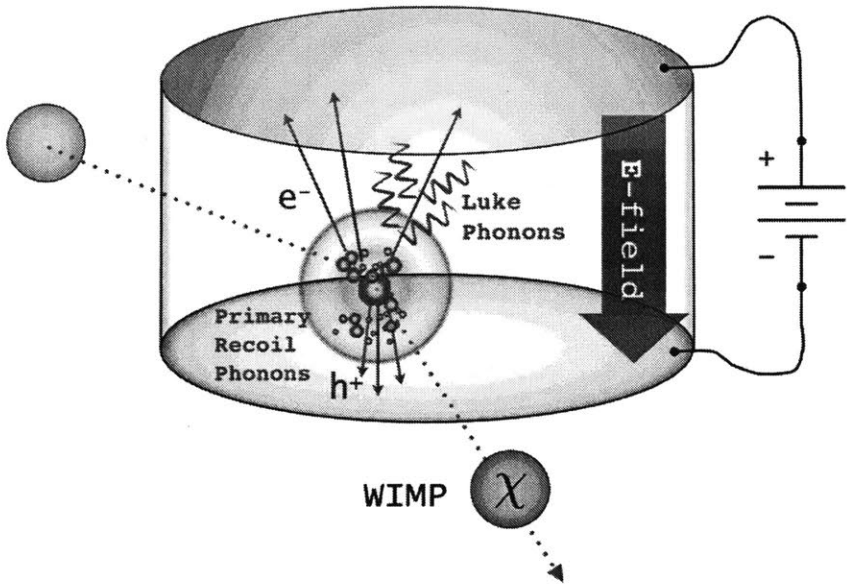

Figure 2-4: Schematic of the basic operation of CDMSlite taken from [5]

of energy deposited into the electrons verses the primary phonons is summarized in the event yield which we will discuss more in detail later. For now though, the electrons that are freed this way now can drift through the crystal pulled, by the weak potential[3] biased across the detector. Afterwards these electrons can be picked up by the ionization readout. However; if one increases this potential across the detector, as was done on CDMSlite up to 69 Volts, one can drag these electrons through the crystal where they rapidly approach their terminal velocities. This velocity is determined by the phonons scattering off the crystal lattice and it does not account for the full energy of these electrons. The extra energy imparted onto the electrons is then radiated off as additional Luke-Neganov phonons [4].

3. Other processes can also contribute to the total phonon signal observed in a detector. We will not go into too much detail here, but they should be mentioned. Specifically on CDMS, the main two that are discussed

[3]In the normal running mode of CDMS the detectors were biased with $\pm$ 2 on each side for a total potential difference of 4 volts across the whole detector

are relaxation phonons and recombination phonons. Relaxation phonons are produced when an electron is imparted with enough energy to reach an excited state, but not quite enough to completely ionize and travel freely towards the ionization collectors. These electrons then relax down to the Fermi-sea level and generate additional phonons, the particulars of which are discussed in much more detail in [6]. In addition, there are recombination phonons. These occur when charge carriers (electrons or holes) arrive at the surfaces of your detector and then recombine with their opposite number releasing their potential energy into phonons. The effect of these phonons is small compared to the Luke-Naganov and Primary Recoil Phonons.

4. Thermal Phonons: The process/propagation times for all the other phonon process described so far are in the μs range or even faster. These phonons can often be of very high energy as they travel through the detector and travel close to the speed of sound inside the detector crystal. Once the initial interaction occurs inside the detector additional processes, such as aharmonic decays [7], can take these initial high speed phonons and convert them down to lower energy thermal phonons - see also [8]. These thermal phonons can fill the entire volume of your crystal, warming the entire detector, which makes it easy to readout at the cost of slower dynamics that result in longer readout times. These are phonons that the CUORE experiment collects using their NTD-based senors described later.

- Electron/Hole pairs (charge carriers) Of all the experiments discussed in this thesis, only CDMS utilizes this readout channel. Germanium and Silicon are both semiconductor materials which means that the spacing between the valance and conduction bands can be quite small, at 50 mK the band-gap ends up being around 0.74 eV (E_g). The total energy needed to generate an electron-hole pair in Germanium ends up being parameterized as:

$$\epsilon_\gamma = E_g + < E_k >_{e/h} + r\hbar\omega_R \tag{2.1}$$

The second and third terms are the average kinetic energy of the electron/hole pairs in the crystal lattice and the contribution of Raman phonons following the parameterization in [9]. Raman phonons are generated in order to radiate off the excess energy needed to break the bond between the lattice and the newly created electron-hole pair. In particular, r is the number of optical[4] phonon scatters per ionizing event, and ω_R is the Raman phonon frequency. The resulting energy needed to create an electron-hole pair in Germanium ends up being around 3 eV total [11]. Another important aspect to remember is the idea of the "event yield", which again changes definition from experiment to experiment, but in CDMS represents a ratio of energy available to generate charge carriers to the total energy desposited in the event - see next section and in particular Fig. 2-5

- Scintillation photons (light): If you happen to have a scintillating bolometer, one other avenue that the initial E_{dep} splits off into is light. Scintillation light has the advantage of being easy to detect, often with a well known wavelength (usually in the visible or near-visable range), without the need to attach additional sensors to your crystal. [12]

2.1.1 Yield Considerations

For each experiment that measures two different readout channels simultaneously, one often defines an additional event quantity known as the yield, Y. This represents the ratio between how the initial event energy, E_{dep}, is then divided up between the two readout channels. As with all the above sections, the exact definition varies from experiment to experiment, but we will take CDMS as a case study. CDMS defines their yield (Y) as the ratio between the energy deposited in the ionization channel and total energy of the nuclear recoil recorded in the event. If you plot this yield as a function of recoil energy as shown in Figure 2-5, one can quickly note that the

[4]Again terminology can get confusing here, but for our purposes optical phonons are phonons whose dispersion relation follows $\omega_+ = \sqrt{\frac{2(\kappa_1+\kappa_2)}{m}}$ at $k = 0$ see Figure 10.6 in [10]

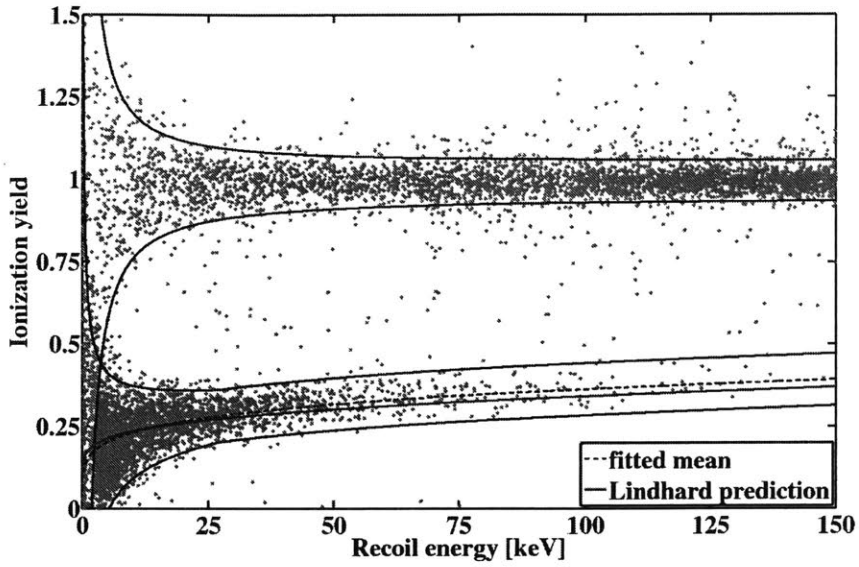

Figure 2-5: Typical CDMS yeild plot, showing the double band structure that provided the powerful background rejection capabilities of CDMS. Taken from [13]

yield produces two clear event bands centered around 1. In CDMS, the event energy is often normalized with respect to the ionization channel thus resulting in an event yield centered around 1 and ≈ 0.25, with the upper band representing events dominated by electron recoils (more ionization energy) and a lower band representing nuclear recoils (more energy in the phonon sector). Above 25 keV, there is clear separation between the two yield bands, but at the very lowest energies this separation becomes less and less effective as an event discriminator. This is due to the increasing uncertainty in the event energy reconstruction.

At higher energies it is possible to fit a 3 σ nuclear and electron recoil band thanks to the clear separation between the bands and the high event statistics available in these regions. At these very low energies it often becomes useful to instead define a parameterized model for the yield which can be extrapolated down from the fitted bands calculated at higher energies. The most common method for doing this comes in the form of the Lindhard parameterization [14][15] given by the following four equations:

$$Y(E_{recoil}) = \frac{kg(\epsilon, E_R)}{1 + kg(\epsilon, E_R)} \tag{2.2}$$

$$\epsilon = 11.5\, E_R Z^{-7/3} \tag{2.3}$$

$$k = 0.133\, Z^{2/3}\, A^{-1/2} \tag{2.4}$$

$$g(\epsilon) = 3\epsilon^{0.15} + 0.7\epsilon^{0.6} + \epsilon \tag{2.5}$$

$$k_{\mathrm{Ge}} = 0.157 \tag{2.6}$$

In above equations, Y is the yield and the recoil energy E_R has units of keV, all the other values are driven by experimentally determined values. In particular, these experimentally determined values provide some of the largest points of contention in any dark matter search result. Even small changes to any one of these parameters affects the energy spectrum of your recoil events, which changes the effective threshold value in your DM search. This in turn can have a huge impact on your final sensitivity reach. For a more detailed discussion of the derivation of these parameters, I point you to [3], specifically Chapter 3.

2.2 Dilution Refrigerators

In recent years there has been amazing progress in the field of cryogenic technologies and infrastructure. One example is the CUORE cryostat (for a full technical report on the inner workings of the cyrostat see [16]), which which in 2017 gained fame for cooling the coldest cubic meter in the known universe [17]. In particular, rare-event searches have benefited from cryogenic advances, since their sensitivity is directly correlated with the overall size and run time of their experiments. At the same time, it is vital for these cryogenic experiments to operate as close to absolute zero as possible in order maximize the relative signal to noise ratio of the incoming signal. To illustrate this, we will take a 1 MeV signal event, which is a typical E_{dep} encountered in the CUORE experiment. Using the measured value of the specific heat of TeO_2 [18], one can calculate that the overall induced temperature change of the crystal would be on the order of 100 μK, well below the standard operating temperature of 10 mK highlighting the relative scales of these events.

Material	Temperature (K)	Notes
Ice	273	Most common source of clogs and headaches for experiments
Oxygen	90	
Nitrogen	77	Commonly used to 'pre-cool' cryogenic systems due to its availability
Helium-4	4.2	Pure He-4
Helium-3	3.2	Pure He-3
Helium-4 (pulling vacuum)	1.1	This temperature can only be achieved if you pump on a bath of Helium

Table 2.1: A collection of some of the common temperature encountered in cryogenics values taken from [19]

The current world record for coldest measured temperature lies at around 100 picoKelvin. In order to cool down large bulk volumes of material down to cryogenic temperatures the leading technology is a dilution refrigerator.

The CDMS, CUORE and Ricochet experiments take advantage of "dry" dilution[5] refrigerators, so called as to not require backfilling of liquid nitrogen/helium to pre-cool the cyrogenic load, drastically reducing their operating costs. An additional advantage of no longer having to perform backfills allows for the refrigerator to run with a fair amount of automation as seen on the Oxford Triton and Cyroconcepts UQT fridge models.

The basic physical principals that allow dilution refrigerators to work are summarized in Figure 2-6, in particular we will focus on the region labeled "Superfluid He-3/4". Once you cool Helium below $\approx$ 2 K one enters a the strange world of condensed matter physics and He phases. This initial temperature of 2 K is reached in one of two ways. In "wet" fridges you thermally connect your experiment to a bath of liquid helium, which you then pump on, usually with a roughing pump, dropping the temperature from 4.2 K down to 1.2 K via evaporative cooling. In "dry" fridges, you forgo this liquid helium bath in favor of pulse tubes (for the original paper on their invention see [20]), which use pressure waves induced on your working gas (in

[5]Please do not commit the same mistake I did in my first year and refer to these refrigerators as "delusion" refrigerators

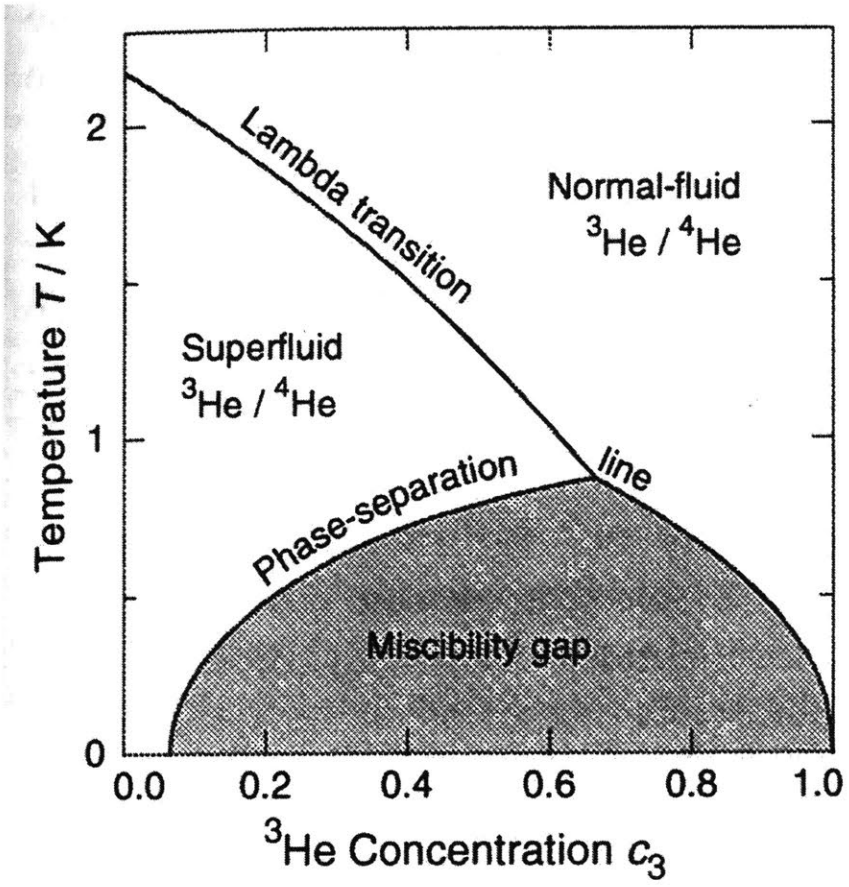

Figure 2-6: The helium phase diagram. Here the miscibility gap represents an area of phase space where that particular combination of temperature and He-3 concentration can not occur. Taken from [19]

our case Helium) together with a compression piston to cool the working gas. There have been many advances in the design and operation of these pulse tubes over the course of latter half of the 20th century [21]. It was not until the first pulse tubes that could get below the boiling point of nitrogen [22] arrived on the market that they were seriously considered for use in large scale Cyrogenic systems such as dilution refrigerators. These systems continue to be improved. The massive CUORE cyrostat [16] uses 5 pulse tubes and has been able to achieve the unheard cooling power of 600 Watts at 77 K, allowing them to cool down nearly a metric tonne of material down to the target temperature of 10 mK. The exact techniques that modern pulse tubes implement in order to achieve these cooling powers are closely guarded secrets of the pulse tube manufacturers, such as Cyromech. These pulse tubes though do have one major disadvantage. The piston action can act like there is a hammer constantly hitting your cryostat. This could then induce unwanted noise/energy into your readout/crystal.

The next discussion assumes that you have reached the liquefaction temperature of your mixture either through pulse tubes or via pumping on a pool of liquid Helium cooling via evaporation. The main mechanism by which the dilution refrigerator works to get below 1 K is by taking advantage of differences between the physical properties of He-3 (a Fermionic material) and He-4 (a bosonic material). As Helium-3 obeys Fermi Statistics. This means you can write down the effective Fermi Temperature, which by extension is a measure of the average kinetic energy of your He-3 atoms have, as:

$$T_{Fermi} = \frac{\hbar^2(3\pi^2)^{\frac{2}{3}}}{2m_{eff}k_b}(n_{He-3}^{\frac{2}{3}}) \tag{2.7}$$

where $(n_{He-3}^{\frac{2}{3}})$ is the number density of He-3 in your system. It is important to note that the temperature (and therefore the average kinetic energy) of the He-3 atoms increases with number density. Nature tends for systems to enter into their lowest energy state and two Fermions can not occupy the exact same quantum state. This leads Fermionic systems to "stack" and reach ever higher energy levels as you increase the number of particles in your system. Multiple bosons, such as He-4, can occupy

the same quantum state, which means that they can fill out lower energy states and spread "horizontally", without having to occupy the higher energy states. This means that one way to ensure that the overall system finds the lowest possible energy is to weakly bind the He-3 and He-4 atoms together. However; this can only be done up until a point, due to the fact that as you increase the number density of He-3 you also increase the average kinetic energy of the He-3 in the system, eventually breaking the weak bonds formed between He-3 and He-4. The maximum number density (measured as the concentration of He-3) that can be achieved in this supermixture of He-3/4 ends up being around 6.5 %[6]. The remaining He-3 therefore forms a separate phase. This phase is nearly pure He-3 and called the rich/concentrated phase. This rich phase distinct from this superfluid mixture of He-3/4 and floats on top of the 6.5 % dilute phase. This all occurs within the so-called mixing chamber of your dilution refrigerator. If you pump on this system and pump out only the dilute phase, the He-3 of the concentrated phase will seek to replace the He-3 lost in the dilute phase in order to maintain this 6.5 % concentration. This leads to heat being pulled out of the anything connected to the mixing chambersee Figure 2-8

As shown in Figure 2-7, once you have pumped on the dilute phase, the mixture enters the still where the same phase separation process takes over and results in almost pure He-3 exiting the Still and entering your circulation system. After the He-3 has circulated through the system it reenters the still, which operates at 700 mK and then reenters the mixing chamber as close to the base temperature as possible to minimize any heat re-introduction into the mixing chamber. One of the main advantages of this process is that there are no moving parts below the still, all the movement and heat exchanges are performed passively using vacuum that is created using just the circulation pumps. The main challenge in running a dilution refrigerator comes in the form of the engineering and precise tuning of each of the stages to ensure the best possible performance of the refrigerator.

When you take a closer look at the individual (shown in Figure 2-8) stages on our dilution refrigerator, which we named Olaf after the snowman in Frozen, one can

[6]The exact number does depend on the temperature, but here we will take the limit as T $\rightarrow$ 0

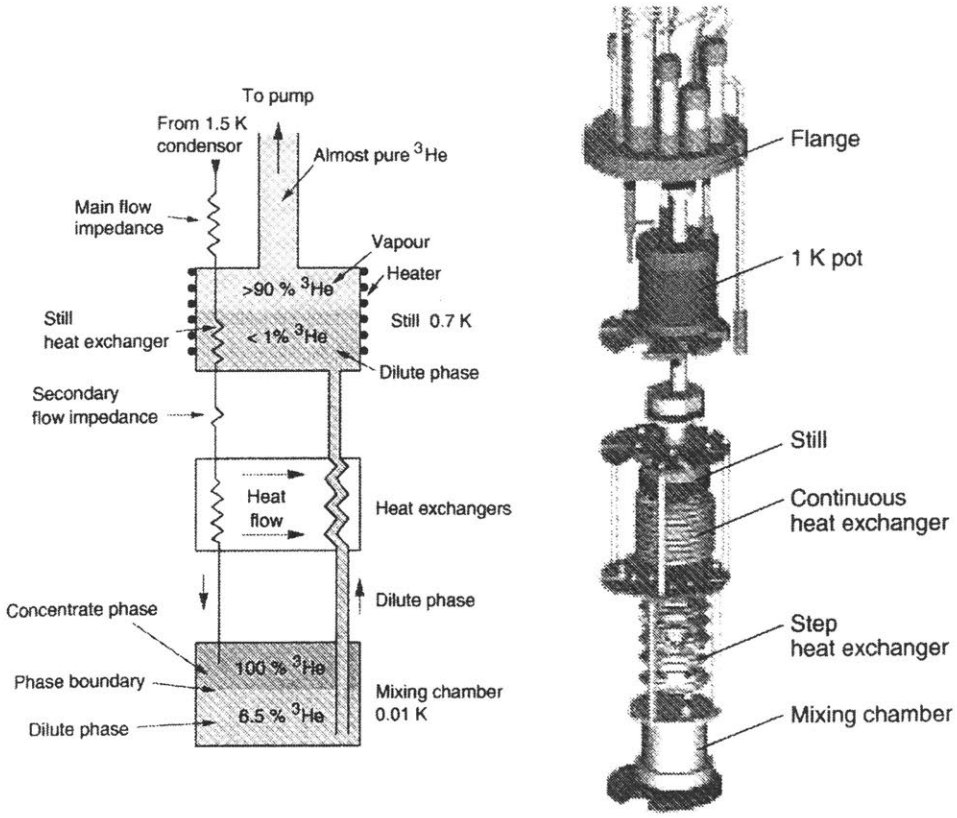

Figure 2-7: The basic operating principle behind a standard Helium 3/4 dilution refrigerator. Taken from [19]

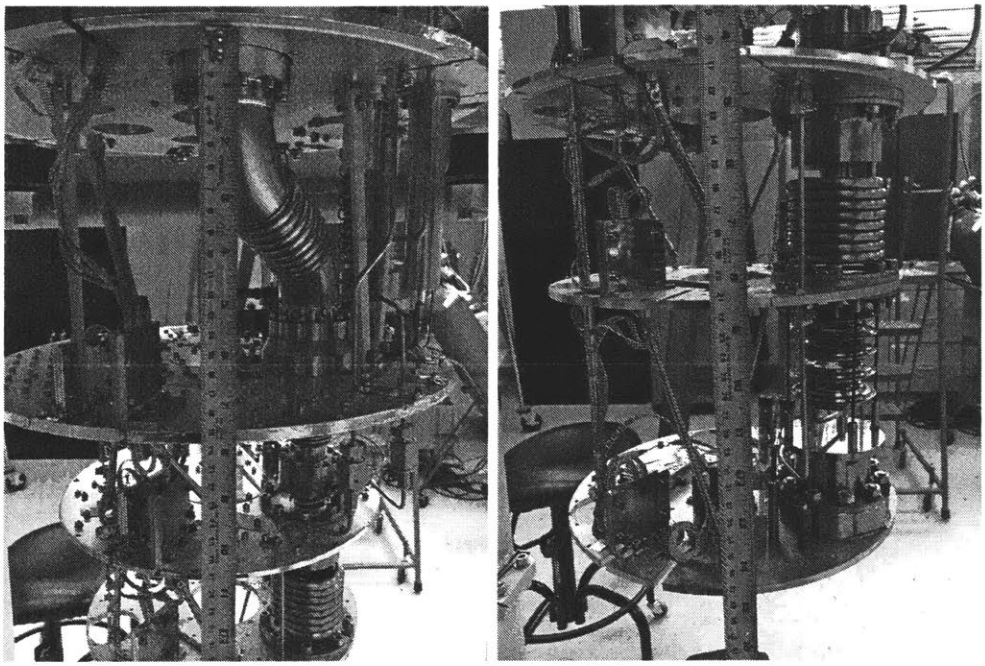

(a) 70 K, 1 K and still Plates (viewed from top to bottom) installed on Olaf

(b) Still, Cold and Mixing Chamber Plates installed on Olaf

Figure 2-8: All the stages of the dilution refrigerator, named Olaf, installed in MIT room 24-036. The individual stages are named after the temperatures that during baseline operation they are designed to reach.

identify some of the engineering that goes into the design of these fridges. For full details on all the engineering, from the heat exchangers to exact workings of the pulse tubes, that goes into the design of these refrigerators I strongly refer the reader to chapter 11 in [19].

2.3 Vibration Measurements on Dry Dilution Refrigerators

One particular item that I want to focus on comes in the form of vibrations induced by pulse tube cooling. The pulse tubes as described earlier are what allow us to reach the initial temperature of 4 K, which is when the mixture in the system liquefies allowing the the dilution process to take over. One of the primary components of the pulse tube system comes in the form of a piston that oscillates at $\approx$ 1 Hz to drive the gas oscillations that are the driving force behind the cooling power. These oscillations, which act as though you were hitting the fridge frame with a heavy hammer every second, can induce vibrations that can then travel throughout the rest of your fridge setup [23] [24]. These induced vibrations can then inject extra power into whatever load you have running in your fridge, for example electron microscopes [25] or crystal bolometers. This decreases the sensitivity levels by decreasing the energy resolution by increasing the noise in the signal to noise ratio.

This is a problem that wet fridges do not encounter as they achieve the initial cooling through the passive cooling via liquid Helium. Therefore the goal of Cyrostat R&D with current dry, pulse tube-based, dilution refrigerators is to reach the same baseline vibration level achieved with wet dilution refrigerators. To this end we undertook a series of measurements with low-noise accelerometers with the goal of characterizing this pulse-tube induced vibration level on various dilution fridge models each of which uses different vibration mitigation technologies (see Figure 2-9) with the goal of reducing the effect of the pulse tubes.

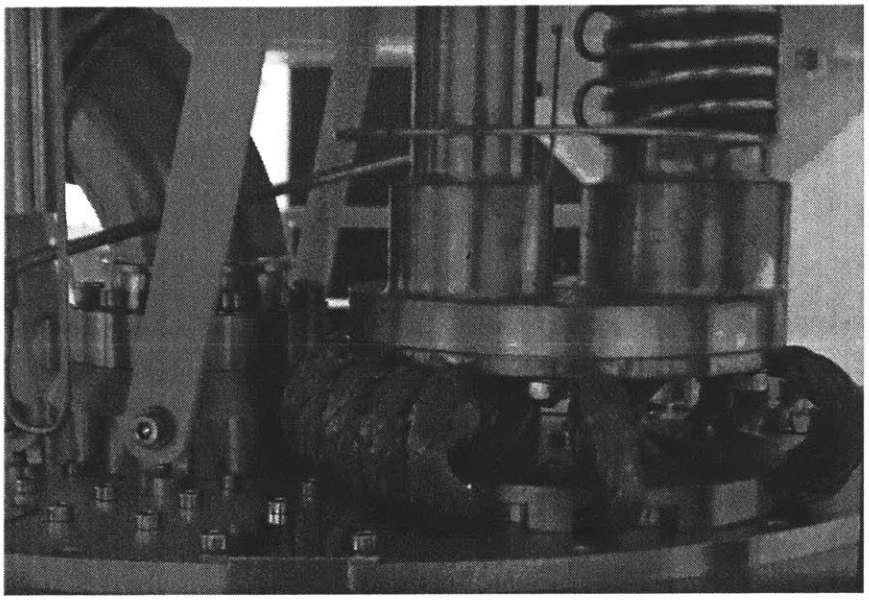

Figure 2-9: The pulse tube head on Olaf's 4 K plate along with the vibration isolating copper braiding designed to mitigate the propagation of vibrations down to the lower stages of the fridge. One of the main challenges faced when attempting to isolate vibrations is that you still need to provide effective thermalization via physical contact, but somehow not transmit vibrations through that same connection. The thick copper braid seen here is designed to act like a high-frequency bandpass filter

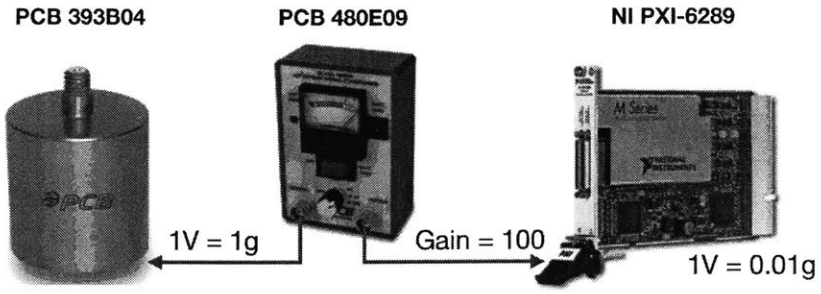

Figure 2-10: Measurement Setup for measuring the vibrations induced on the Olaf Fridge

Experimental Setup

To measure the vibrations on the Mixing Chamber (10 mK cold plate) of the Olaf refrigerator, we set up the following readout chain composed of a high sensitivity PCB-393B04 seismic accelerometer[7], a PCB-480E09 signal conditioner and a 16-bit National Instrument DAQ readout create PXI-6218 as shown in Figure 2-10. These particular modules were chosen due to their low-noise performance in the frequency range of interest for us. In addition, we ran these modules at room temperature[8] and under soft vacuum ($\approx$ 1 mbar) to reduce acoustic pick up that could interfere with our readout measurement.

On Olaf, only measurements were undertaken with the accelerometer placed in the z direction, while on the other cryostats measurements were undertaken in both the z and r directions.

Results

Using the experimental setup described in the previous section we could then collect data with the pulse tubes on and off. The first step in our analysis was to perform a Fast Fourier Transformation (FFT) on the 5 second data windows that we collected on our accelerometers to then calculate the Power Spectral Density (PSD) (data for the Pulse Tubes ON on Olaf shown in Green in 2-13) for frequencies between 1 and

[7]PCB Piezo-electronics, typical sensitivity of 1 V/g in the 1âĂŞ750 Hz frequency region

[8]Running these modules at cryogenic temperatures was not an option as all the accelerometers we looked at that would work at cryogenic temperatures did not have the noise performance we needed

Figure 2-11: Mounting setup of the accelerometer as mounted on the Mixing Chamber plate on Olaf. One of the main concerns when running the blue readout cable came in the form of peizo-capasitances created when the readout cables are mechanically stressed. These capacitances could induce additional noise in our readout signal, which is why you see zipties and fishing lines (not pictured) to tie down these cables to the various support beams

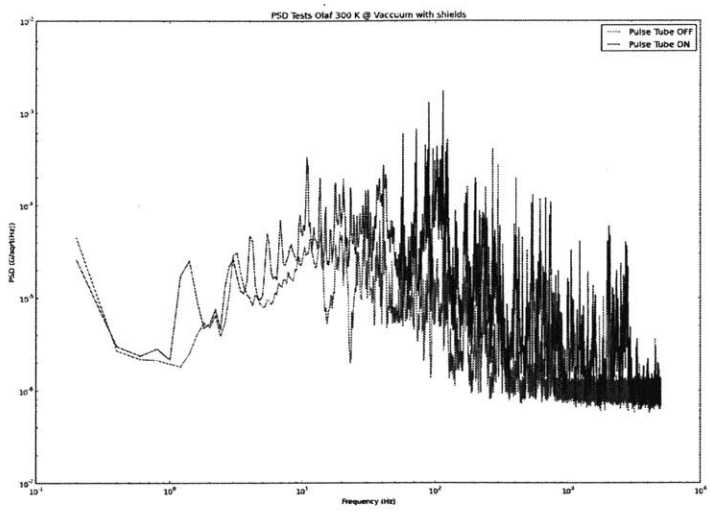

Figure 2-12: Olaf PSD in units of g/$\sqrt{(Hz)}$ with the pulse tubes both on and off. One can clearly see the peak associated with the $\approx$ 1 Hz oscillation frequency of the pulse tubes

1000 Hz. In following section, we divide the frequency domain at 1-40 Hz, which is the region that most affects slower readout technologies, such as NTDs and into 40-1000 Hz, which affects faster TES-sytle readouts. Both these detector technologies will be discussed more in the following sections. By looking at the raw PSD we are better able to deduce the source of any spurious vibrations as seen in Figure 2-12

One way to better gauge the effect that these vibrations have on the overall setup is to convert the PSD into units of displacement instead of acceleration as this gives us a better handle on the total amplitude of the oscillations being injected into the system in both frequency ranges of interest. This is achieved by first integrating twice in Fourier space via the following relation:

$$PSD_{displacement}(f_i)[\text{m/sqrt(Hz)}] = (\frac{9.81\frac{m}{s^2}}{2\pi f_i})^2 PSD_{acceleration}(f_i)[\text{ g/sqrt(Hz)}] \quad (2.8)$$

We then used Parseval's theorem as discussed in [27],to determine the RMS displacement across the specific frequency regions using:

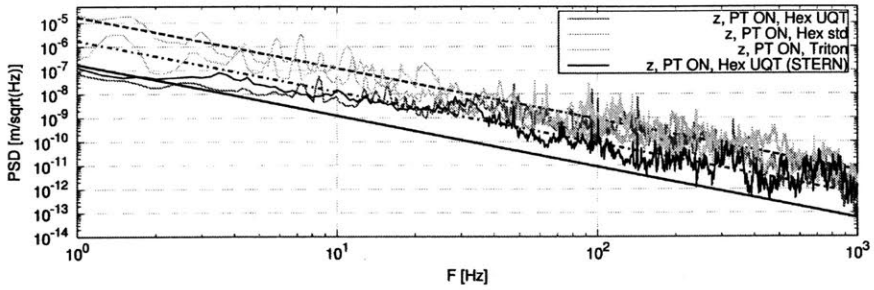

Figure 2-13: Displacement of fridge vibrations compared to other fridge units. Olaf results labeled under "Triton". Taken from [26]

Cyrostat and Orientation	Displacement Reg I [μm] (OFF)	Displacement Reg II [nm] (OFF)
Triton 400 (z direction)	2.4 (0.3)	56 (19)
HexDry UQT (z direction)	0.071 (0.066)	25 (22)
HexDry UQT (r direction)	1.2 (.3)	116 (22)

Table 2.2: Summary of the displacement measurements undertaken on the Olaf and the HexDry UQT cyrostat systems, values taken from [26]

$$RMS_{total}|_{f_i}^{f_f} = \sqrt{\sum_{Region} (PSD_d(f_i))^2 \Delta f} \tag{2.9}$$

Where Δf is the inverse of the sample collection time, which for us ends up being 0.2 Hz. The results of our calculations are summaried in Table 2.2

As a point of comparison, I have included data collected on a HexDry UQT (Ultra Quiet Technology), which replaces the thick copper braids seen in Figure 2-9 with Helium exchange gas that flows between a series of radiator fins with one set connected to the pulse tube cold head and the second set connected to the 4 K plate. This has the advantage that you can still provide a thermal connection through the helium gas, but without physically connecting the pulse tube (and its induced vibrations) to the 4K plate. The results above clearly show that the UQT does effectively reduce the vibrations, particularly in Region I, where the pulse tube oscillations are most clearly felt (refer to Figure 2-12). Due to the long time scales associated with reading out Neutron Transmutation Doped (NTD - discussed more in the following section) readout, this means that NTD R&D efforts would benefit greatly from the inclusion of this UQT damping technology. As a case study our collaborators undertook a series

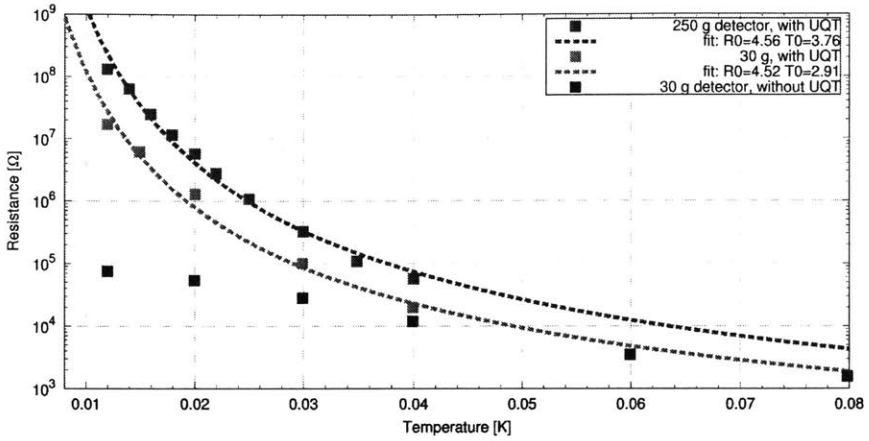

Figure 2-14: Effect of vibrations on NTD resistance measurements. 30 g detector measurement fitted to a Mott-Anderson Power curve. The black points in particular refer to the measurements taken with on fridge without vibration damping technology, as the temperature gets lower the overall effect of localized power injection on the NTD chip increases. Taken from [26]

of measurements using these NTD readouts with a 30 gram Germanium detector on a cryogenic system with (red points on Figure 2-14)and without (black points on Figure 2-14)the UQT damping system. As the operating temperature of the detectors was lowered below around 40 mK, one can clearly begin to see the divergence in the resistance readout from the NTD sensors. This reduced resistance indicates that while the overall 30 g Germanium detector is well thermalized to the operating temperature, the NTD sensors are experiencing a local injection of power through these mechanical vibrations. This local injection of power results in a higher effective temperature of the NTD readout compared to the crystal.

2.4 Detector Readout Technologies

No matter how pure or clean your detector crystal, it is only an inert chunk of material unless you have some way of converting a particle interaction into a readable electronic signal. The exact method of how this is achieved is highly dependent on the exact signal mechanics. In this section we will discuss the three different experiments that I have worked on to examine the ways that these different experiments have optimized

their detectors to search for the phenomena that they are most interested in. All the detectors we will discuss use sensors that are directly coupled to the crystal they are interested in, although there are proposals in the literature to remove this direct contact between the thermometer and crystal [28], those are beyond the scope of this thesis.

2.4.1 CDMS Detectors

As discussed earlier, when a particle interacts with your crystal detector, it can deposit some fraction (the Yield) of the total event energy to the phonon channel to produce the primary recoil phonons as seen in Figure 2-3. A quick order of magnitude calculation shows that the timescales for these initial phonon to travel through the detector once ends up being around 1 μs. After those initial recoil phonons are created, many different phonon processes take over and down-convert these initial phonons into lower energy phonons until the phonon "cloud" fills the entire detector volume isotropically, which corresponds to the thermalization of the cyrstal volume. However; if you wait until the phonons have thermalized[9] throughout the entire detector volume you lose a lot of the information associated with the event that created the initial burst of phonons. In particular you lose information associated with the exact timing, position of the initial event as well as losing the ability to discriminate between nuclear and electron recoils. For Dark Matter searches, such as CDMS, the loss of all this event-by-event information has an significant impact on the future sensitivity of any DM analysis. Therefore the main goal of designing the CDMS detectors was to design the detectors to read out as many of these initial phonons as possible and therefore glean as much event-by-event information from these phonons. This was achieved with the iZIP (interleaved Z-sensitive Ionization Phonon) detectors that used Transition Edge Sensor (TES) for the phonon channel readouts - shown in Figure 2-15, the operation of which I will attempt to summarize in a few lines. For the full details of how these detectors were designed I suggest the following sources sources [3] [5] [29]. CDMS detectors also have sensors designed to readout the charge

[9]The timescales for thermalizing the entire detector ends up being around 1 ms

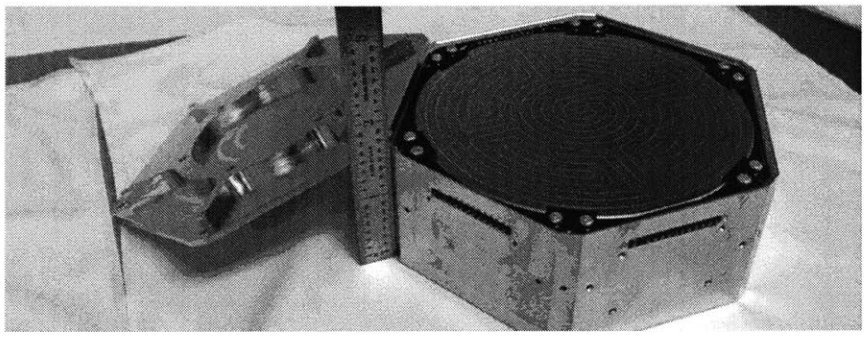

Figure 2-15: CDMS 600 gram iZIP detectors that will eventually be deployed at CDMS-SNOLAB, the structures you see on the surface correspond to the interleaved phonon and charge readouts. On these detectors there are 6 phonon readout (4 sectors plus the center region and an outer ring) and two charge readout channels.

produced in each event, but in this thesis section we will focus on the physics behind reading out the phonon signals as this will form the basis of the detectors developed as part of the Ricochet R&D program. TES phonon sensors operate on the simple premise that the transition between the superconducting and normal phase of a metal occurs at an extremely specific temperature (the critical temperature denoted T_C) with a narrow response domain - shown in Figure 2-16.

If you bias the sensor and balance the sensor temperature to sit exactly the T_C, using a precise mechanism called electrothermal feedback [30] [10], any slight change in the temperature of the sensor will result in a large change in the resistance of the sensor, which in turn read out as a change in voltage or current[11].

CDMS takes this concepts one step further by creating a phonon "band-pass" filter - shown in Figure 2-16. Tungsten has a very low T_C (between 50 and 150 mK), but this can be finely tuned during the manufacturing process via the manipulation of the two crystalline structures of Tungsten [31], while Aluminum has a much higher T_C (1.2 K). One of the main components of superconducting theory [32] is the idea of a Cooper pair, which is a pair of electrons tied together via a phonon exchange

[10]On CDMS a TES sensor coupled with this electrothermal feedback mechanism is called a quasiparticle-assisted electrothermal-feedback transition- edge sensors or QET and then if this was coupled with a SQUID array (which I will not discuss here) the whole thing turned into a SQUET, physicists do love their acronyms...

[11]If you keep the voltage constant and read out the change in current through your detector, you are running in *Voltage-biased* mode while if you keep the current constant and readout any changes in voltage you are running in *Current-biased* mode

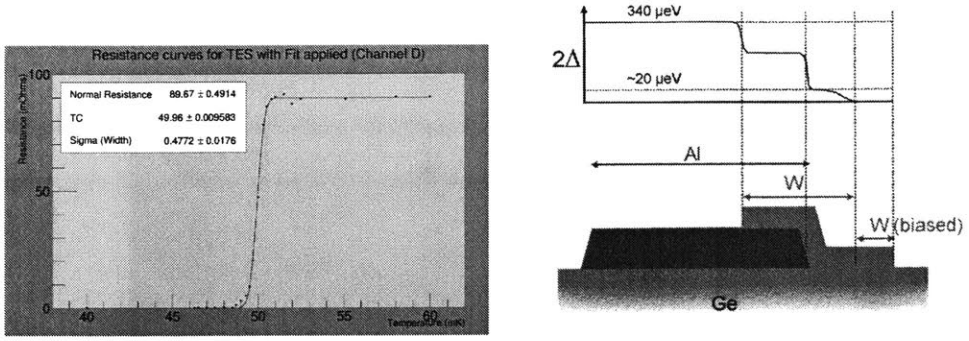

Figure 2-16: (a)TES resistance curved collected on a CDMS Tungsten TES using the MIT CDMS test cyrostat showing the basic operating principle behind a CDMS TES and (b) Cross section of the phonon readout scheme used in CDMS. In blue you see the Aluminum phonon absorption fins and in red the physical Tungsten TES readout. Taken from [3]

force. These Cooper pairs, which act a single bosonic particle in many instances, can only be created once your material has gone below its T_C and become the dominant energy carrier in a superconducting system, especially as you cool further and further below the T_C. It makes some sense then that the energy, which we will label as Δ, needed to create these bosonic particles depends on the T_C of the material they are in. [12]

If high energy phonons (read the initial recoil ballistic phonons) make it to the surface of the detector specifically the Aluminum fins, they will have enough energy to break the Cooper pairs inside the Aluminum fins and then via intermediate particles, called Bogoliubov quasiparticles [33], which then can diffuse into the Tungsten fins - see Figure 2-16, where they then relax into a lower energy state due to the lower Δ found in the Tungsten. During this relaxation these quasiparticles then release their stored energy in the form of phonon, which then heat up the TES sensor and provide a signal to the readout. The end result of all this nano-engineering is a TES sensor (see Figure 2-17)that is only sensitive to the initial burst of high energy phonons generated at the initial recoil site of the particle physics interaction at the μs timescale.

[12]Please note, I am skipping over ALOT of condensed matter physics in this discussion, but the main takeaway from this is that these particles have an energy of creation/annihilation that is proportional to the T_C of the materials they are in

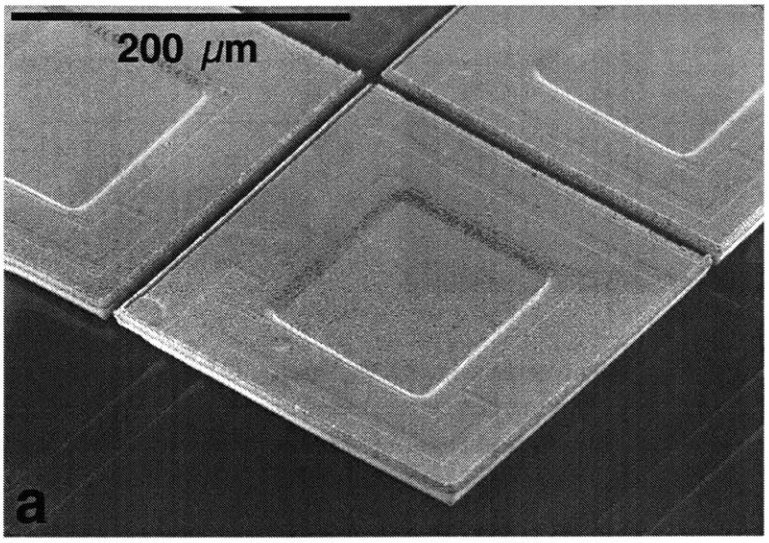

Figure 2-17: Microscope image of an early CDMS TES sensor to give a sense of scale involved in the manufacture of these TES sensors

2.4.2 CUORE Detectors

The CUORE experiment uses a simpler readout technique (shown in Figure 2-18) to read out the heat signal generated in their detectors, as CUORE does not look for an initial burst of phonons produced in particle interaction events. Threshold considerations are not as important as compared to CDMS, but now having a good energy reconstruction and resolution are main focuses of the CUORE readout system. This means that the readout scheme can focus on looking at the down-converted phonons generated on timescales of $\approx$ ms, after they have thermalized through the entire crystal. The sensors used in this endeavor are Neutron Transmutation Doped (NTD) Sensors which are glued onto the surface of the $Te0_2$ CUORE crystals. [34] The manufacuring process for NTD starts with a simple wafer of Germanium, which is then exposed to a neutron beam [13]. The neutron exposure results in the distribution of so-called 'conduction centers' individual atoms of Ga, As and Se which then act as dopants spread randomly throughout the bulk of the wafer. At high temperatures and electrons passing through the wafer can easily hop from one conduction center to

[13]The NTDs used on the CUORE experiment were exposed at the MIT Research Reactor, discussed as an experiment site in Chapter 4 of this thesis

another, which translates into a high electrical conductivity/low resistance. As the temperature falls, the electron wavefunctions become more and more localized around each conduction center, which means that the only way for current to travel through the wafer is through a mechanism called 'variable length hopping'. Here phonons present throughout the material act as a type of mediator that allowed for localized electrons to reach excited states where they can 'hop' to another conduction center. However; as the temperature falls lower and lower the electron wavefunctions become more localized requiring ever higher energy phonons to exite them into hopping, which means that electrons no longer flow as easily through the wafer. This result is the following equation for the the electrical resistance for $T \rightarrow 0$ known as the Mott-Anderson Law:

$$\rho(T) = \rho_0 \exp^{(\frac{T_0}{T})^\alpha} \tag{2.10}$$

where ρ_0 and T_0 are predetermined by the doping levels generated during the manufacture of the NTD readouts and are usually empirically measured. α represents an additional empirical parameter that can be fit to account for deviations in the variable length hopping due to imperfections in the NTD, for the ideal Mott-Anderson Law this parameter is equal to $\frac{1}{2}$. The end result of this is a readout sensor that has a well defined response curve to any small changes in the temperature- see Figure 2-14 over the course of a second. It is important to note that the sensitivity to changes in temperature increases as $T \rightarrow 0$, as the ΔR a fixed change in temperature increases as you lower the operating temperature.

2.4.3 Ricochet Detectors

The Ricochet experiment has proposed a different style of detector based on some of the superconducting physics found in the CDMS TES sensors. Up until now all the detectors we have discussed use semi-conducting crystals materials, read out by a semi or superconducting readout system. Ricochet seeks to use a superconducting single-phase crystal for its detector material, either Zinc or Osmium, due to their

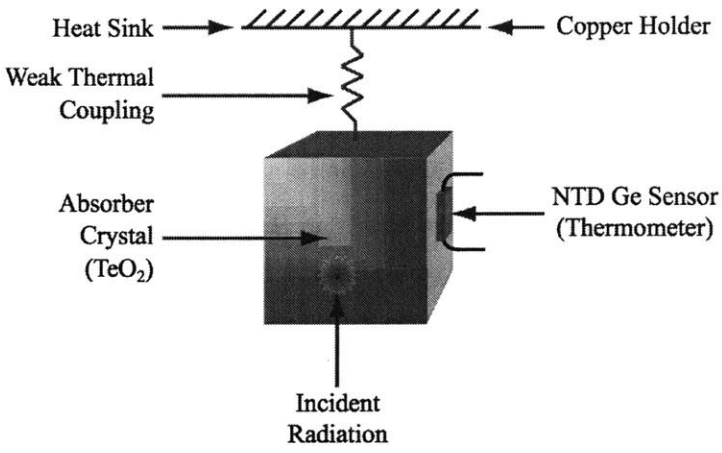

Figure 2-18: Typical CUORE bolometer setup. Taken from [35]

potential in screening out spurious background events.

One of the main problems with low threshold detectors comes in the form of electro-magnetic backgrounds, for example background γs from the surrounding environment, that can have a significant impact on your final sensitivity. These superconducting detectors seek to make their detectors as insensitive to these EM backgrounds by taking advantage of the various coupling times found inside superconducting materials. As these detectors go superconducting, their detector volume is filled with Cooper Pairs, which can be broken up into Quasiparticles, such as the Bogoliubov quasiparticles [33], discussed previously. Electromagnetic interactions, will predominently break up Cooper pairs into these Quasiparticles which can then recombine into a Cooper Pair, but in Zinc and Osmium the recombination time (labeled τ_r in Figure 2-19) grows to beyond a second as you cool the detector well below its T_c. Once the recombination occurs the Δ used to create the Quasiparticle in the first place is re-released as phonons. On the other hand, nuclear events, such as the recoil of a nucleus, will deposit their energy predominantly into the balastic phonons that CDMS had optimized their detectors to readout. This means that, if you design your readout to be fast/sensitive enough, you should see two components of any energy signal, first the phonons from the initial recoil event, and then a second slower signal

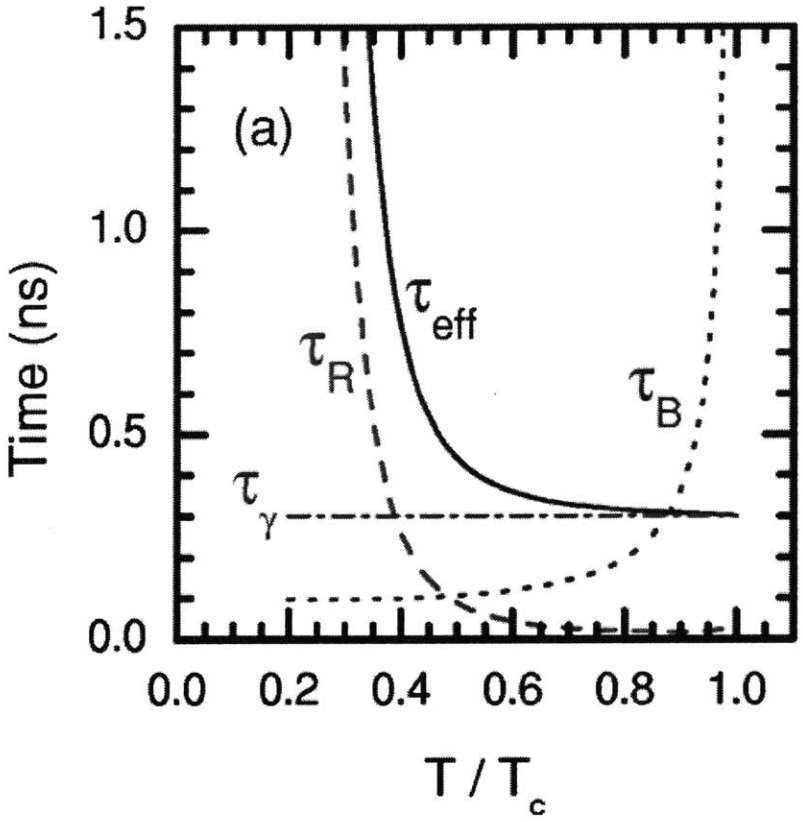

Figure 2-19: Superconducting Timing constants in Ricochet detector see [36]. In particular here τ_γ is the escape time for phonons to exit your crystal, which remains constant as you cool your crystal, while the recombination time, τ_R rises dramatically.

if there was any γ background component to the event. Now instead of performing background rejection based on the ratio between the ionization/phonon or scintillation/ionization etc... you can perform the same task using a single readout channel with the information stored in the pulse shape of each event.

2.5 Detector Materials

It is also important to take a quick look at some of the rationale in choosing specific detector materials used in all these experiments. While in Ricochet the choice was mostly driven by favorable superconducting physics found in Zinc, other experiments chose their detector materials based on other criteria. For example, on the CUORE experiment the detector crystal material TeO_2 was chosen as Te-130 has a high Q-value for the $2\nu\beta\beta$ reaction, well above many of the background processes that can dominate your background. At the same time the high natural abundance of Te-130 does not require expensive enrichment processes, allowing for larger exposures and therefore higher sensitivities to $2\nu\beta\beta$. In terms of cryogenic engineering it also has the distinct advantage of have similar thermal contraction properties as Copper, which matches a large percentage of the surrounding support framework. CDMS chose Germanium as their target material due to the extensive knowledge base built around the manufacture of high purity low-background large scale Germanium crystals. In addition, the nano-fabrication of sensors onto the surfaces of Germanium has had a long history that reduces the need for prototype R&D efforts. Moving to the next generation of CDMS, CDMS will continue to use these semi-conductor detectors in their deployment, but now due to the need to probe lower-mass dark matter models, a lighter semi-conductor material such as silicon will become more interesting moving forward (discussed more in the following chapter).

At the same time it is important to consider all the materials that will surround your detector, as shown in the COGENT [37] experiment, when their signal detection became attributed to surface events induced by the clamps surrounding their detector. The CUORE experiment has also placed a lot of effort into ensuring that all materials

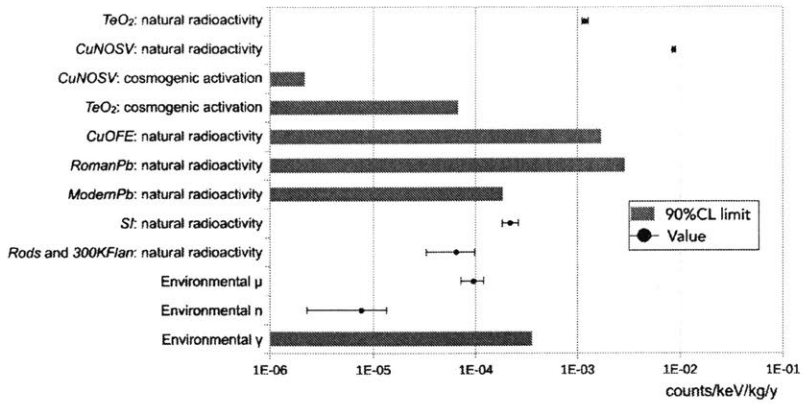

Figure 2-20: Summary of the CUORE background budget. Taken from [38]

that would be in close proximity of the crystal detector would have the lowest possible radioactive contamination levels as seen in Figure 2-20

To give a sense of the background levels required to run an experiment such as CUORE, take the two highest measured background radioactivity levels from Figure 2-20, the natural radioactivity of the TeO_2 and the CuNOSV (the background contribution from the copper support structures surrounding the detectors) is expected to lie around 10^{-3} and 10^{-2} counts/keV/kg/year respectively, which if you consider a 10 keV window around your signal peak in a 750 gram detector ends up contributing around 0.08 total events **per year** to your detector. This will be become the limiting factor in pushing forward into new parameter space with next generation $0\nu\beta\beta$ experiments, such as CUPID, where even more stringent background requirements will become the norm.

This all highlights the some of the major considerations [14] that go into planning of which material you wish to use in your rare-event search.

2.6 Conclusion

Rare-event searches have the unique challenge of requiring both massive experiments that simultaneously require extreme precision in order to have a chance of detecting

[14]There can also be some less practical considerations, such as the fact that working with Tellurium can make your breath smell like garlic for a while...

the phenomena they are after, while ensuring that their signal is not some spurious background event. Backgrounds can come in many different forms and must be carefully characterized in order to minimize their impact. New developments in the field of cryogenic infrastructure and readout technologies have made the construction of ever larger bolometer experiments possible. It is only through the construction of these massive bolometer experiments that we can begin to probe new and exciting area of parameter space in both Dark Matter and $0\nu\beta\beta$ searches.

Chapter 3

CDMSlite

"We are the world leading experts in making much ado about seeing 0, 1 or 2 events in our detector"

— Anonymous CDMS collaborator

3.1 Introduction to Dark Matter

The characterization of Dark Matter (DM) remains one of the most pressing issues in particle astro-physics today. While observations from the previous 70 years have yielded some interesting insights/clues into the nature of DM, we have yet to detect it with a terrestrial detector. From our observations, which encompass a deserve range of techniques/probes, we know about the vast time, length and mass scales that this mysterious matter plays an integral part in. We know that DM makes up a large percentage of the total matter density - see Figure 3-1 - of our universe and that it only seems to, at best, weakly interact with the known types of matter that we are most familiar with. While the name dark matter originally came from the fact that during early visual evidence for this matter had no accompanying EM signal, thus dark matter. This name continues to be fitting to this day as we continue to be "in the dark". We do not know for sure if all this dark matter is made up of a single particle or rather constitutes an entire "dark sector", whose interactions and processes are currently beyond our current theories. While it is difficult to makes any precise

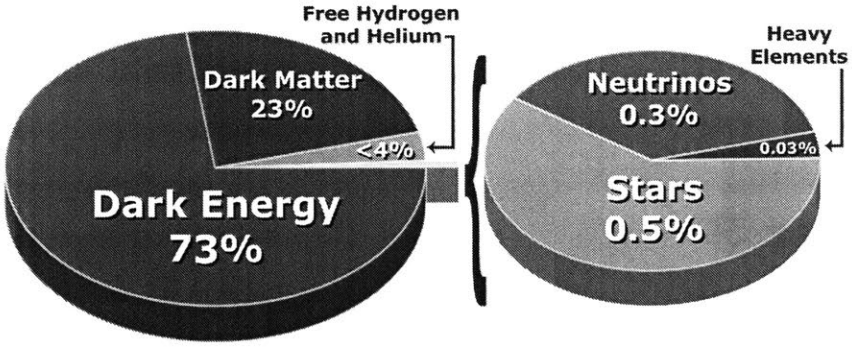

Figure 3-1: Dark Matters makes up a large percentage of the matter density of the universe. The majority of the total mass-energy density is tied up in Dark Energy, which is well beyond the scope of this thesis. Taken from [13]

statements about the nature of this mysterious matter, in this chapter we will briefly discuss some of the evidence that we have for DM, one possible candidate for what DM is and one experiment that sought to probe specific models of this candidate.

3.2 Dark Matter Framework

Our current understanding in modern cosmology of large scale structures in the universe is based on the Robertson-Walker spacetime metric or perturbations on this metric, which assumes a isotropic and homogeneous universe. While we know about some of our local 'inhomogeneities', such as galaxies and our local galactic neighborhood, at the very largest scales, our observations indicate that the universe is approximately as such, which means that at all points in the universe the rest of the universe looks the same in all directions. Knowing that we can approximate the universe as homogeneous and isotropic we can then begin to characterize the structure of the universe using this Robertson-Walker metric[1]:

$$ds^2 = dt^2 - a^2(t)[\frac{dr^2}{1 - Kr^2} + r^2 d\Omega] \tag{3.1}$$

where:

[1]In mathematics, a metric is a way of calculating the distance between two point in a given space

$a(t)$ is the *scale factor* that sets the overall length scale at a given time t

$d\Omega$ is the solid angle in 3 dimensional space given by $d\theta^2 + sin^2\theta d\phi^2$, where here we use the usual convention of (r,θ,ϕ) for the angles and position

K is a parameter that can vary between -1 and +1 depending on the curvature of the space it is currently describing. Current observations seem to indicate that for our universe the value is very close to 0, corresponding to a flat geometry.

For all the subsequent discussions I will define an additional constant/parameter, the Hubble constant $H \equiv \frac{\dot{a}}{a}$, [2] which measures the rate of expansion of the universe and is an parameter that we can measure. We can broadly divide mass-energy of the universe into three components, vacuum energy, non-relativistic matter and relativistic matter. Before we start solving the above equation for our we can write out how we expect different types of matter/energy densities to evolve as a function of time. Given the Roberston-Walker metric we need to calculate the dynamical evolution of the universe, which is done via the Einstein equation:

$$R_{\mu\nu} - \frac{1}{2}g_{\mu\nu}R + \Lambda g_{\mu\nu} = 8\pi G T_{\mu\nu} \tag{3.2}$$

where:

$R_{\mu\nu}$ and R: are the Ricci tensor and scalar respectively

G: the well known Newtonian gravitational constant

$T_{\mu\nu}$: the stress-energy tensor, on the scales we are interested in we can treat all the 'stuff' in the universe as if it behaves like a 'perfect fluid', which means that it has no viscosity or heat flow. Therefore we can write this stress-energy tensor quite simply as $T_{\mu\nu} = diag(-\rho, \rho, \rho, \rho)$

ρ: energy density of the universe at a given time t

[2]Newton's notation (known as dot notation) is only widely used in the field of classical mechanics and cosmology, this only came about due to the rivialiy between the Liebnitz and Newton camps during the early years of calculus and the Newton camp developed the early tools of classical mechanics, fun little historical note

$g_{\mu\nu}$: is the space-time metric tensor

Λ: the cosmological constant, for many years this was assumed to be zero [39], but in the past 20 years there has been renewed interest for precise measurements of this parameter due to far-reaching implications it would have for cosmology, for our discussions we will include this term for completeness

Now let us examine the energy density, ρ, a little more closely, specifically how it evolves as a function of the length scale a and therefore by extension time. For non-relativistic matter consider a cube with sides a_0 in space with a fixed mass with corresponding to an original density ρ_0 . If you change the length of each of the sides relative to the original length, but keep the total mass contained within the cube constant you arrive the relation $\rho(t) = \rho_0(\frac{a_0}{a(t)})^3$. For relativistic densities, such as expanding photons gases, additional considerations must be taken into account as we can no longer use mass to 'fix' the density at a specific time. From statistical mechanics, we know that $\rho \propto T^4$, where T is the temperature of the gas and the entropy, $S \propto VT^3$. Now, assuming an adiabatic expansion to universe we can deduce that $T \propto \frac{1}{a(t)} \implies \rho = \rho_0(\frac{a_0}{a(t)})^4$. Finally, we can characterize the vacuum energy as constant throughout any given volume ρ_V, which does not change over time. Now we can go about solving for $a(t)$ the Einstein equation using our metric and the parameters defined above which gives the following equation (known as the Friedman equation):

$$H^2 \equiv (\frac{\dot{a}}{a})^2 = \frac{8\pi G\rho}{3} - \frac{K}{a^2} \tag{3.3}$$

Using the relations between ρ and $a(t)$ discussed previously we can go ahead write down the evolution of $a(t)$ for different type of mass - see Table 3.1. Something

Now we can write the total energy density as follows:

$$\rho = \frac{3H_0^2}{8\pi G}[\Omega_\Lambda + \Omega_m(\frac{a_0}{a})^3 + \Omega_R(\frac{a_0}{a})^4] \tag{3.4}$$

where $\Omega_\Lambda, \Omega_m, \Omega_R$ represent the individual fraction of the total energy density that is made up of Vacuum energy, non-relativistic and relativistic matter respectively. For

Type of Matter/Energy	Evolution
Non-Relativistic Matter	$a(t) \propto t^{\frac{2}{3}}$
Relativistic Matter	$a(t) \propto t^{\frac{1}{3}}$
Vacuum Energy	$a(t) \propto exp(Ht)$

Table 3.1: Summary of the time dependence of various scale factors that correspond to various types of matter. Important to note is that the density of all three types of matter indicate that the universe is actually expanding with time.

dark matter searches we often divide $\Omega_m \equiv \Omega_b + \Omega_c$ where Ω_b represents baryonic matter and Ω_c is everything else (spoiler alert: the non-baryonic dark matter the c stands for *cold*). While there is some minor tension between all the various measurements, the consensus is that $\Omega_m h^2 \approx 0.15$ and $\Omega_c h^2 \approx 0.13$ [3]. What this means is that if you just look at all the mass of the universe, the overwhelming majority of it comes in form of non-baryonic matter - see Figure 3-1 . From our astronomical observations, we have observed something that seems to make up the majority of the matter in the universe and yet it does not emit light or interact via the normal interaction methods that we know of, thus the name 'dark matter'.

3.3 Observational evidence for Dark Matter

3.3.1 Rotation Curves

The earliest evidence for dark matter came from observations of the rotations speeds of the luminous matter in nearby galaxies, which seemed to imply that there was some additional mass pulling on objects at higher radii in galaxies. Using the toy galactic model of a perfectly uniform axisysmmetric rotating mass about its center one can deduce, using only Newtonian gravity, that the velocity of objects at a radius r from the center should go as $v(r) \propto \sqrt{\frac{M(r)}{r}}$, where $M(r)$ corresponds to the mass contained in a circle of radius r. The main techniques for measuring this in other galaxies come from measuring the redshift of atomic lines for objects at various distances from the center of rotation. Common spectral lines used in this technique are the famous

[3] Here h^2 is the Hubble Constant

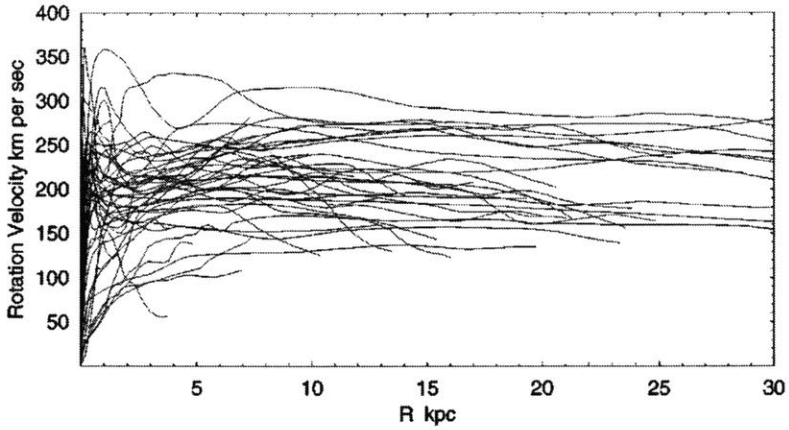

Figure 3-2: Summary of the $H\alpha$, 21-cm and CO data to generate galactic rotation curves as a function of radius. Taken from [40]

$H\alpha$and 21-cm Hydrogen hyperfine transition lines as well as the CO lines at 2.6 mm and 1.3 mm [4] [40]. Looking at the results presented in Figure 3-2, one immediately can see that the velocity does not drop as a function of radius, rather seems to increase and then keep roughly constant. The only way this behavior could be observed is if $M(r) \propto r$, which does not agree with observations of the luminous observable matter.

One other observation of that provides evidence for dark matter comes from observations larger scale structures such as the Bullet Cluster - shown in Figure 3-3, which is a collection of galaxies currently in the process of colliding. Stars and galactic plasma emit very characteristic wavelengths of radiation in the visible/IR and x-ray bands respectively, allowing us to visually inspect where the largest concentration of stars lie in a large scale structures. At the same time, gravitational lensing bends light from sources behind massive structures depending on the total amount of mass that the light could interact with. Gravitational lensing gives us a handle on where the majority of the total mass of the system lies, interestingly the center of mass does not correspond to the center of luminous mass. This indicates some that some large fraction of the total mass of the combined system did not interact and simply travel through the opposite cluster, which is more akin to a collision-less gas rather interacting matter particles. This observation also allows us to infer some of the properties

[4]This lines correspond to the J = 1 → 0 and J = 2 → 1 transitions in CO respectively

Figure 3-3: Chandra x-ray observations (pink) overlaid from gravitational lensing surveys (blue) overlaid on a Hubble image taken of the Bullet Cluster - taken from [41]

of this dark matter, specifically its non-bayronic nature, as otherwise it would have produced some measure of X-rays.

As an interesting side note, observations of the bullet cluster also provide us with the ability to make a measurement on the ρ_m corresponding to the Ω_m value discussed previously. From the combined Candra and gravitational lensing data we can infer the total mass (M), which when combined with the cluster luminosity (L) and the total luminosity density of the universe (ℓ), one can write:

$$\Omega_m h^2 = 0.15 \pm 0.05 \tag{3.5}$$

3.3.2 CMB measurements

Measurements of the Cosmic Microwave Background (CMB) have given us the most precise measurements of all energy densities (ρ) to date. The CMB comes about as a remnant of the conditions found in the early universe. As the primordial plasma of the early universe went through recombination forming neutral hydrogen, the free

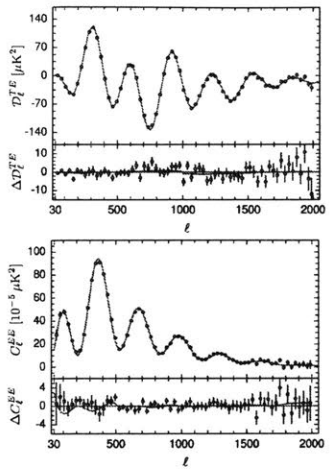

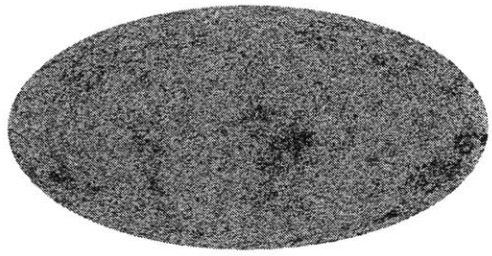

Figure 3-4: (left)CMB Power Spectrum in both the TE and EE polarization models along with the corresponding residuals. Taken from [44] (right) High Resolution Image of the CMB taken with the PLANK satellite, for a sense of scale the maximum resolution of these images corresponds to a change in temperature of the sky of about 1 in 100000.

photons in the universe suddenly had a much longer mean-free path to the point due to the relative lack of interaction between these photons and neutral hydrogen. After this last interaction with matter, these photons are free to stream all the way to our instruments with very little interference from other natural sources, forming a 'snapshot' of the universe at this critical juncture [42] [43]. As the universe expanded, these photons gradually got shifted into the microwave band. To zeroth order, these microwave photos form a isotropic blackbody spectrum, however; as you increase the sensitivity of your measurements one begins to notice anisotropies in this background spectrum, caused by structures found in the early universe. Similar to how you can reconstruct most mathematical functions as a Fourier series, you can map out the 'function' as a series (indexed by l, the multi-pole moment) of component functions, in this case the spherical harmonics. Broadly speaking the various multi-pole moment corresponds to structures on the scale of the inverse of the multi-pole moment, with $l = 10$ corresponding to structures with a size of 10 degrees and $l = 100$ corresponding to structures on the scale of 1 degree. From the framework laid out in the previous section, one can then make predictions for how the various energy densities (and therefore the corresponding Ωs) impact the formation of various structures at

the various length scales. The specifics of how the various Ωs are extracted from this map are beyond the scope of this thesis, but the Particle Data Group does contains a good overview of some of the calculations and the impact of individual parameters/errors [45] to the final fit but for our discussion the final values that come out are (from [44]):

$$\Omega_b h^2 = 0.02230 \pm 0.00014 \tag{3.6}$$

$$\Omega_c h^2 = 0.1188 \pm 0.0010 \tag{3.7}$$

$$\Omega_m h^2 = 0.1417 \pm 0.00097 \tag{3.8}$$

The values are the final combined fits using a combination of all the various datasets available to the PLANCK collaboration including polarization and gravitation lensing data, the impact of the inclusion/exclusion of these data sets are again beyond the scope of this discussion. The important item to note is that these values are consistent with the Ω_m value obtained from the cluster data, which confirms the underlying total mass density of the universe, while also adding in the contribution of dark matter to these values.

3.3.3 Other measurements

For the sake of brevity, there are other measurements of the various Ωs which we can not cover in depth here, but we can list here for completeness, for a full discussion of these measurements I point the reader to [46]:

- Type Ia Supernovae - Type Ia supernovae are the result of binary white dwarf where one of the white dwarf has accredited enough matter from its partner. Once the heavier partner has gathered enough material and passes the Chandrasekhar limit, the maximum mass that can be supported through electron degeneracy pressure, the white dwarf grows increasingly unstable and extremely hot allowing for the production of heavier elements beyond Lithium [47]. This limit provides a very sharp cutoff to the masses of white dwarfs, which then go supernovae, providing observationlists with a standard candle that have a

fairly uniform amount of fissile material and peak luminosity. Knowing this you can use these supernovae to measure distances on cosmic scales, which then allows you measure the relative size of the universe at different times [48]. As dark energy and the matter components of the universe provide the acceleration/braking mechanisms for the expansion of the universe, you can then fit the expansion of the universe at different times, corresponding to different redshifts z as shown in Figure 3-5 The resulting fits result in the following values for Ω_b [48] :

$$\Omega_b h^2 = 0.028^{+0.09}_{-0.08}(statistical)^{+0.05}_{-0.04}(systematic) \tag{3.9}$$

- Big-Bang Nucleosynthesis (BBN) - During the early stages of the universe all the matter, including baryonic matter such as proton/neutrons, was tied up in a constant state of annihilation/creation. As the universe cooled, individual particles began to form and could then begin to make heavier/more complex forms of matter, such as the lighter elements up to Lithium-7. Heavier elements beyond Lithium-7, the so-called metals in astronomical parlance, would have to wait for other production mechanisms in the interiors of stars to come about in significant quantities. Using the well-documented cross sections for the production of Helium-3,Helium-4 and Deuterium using free protons/neutrons, one can assign a probability and therefore a total abundance of these lighter elements that formed the initial basis for all the reactions in our universe. These models, which fall the umbrella of Big-Bang Nucleosynthesis (BBN), predict a abundances based on the initial baryon density and a parameter η, which corresponds to the relic blackbody photon density, in the early universe. Using observations of high redshift quasars corresponding to very early periods of the universe, specifically the ratio of Deuterium/Hydrogen in their spectra one can check the predictions of BBN for these early times. The result is a constraint on the overall baryon density of the early universe, where:

$$\Omega_b h^2 \in [0.021, 0.025] \tag{3.10}$$

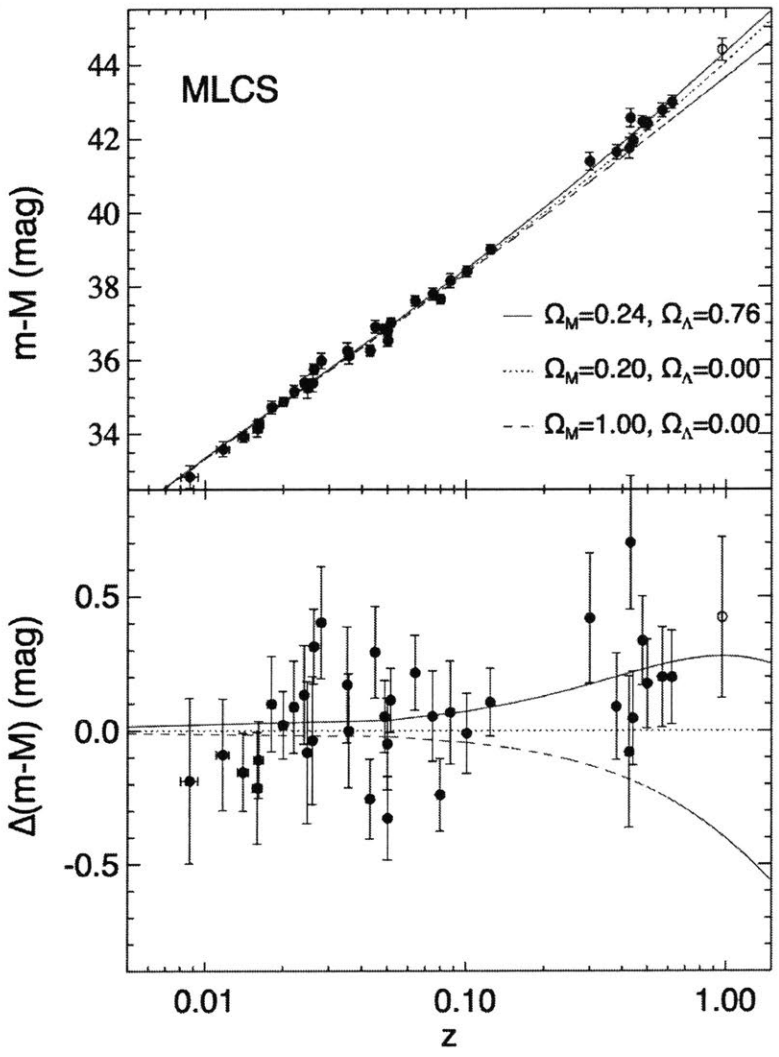

Figure 3-5: Supernovae models and their corresponding fits/residuals - taken from [48]

However; all these measurements paint a consistent picture for the makeup of the universe, namely that matter only makes up a fraction of the total energy density of the universe. If you then only look at the matter component in the universe a large proportion of it is composed of non-baryonic matter that for sure only interacts via gravity.

3.4 WIMP Dark Matter

From the evidence provided in the previous section one can then begin to create a list of requirements for a particle to be dark matter, namely:

- Stability - Any dark matter particle crated in the early universe continues to play a role in galactic dynamics even to this day, without producing any type of visible decay signature
- Electrically neutral - From the bullet cluster measurements we can see that the dark matter particle simply passes through itself as a frictionless gas, which means that there was no electrical interaction between the dark matter particles slowed down its movement
- Interaction via gravity - from the galaxy rotation curves, this is the only force that we know for sure dark matter seems to interact with
- Produced in the early universe - from CMB measurements we know that a significant portion of the matter density in the early universe was non-baryonic and seemed to brake the expansion of the universe via gravitational pull. This component has been accounted for with the inclusion of dark matter.

From this we can draw up various theories that generate particle than can fulfill the above requirements, in particular we will focus on the WIMP, the Weakly Interacting Massive Particle. From the all the evidence we discussed in the previous section, we did not include any limits on the weak nuclear force, which opens up the possibility that dark matter interacts via gravity **and** the weak force thus the *weakly interacting*

part of a WIMP. Direct detection searches, such as CDMS (Cryogenic Dark Matter Search), have specialized on detecting this spices of dark matter due the relative ease in building a detector to search for it and have placed limits on the nucleon-DM interaction strength of this dark matter candidate. There are multiple reasons why WIMPS have become a favored dark matter candidate for direct detection searches. First the so-called 'WIMP miracle', was mechanism by which you could generate the modern-day observed dark matter density (Ω_c), by creating a particle during the early universe that would freeze out of thermal equilibrium at a time associated with weak-scale masses and cross sections. The WIMP miracle consisted of two parts starting with an initial freeze out of these WIMP DM particles from the initial furnace of the early universe. Coupled with the decreasing number density of these particles this would eventually result in fewer interactions between these particles and then result in the relic density observed today - summarized in Figure 3-6. While the standard model has been a mainstay of the particle physics world for the past 50+ years, phenomena such as neutrino mass and dark matter have prompted searches for physics Beyond the Standard Model (BSM), including supersymmetric models. The trademark of these supersymmetric models is the creation of *superpartners* corresponding to each of the particles found in the standard model, for dark matter searches neutralino, a distinct combination of 3 other super-symmetric partners, has gained traction as a dark matter candidate [50]. The final component to this model is the expected mass of these new dark matter particles. By constructing a thermal model for the freeze out of the dark matter particle coupled with some dimensional analysis for the cross sections as outlined in [46], one can determine that Ω_c scales as the square of the dark matter mass and that once you plug in numbers you can determine a range of plausible dark matter masses $\in [\approx\ 10\ GeV, \approx\ 1\ TeV]$. However; this range is approximate and many theories have been developed that can extend this plausible mass range to include even lighter WIMPs. For a full discussion of the theory behind these low mass models, I point the reader towards dedicated dark matter thesis's including [46] [5].

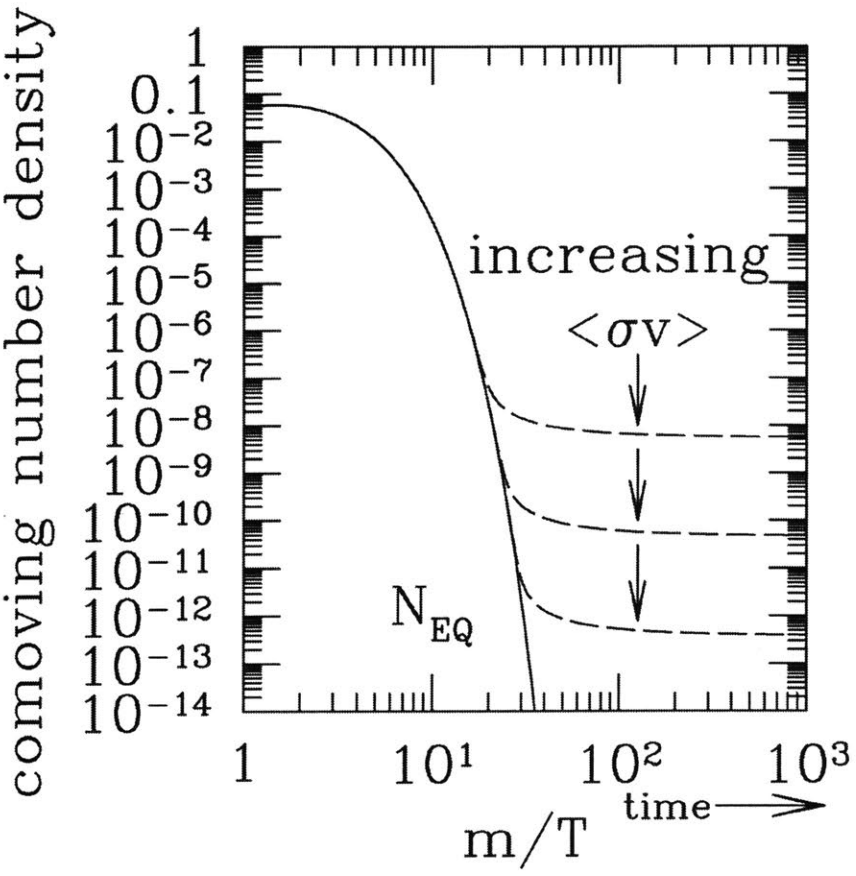

Figure 3-6: Illustration of the WIMP miracle, the three dashed lines correspond to different interaction cross-sections which after some time would result in the relic density observed today, as seen in [49]

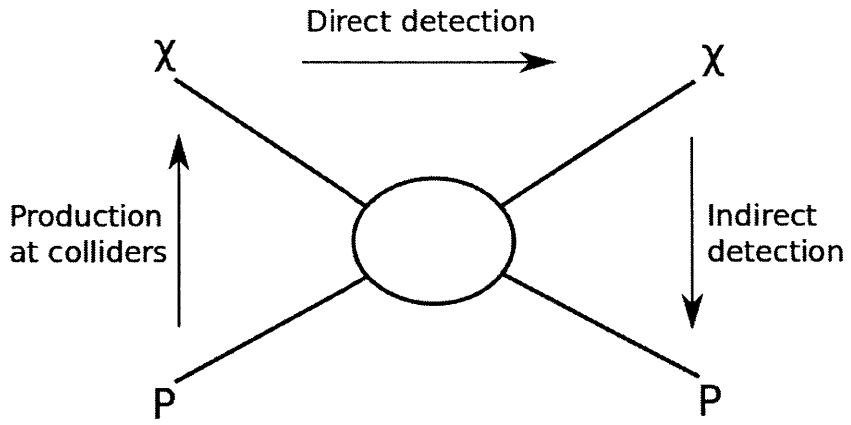

Figure 3-7: Illustration of the ways that we have attempted to detect dark matter

3.4.1 WIMP Detection

Now that we have discussed some of the theory behind dark matter, how does one go about detecting it with terrestrial detectors? There are currently three main ways to go about detecting dark matter as illustrated in Figure 3-7:

- Production at collider: Discussed in detail in Chapters 13-15 of [51]. In broad strokes, large scale colliders, such as the LHC have the potential to create dark matter particles in their collisions. If created, these the dark matter particles would appear as 'missing energy' in the final energy budget of an event. While competitive limits on dark matter interaction cross sections have been produced by collider experiments, they are often model-dependent and it is difficult to compare the resulting limits from colliders with indirect and direct detection searches.

- Indirect detection: Discussed in more detail in Part V of [51]. These searches focus more on astrophysical observations in various bands, looking for an excess in signal coming from areas of the sky expected to have a larger concentration of dark matter. In recent years there have been numerous possible signal excesses coming, for example, from the center of the galaxy [52]. One of the main problems associated with these searches comes from other astro-phyical background

sources, that if improperly accounted for, could mimic a dark matter induced excess signal. In addition, the conversion of a background excess into a dark matter signal is heavily model dependent, depending for example on the dark matter production model.

- Direct detection: These experiments work on the premise that the earth is traveling through a dark matter cloud with a relative velocity and density determined from astrophysical observations. WIMP dark matter in particular, could the directly interact with your experiment at a specific rate 'pinging' your detector. These 'pings' would be extremely low energy interactions that require low threshold, large mass experiments such as CDMSlite. The main disadvantages of this method come from experimental/engineering/financial requirements in the construction of extremely low background detectors in deep underground labs. In the remainder of this chapter I will focus on these types of searches. For more details I refer you to Part IV of [51].

3.5 CDMSlite

Between 2011 and 2014 the CRESST, COGENT, DAMA and CDMS (for a full report on the status of DM searches I point the reader towards the PDG review in [53]) collaborations reported possible DM signals in the "low mass regime" of dark matter (less than $\approx$ 10 GeV), spurring great interest in new experiments and techniques that could probe these low mass WIMPs. From a theory standpoint, these light dark matter particles are motivated by the Asymmetric Dark Matter (ADM) models within the supersymetry framework. These ADM models creates higher order operators that couples the observed ratio of $\Omega_c/\Omega_b \approx 5$ to the measurements of η, the ratio of the number densities of baryons (and anti-baryons) to photons, from BBN observations discussed earlier. By then saying that the observed value of η act a type of seed, wherein the matter/anti-matter particles interact and annihilate each other leaving only the asymmetric remainder as the number density that we observe today. The effect of this is that the number densities of both dark matter and regular matter

are approximately equal. This means that you can scale the window of possible wimp dark matter theories down by a factor of $\Omega_c/\Omega_b \approx 5$ to masses closer to 1 GeV depending on the model used. The challenge in detecting these lighter forms of dark matter comes in the form of the maximum expected recoil energy per event even by:

$$E_{maxrecoil} = \frac{m_{DM}v^2}{2}\frac{2m_N}{m_{DM}(1+m_N/m_{DM})^2} \tag{3.11}$$

Which when you plug in numbers gives you a nuclear recoil energy of $\approx$ 1 keV for a 10 GeV WIMP traveling at 10^{-3}c [5]. The impact on the necessary thresholds for dark matter searches is then clearly shown in Figure 3-8, decreasing the threshold by a factor of 4 increases the total number of counts (and therefore improves your expected sensitivity) by an order of magnitude.

CDMSlite allowed you to decrease this threshold by increasing the potential across your detector to generate additional Luke-Neganov phonons (see discussion of phonon physics in bolometer chapter - see 2). These additional phonons allowed you to amplify very small signals therefore decreasing your effective threshold. The exact setup and discussion of how all the experimental parameters were determined are discussed in much more detail in [5], [55] and [46]. Throughout this discussion it is important for the reader to bear in mind that all this analysis was performed with only one of the 15 detectors on CDMS, chosen via its energy resolution and noise performance. One important item to note are the two energy scales used in CDMSlite, the Nuclear Recoil (NR) and Electron Equivalent (EE) energy scales. Most background and calibration processes, produce more ionization energy per event than a pure WIMP-induced recoil signal, which should produce a pure phonon signal. While most calibration sources, for example Barium-133, produce multiple clearly defined signal peaks in the electron-equivalent energy scale, it is difficult to produce clear peaks in the pure nuclear recoil band especially at the lowest energies ($\approx$ 10 keV and lower) near threshold. To calibrate the nuclear recoil band, the CDMSlite

[5] an often overlooked component to these dark matter models comes in the form of the dark matter velocity distribution, for consistency all experiments assume a Maxwell-Boltzman velocity distribution with a Standard Halo Model, but this is by no means the only model out there, for a review I point the reader to [54]

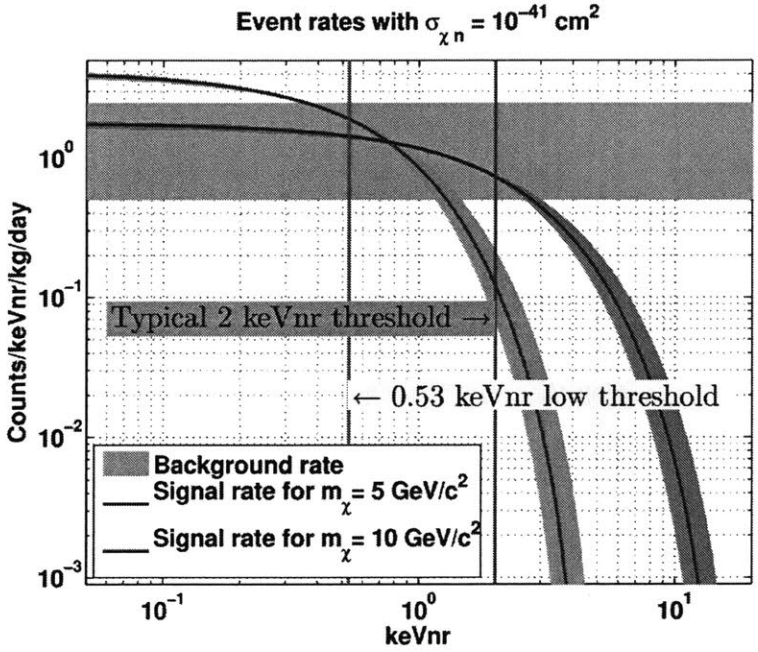

Figure 3-8: Differential Event Rate in CDMSlite for a different dark matter masses given a cross section for two different detector thresholds. The green band on the top represents the expected background rate that CDMS expected at the Soudan site. From [55]>

team created a conversion factor[6] between the NR and EE bands, based on the Luke-Amplification factor, given by:

$$E_{NR} = E_{EE}\left(\frac{1 + \frac{eV_{bias}}{\epsilon_\gamma}}{1 + Y(E_{NR})\frac{eV_{bias}}{\epsilon_\gamma}}\right) \tag{3.12}$$

where:

V_{bias} represents the bias voltage run across the detector, set at 69 Volts due to the best signal to noise ratio observed at that bias

ϵ_γ the energy needed to create an electron-hole pair in Germanium ($\approx$ 3 eV)

$Y(E_{NR})$ is the yield of an event within the CDMS as characterized by the Lindhard parameterization. Yield is one of the most important varibles in CDMS as it allows an event-by-event discrimination between signal and background events given by: $\equiv \frac{E_{ChargeChannel}}{E_{PhononChannel}}$. The specifics of this term as well as a discussion regarding the Lindhard potential are discussed in the previous chapter.

The main advantage of this method comes from the fact that you can use the normal calibration data to calibrate the possible response of your detectors to nuclear recoils. The downside of this method comes from the fact that you place a heavy emphasis on the parameters fed into the Lindhard parameterization of the yield, most clearly seen in Figure 3-9

As you lower your threshold, noise and other spurious events become increasingly important to identify and they grow in number exponentially at low energies. The purpose of the data cuts described below was to cut out as many of these spurious events while passing as many actual signal events as possible. Note that the studies presented here were done on the CDMSlite run 2 dataset and represent the first pass through of this dataset and represents the status of the analysis chain during the summer of 2014. These analysis techniques were further refined and updated by the CDMSlite team with the final results presented in [55].

[6]See Equation 8 in [55]

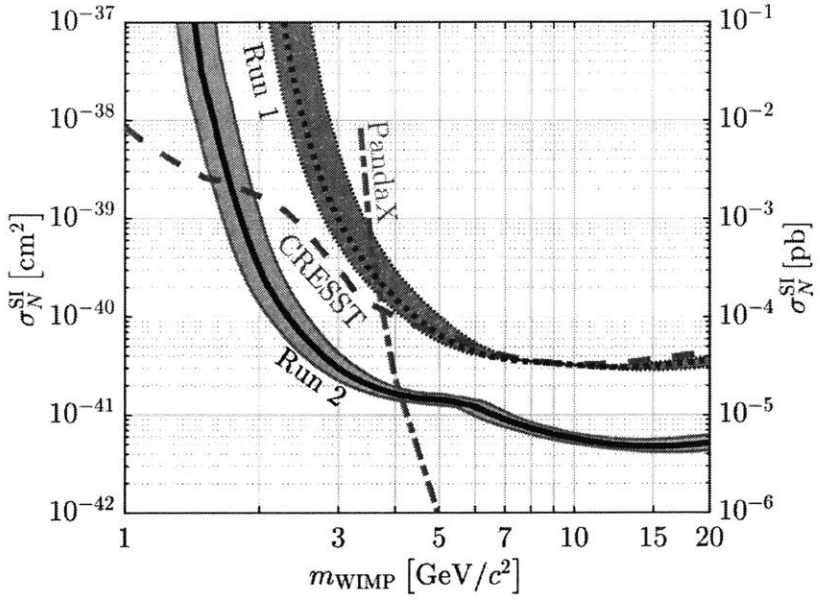

Figure 3-9: Zoomed in limits from CDMSlite runs 1 and 2. The yellow bands and red bands surrounding the limits from runs 2 and 1 respectively specifically correspond to the systematic errors due to uncertainties in the Lindhard parametrization. From [55]

3.5.1 Glitch Cut Calculation

Within CDMS a 'glitch event' was an event that had much sharper rise and fall times compared to a typical phonon/ionization pulse, as seen in Figure 3-10a. The exact origin of these events comes from a wide variety of sources and is an ongoing analysis project, but for this analysis they are simply treated as background and filtered out of the final dataset of pulses. For this first pass through the data a single glitch template was used to identify pulses, later CDMSlite analyses used multiple glitch templates that pertained to specific glitch event populations, but for this discussion we will only use the one template. The main way glitches were indentified was through their $\Delta\chi^2$ from the optimal filter. The theory behind the optimal filter is discussed more in detail in Appendix B of [56], but I will summarize it here. If you imagine every event as a combination of a scaled ideal pulse shape plus noise: $v(t) = As(t) + n(t)$ when you take the Fourier transformation of every pulse it would return the combination of the Fourier transforms of each of the pulse components. From random triggers you know what the pure noise looks like in both time and frequency space, which means

if you see any deviation from that power spectrum in frequency space you could then deduce that something besides noise had occurred during that time. By comparing how the power spectrum changes given various amplitudes of signal plus noise you can create various fitting criterion in frequency space. On CDMS the following basic criterion[7] was used:

$$\chi^2 = \int_{-\infty}^{\infty} df \frac{|(\widetilde{v(f)} - A\widetilde{s(f)})|^2}{J(f)} \tag{3.13}$$

where:

$\widetilde{v(f)}$, $\widetilde{s(f)}$ are the Fourier transformations of the total pulse and signal template respectively

A is an estimate of the amplitude of the signal/scaling factor of your signal template, can be used later to estimate the total energy of your pulse

$J(f)$ is the noise Power Spectral Density (PSD) of the noise

If three is no noise and your pulse matches your signal template exactly you get a χ^2 of zero, but we work in a environment full of noise that stems from your electronics, pulse tube vibrations in your cryostat or even a massive construction site directly outside the lab. The glitch cut is designed to as efficiently as possible select only these glitches while minimizing any loss of signal events to the analysis cut. First we defined a new pulse shape parameter, $\chi^2_\Delta = \chi^2_{OF} - \chi^2_{Glitch}$, which combined the fitting criterion from above generated from glitch and signal pules templates. With this sign convention pure signal pulses produce very negative values, while pure glitch pulses produce positive values. The question becomes at what value to set the cutoff point in this parameter such that especially at lower energies the loss of signal events is minimized. For extremely low energy pulses the Optimal Filter often finds it difficult to reconstruct the full pulse shape, resulting in the merging of all the various event populations into one large blob of events at lower energies as seen in Figure 3-11. To

[7] I am making a ton of simplifications here for the sake of brevity. There is an entire field of optimal filter theory wherein you can add additional scaling and offset factors and additional terms to account for things like correlations across bins or unknown trigger times etc... for more details I point you to Appendix B in [56]

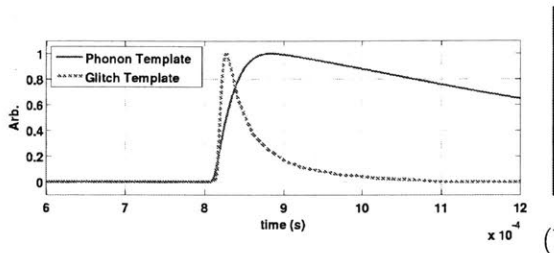

(a)

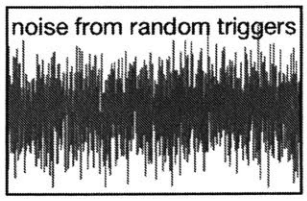

(b) Example noise pulse drawn from CDMS data

Figure 3-10: Example average phonon pulse (red) and example average glitch pulse (yellow) drawn from CDMS data - Figure a. Both pulses have been normalized such that their amplitude ends up being 1, which is then scaled to the energy you want to test for in the dataset. Interesting the averaging process also allows you to create so-called 'zero noise' templates which then require the addition of noise collected from random triggers (Figure b) in order to simulate true pulses

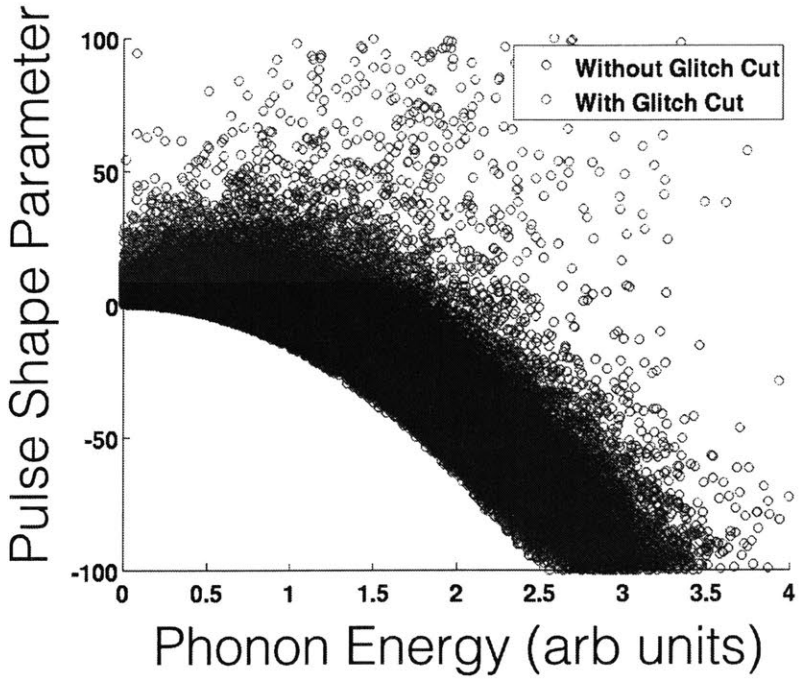

Figure 3-11: Actual CDMSlite data, not simulation. Green events are events that are tagged as glitch events via a pure χ^2_{Glitch} cut, which is why there are glitch events in the signal band. The pulse shape parameter on the y-axis is given by χ^2_{OF}-χ^2_{Glitch}, which means that pulse events will have a large negative values and 'pure' glitches will have large positive values. Cutoff value in this pulse shape parameter selected to be ≈ 10

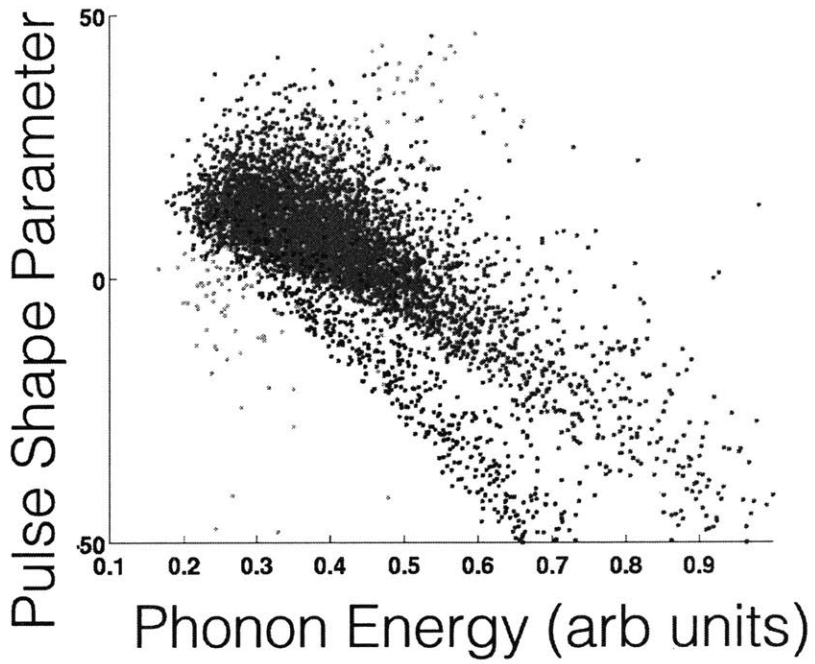

Figure 3-12: Simulated various event populations. Blue = scaled signal pulses plus noise, Red = scaled glitch template plus noise, Green = pure noise events

this end we undertook a series of simulations wherein we generated three different event populations: scaled pulse events (pulse template+noise),scaled glitch events (glitch template + noise) and pure noise events and then passed these events through the CDMS analysis chain. The specific ratios of events was chosen based on previous estimates of the sizes of the various populations gathered during CDMSlite run 1. Using the simulated events in Figure 3-12 one can clearly see that the glitch events tend to reconstruct to a χ^2_Δ band that lies above the signal band, which prompts the use of a larger χ^2_Δ cutoff. In the end we kept the cutoff value (Keep all events with χ^2_Δ < 10) that had been determined by Rito on the CDMSlite Run 1 data. This was done as the passage fraction of signal events was shown to be above 90 percent with this cut even at the lowest energies. After I left CDMS this analysis was continued refined further to include multiple χ^2_Δ, which used the differences in χ from multiple glitch templates that corresponded to various populations of glitches that were discovered. For a full discussion of the final glitch cuts that were utilized in the analysis of the

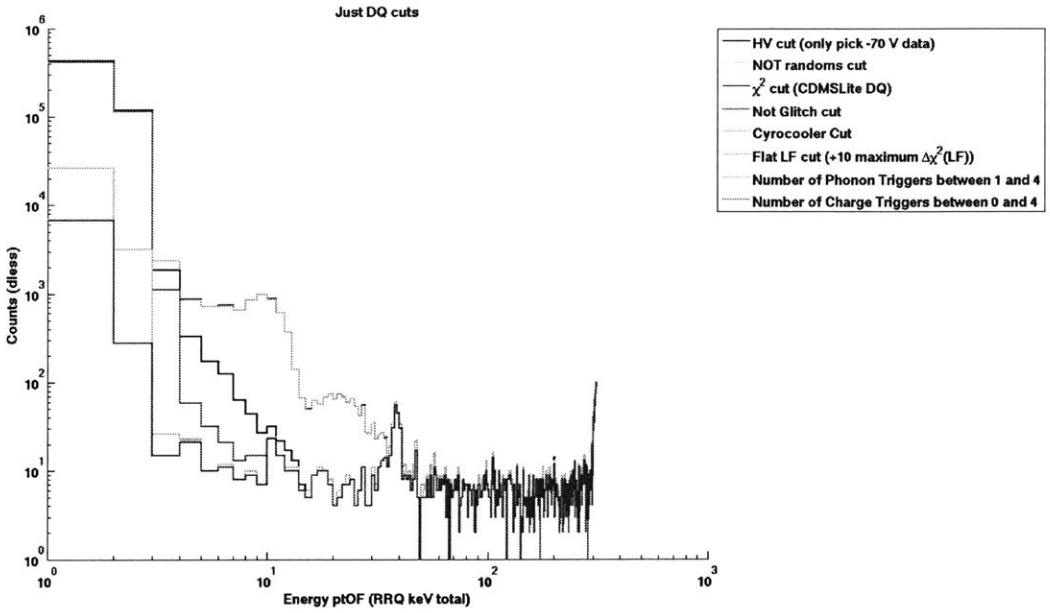

Figure 3-13: Energy histrogram showing the individual effect of all the various DQ cuts applied to the CDMSlite data. N.B. these were not the final cuts applied to the CDMSlite data, these were the preliminary cuts applied during the first pass through the CDMSlite Run 2 data in 2014/5. For the final analysis cuts applied see [55]. For reference rise seen at $\approx$ 300 ptOF corresponds to the 10.37 eV K-Shell electron capture in Germanium, which highlights the fact that this is a not a calibrated spectrum

Run 2 data I refer the reader to section 2 of [55]

3.5.2 Trigger Efficiency

The glitch cut described in the previous section, was just one of the data quality cuts that would be applied to final dataset, each one having to be optimized to have the largest signal pass fraction while at the same time rejecting as many background/spurious events as shown in Figure 3-13 Reducing the analysis threshold combined with increasing your exposure are the main ways that dark matter experiments push down into new areas of dark matter parameter space. However; increasing the exposure of an experiment often comes with with a hefty price tag as many times the largest expenditure in the operating budget of a rare-event search. As shown/discussed in Figure 3-8, even a small reduction in your analysis threshold can have a major impact on the final number of expected counts and therefore your

final sensitivity. The lowering/understanding of the threshold becomes particularly important for lower mass dark matter models. In order to measure the threshold, defined as the energy at which a signal event has a 50 percent probability of triggering the detector, a multiple detector method was employed. This method takes advantage of the fact that when any detector in CDMS triggers, it results in the hardware taking a 'snapshot' of all detectors even ones that only record noise. After applying all the data quality cuts, taking particular care to filter out any cross-detector induced noise/events, you start by looking at all snapshots where the main trigger was not issued by the CDMSlite detector. Running the optimal filter across all the detectors results an energy/amplitude estimate for any energy deposited per event. One can then compare within an energy bin the number of events that would have issued a trigger in the CDMSlite detector verses all events that get reconstructed to energies higher than the noise wall on the CDMSlite detector. Once you have this list of events and their corresponding energies (E_i) that did and did not issue a trigger in the CDMSlite detector I initially developed an unbinned likelihood fit which fits the data to a linear combination of error functions:

$$\epsilon_{\pm} = 0.5A_1(1 + erf(\frac{E_i - \mu}{\sigma})) \tag{3.14}$$

where:

$+$ and $-$ correspond to trigger (signal) and non-trigger events respectively

A: amplitude parameter that generally reconstructs very close to 1

μ: 50 percent trigger threshold, note that this is kept the same for both the trigger/non-trigger events.

σ: Trigger width, note there there are some normalizations of σ that require an extra factor of $\sqrt{2}$, which I have absorbed into σ.

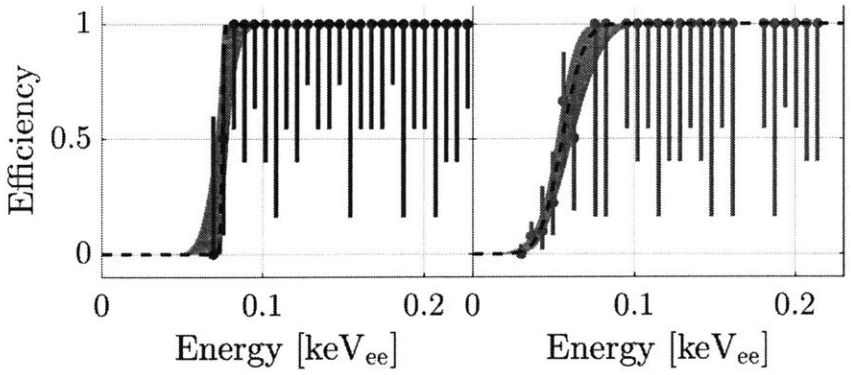

Figure 3-14: Final CDMSlite Trigger Efficiencies for Run 2 Period 1 (Purple) and Period 2 (Orange). The CDMSlite run was divided up into to separate periods as improvements in understanding low frequency noise from the cyrocoolers, allowing for a reduction of the hardware trigger level as discussed in the introduction to bolometers chapter. Taken from [55]

with the likelihood given by:

$$ln(\mathcal{L}(\mu,\sigma)) = \sum_{-} ln\ \epsilon_{-}\ (E_{-}|\mu,\sigma) + \sum_{+} ln\ \epsilon_{+}\ (E_{+}|\mu,\sigma) \tag{3.15}$$

The CDMSlite team then further refined this technique, by applying Markov Chain Monte Carlos (MCMC techniques are discussed in Appendix) to find the best fit values for μ and σ, resulting in the published analysis threshold of 75^{+4}_{-5} (period 1) and 56^{+6}_{-4} eV_{ee} (period 2) as shown in Figure 3-14

3.6 Moving Forward

As current generation direct detection experiments, such as CDMS/CDMSlite [55] or LUX [57] make room for the next generation of experiments (CDMS-SNOLAB [58] or LUX-Zeppelin [59]), dark matter direction detections stands at a crossroads - see Figure 3-15. Liquid noble element-based detectors, such as XENON or LUX/LZ have the advantage of scalability coupled with a heavier target (Xenon) material[8]. This comes at the cost of higher thresholds, which then limits their sensitivity range for lower mass dark matter searches. Cryogenic bolometer based experiments, such as

[8]and added bonuses such as self shielding in the inner detector volume

CDMS, generally use lighter targets (Germanium for example), which allows for lower thresholds and therefore probing of lower mass dark matter models. At higher dark matter masses the liquid noble elements detectors have shown their ability to probe deeper into new parameter space compare the SuperCDMS HT limit curve (consisting of all 15 CDMS detectors operating in their standard configuration) and the Xenon100 and LUX curves. CDMSlite has proven the ability to reach lower lower thresholds via Luke-Neganov amplification. Looking at the limit curves presented in Figure 3-15 the CDMSlite results are particularly impressive considering that the CDMSlite achieved their results through the use of only a single one of the 15 detectors deployed in CDMS. For future experiments this means that the field of direct detection has split into two regimes: searches for dark matter heavier than 10 GeV will require larger and larger scale liquid noble element detectors, while low mass searches will be lead with low threshold cyrogenic bolometer experiments taking advantage Luke-Neganov amplification.

Looking then beyond the next generation of experiments, direct detection experiments are rapidly approaching the so-called 'neutrino-floor', where their experiments have such a low threshold that they pick up the coherent recoil of neutrinos from the sun interacting with the atoms in your detector. This represents the point at which it becomes impossible to distinguish a rate excess in your detectors due to dark matter from statistical fluctuation in this neutrino background source, which can not be shielded against. While for dark matter searches the neutrino floor is an irreducible background, the processes behind the neutrino floor have become an active area of research due to the recent discovery by the COHERRENT collaboration [61] made possible by a low threshold detector setup.

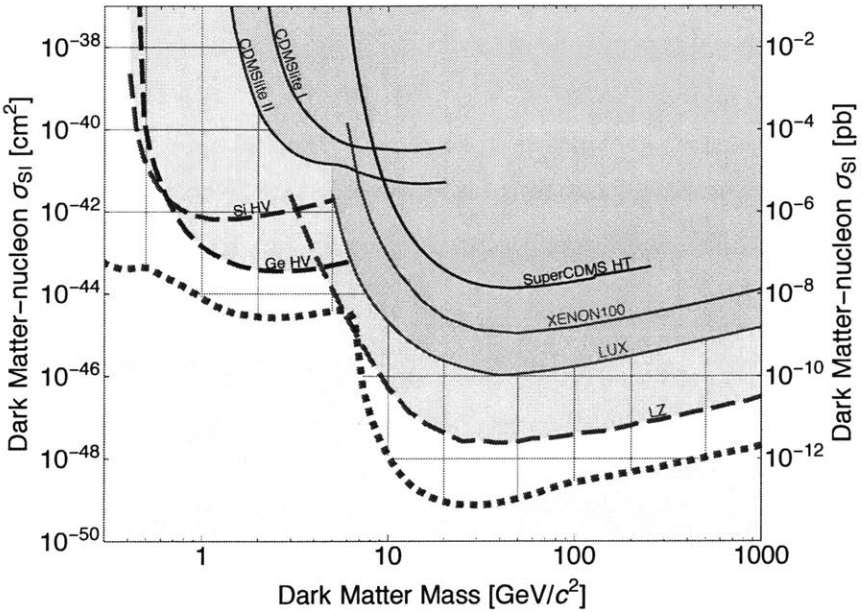

Figure 3-15: Summary plot for the current and next generation of dark matter direct detection experiments. Solid Lines indicate current limits, while dashed lines indicate projections for future. The orange dashed line indicates the neutrino-floor[60] for Xenon based experiments. The neutrino floor comes about from coherent neutrino interactions with nuclei resulting in a low energy recoil event, the detection of which is the main concern of the following section

Chapter 4

Coherrent Neutrino Scattering Background Measurements using Bolometers

"There are two possible outcomes: if the result confirms the hypothesis, then you've made a measurement. If the result is contrary to the hypothesis, then you've made a discovery"
— Enrico Fermi

4.1 Introduction to Coherent (neutral-current) Elastic Neutrino-Nucleus Scattering (CEνNS)

Coherent (neutral-current) Elastic Neutrino-Nucleus Scattering (CEνNS)[1] is a unique interaction between neutrinos and matter as it involves the combined interactions of multiple nucleons with a single neutrino, recently observed by the COHERENT collaboration [61]. The characterization of this interaction would open the door to physics probes beyond the Standard Model as well as providing some "real world" applications for neutrino physics. In recent years, this particular phenomenon has regained attention from dark matter direct detection searches as CEνNS will form

[1]There are many acronyms in literature for this phenomenon including simply Coherent Neutrino Scattering (CNS), but in this thesis we will refer to this as CEνNS, pronounced "sevens"

an irreducible background to all dark matter searches [60] as discussed in the previous section. To first order, this is a tree-level Standard Model process characterized by the following differential cross section [62]:

$$\frac{d\sigma}{dT} = \frac{G_F^2}{4\pi} Q_W^2 M_A \left(1 - \frac{M_A T}{2E_\nu^2}\right) F(q^2)^2 \tag{4.1}$$

where:

$Q_W = N - Z(1 - 4sin^2\theta_W)$ = Weak Charge and G_F^2 = Fermi Constant are well characterized parameters in weak scale physics. However; all the measurements of these parameters occur with reactions which have much higher Q values, opening up the possibility of measuring these parameters in a new energy range

$F(q^2)$ = Nuclear form factor at a specific momentum transfer q, the uncertainty in these calculations dominates the overall uncertainty of $\sigma_{CE\nu NS}$ ($\approx$ 5 percent)

M_A = Atomic Mass and E_ν = Incoming Neutrino Energy

T = Recoil Energy and which is proportional to E_ν, unlike other neutrino neutral current interactions.

This equation alone reveals a several of the interesting properties of CEνNS. The squared dependence on the total number of nucleons in the weak charge factor is what allows the nucleus to behave as one, thus the 'coherent' part of the phenomena. At the same time though in order to maintain coherence there is the additional requirement on the incoming neutrino, namely that its' wavelength must be on the order of the same size as the nucleus it is interacting with. This is what limits the energies of the neutrinos that can be used to study this process. If the incoming neutrinos are too high in energy they will only interact with single nucleon instead of coherently with the entire nucleus. It is this coherence that drives up the overall cross section (read interaction probability) to 10^{-39} cm^2, much higher than most other neutrino processes, resulting in a high event rate. However; the main problem encountered by any experiment attempting to measure CEνNS is that the energy

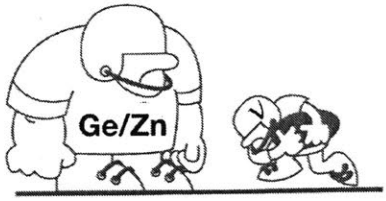

Figure 4-1: Cartoon representation of a typical neutrino-nucleon interaction. The mass differences between the neutrino (mass $\lesssim$ 0.2 eV) and its target (50+ GeV), is what results in the tiny recoils observed in Ricochet

transfer per reaction is extremely small, on the order of keV or less - see 4-1. In fact, in the original paper by Friedman [62], he states that attempting to measure this process is an "...act of hubris, because the inevitable constraints of interaction rate, resolution, and background pose grave experimental difficulties for elastic neutrino-nucleus scattering".

4.1.1 Applications of CEνNS within and outside of Particle Physics

CEνNS has a wide variety of applications both within and outside the world of particle physics and with the recent discovery by COHERENT [61], we have opened up the door to future probes of these applications:

- Supernova physics: CEνNS plays a critical role in the time evolution of type II supernovae and has an strong impact on the resulting neutrino spectrum measured with ground-based neutrino detectors. In the extreme environments [2] inside the core of collapsing supernovae processes such as CEνNSbegin to dominate the interactions between nucleons and neutrinos [63] as over 99 percent of the total energy contained in the explosion gets carried away by neutrinos. One of the problems facing supernova modeling stems from the fact current models do not consistently bring the supernova explosion to fruition [64],[65]. Only through the inclusion CEνNS and other nuclear/neutrinos processes beyond

[2]Just showcase the extreme environment in these supernovae, the density often reaches $10^{12} g/cm^3 \implies$ mean free path of 0.5 km for neutrinos

the scope of this thesis provide the extra energy needed to induce supernovae to actually explode in simulations [66]. Terrestrial measurements of this neutrino spectrum from supernovae would be hampered by the low expected event rate of 7 events in a 10 second window in a 1 ton Argon detector with a 5 keV threshold [67] from a supernova 10 kpc distant. Additional solar measurements [68] are possible.

- Beyond the Standard Model Interactions: Now that CEνNShas been observed for the first time, we have yet to see if the true differential cross section actually obeys equation 4.1. Any deviation from this tree-level rate would point to the need for additional terms in the Standard Model Lagrangian, loosely grouped together as Non-Standard Interactions (NSI) or Beyond the Standard Model (BSM) theories [69] [70]. The measurement of these additional terms could help explain the origin of the neutrino mass [71] (discussed more in detail in Chapter 5) and/or set limits on supersymmetric models [72]. Additionally, any measurement with less than 10 percent uncertainty in the event rate could also provide competitive limits on neutrino magnetic moments [73] as well as a host of additional BSM models [74].

- Nuclear Probes at Low Energies: The factor of Q_W^2 (in particular $sin^2\theta_W$) in equation 4.1 has not been well characterized at low energies. There are hints from the NuTeV experiment [75], that the value of Q_W^2 could start to diverge from the standard model value at Q = 4 GeV, opening the requirement for additional measurements at even lower Q values. CEνNS Cross section measurements as a function of energy on multiple nuclear targets would also allow for a better understanding of the neutron structure functions inside the nucleus reflected in reducing the uncertainty in the nuclear form factor measurements (F(q) in equation 4.1) [76].

- Nuclear non-proliferation applications: Nuclear non-proliferation efforts have gained a lot of attention in recent years, especially after the fall of the Soviet Union. One of the main issues facing non-proliferation efforts come in the

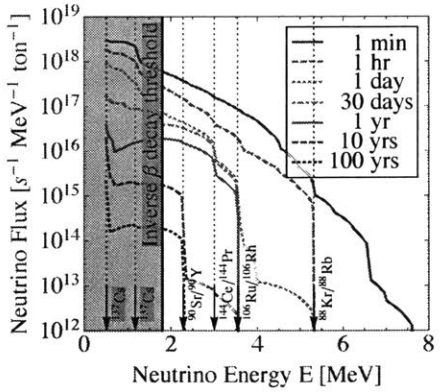

Figure 4-2: The energy spectrum of antineutrinos emitted by spent nuclear fuel as a function of the time the gray bar indicates the area below which inverse-beta decay searches, the dominant neutrino-detection process, are no longer are applicable. From [77]

form of monitoring for compliance to assurethat agreements are being correctly followed. In this vein, CEνNScould provide us with the first direct physics application of neutrino physics. Neutrinos offer us the ability to probe reactions occurring in the inside of nuclear reactors, in a manner than can not be shielded against. If you can create a reliable CEνNS detection system, one then has the ability to monitor spent fuel storage sites [77] or even the ratios of various elements inside heavy water reactors [78], based on the premise that flux and energy spectrum of neutrinos (and/or anti-neutrinos) will change based on the specific ratios of various decaying isotopes as shown in 4-2.

4.1.2 Ricochet Proposal

The recent discovery of CEνNS by the COHERENT collaboration [61] has proven the feasibility of detecting CEνNS, now opening the door to the characterization of CEνNS. Several proposed experiments, including Ricochet [79, 80], seek to take advantage of the low-threshold and high-mass detectors already deployed for dark matter direct detection experiments and discussed in the previous chapters. The Ricochet proposal seeks to utilize a superconducting Zn and/or CDMS-style Ge detector with a target threshold of 100 eV and 1 kg deployed payload. Zinc superconduct-

ing detectors, the subject of ongoing research and development, offer the possibility of intrinsic background rejection due to the difference in quasi-particle interaction dynamics between nuclear and electron recoils [36]. Regardless of the detector material/readout mechanism, all these proposals require a high-intensity high-energy neutrino source, for Ricochet this meant running the detectors near a nuclear reactor. We first explored the possibility of deploying the Ricochet experiment at 7 meters from the 5.5 MW MIT (research) Reactor (MITR) with an expected core neutrino flux of 2.2×10^{18} ν/second corresponding to a CEνNS signal event rate of approximately 1 events/kg/day with Zn detectors. The proximity to the reactor core comes at the cost of an additional intrinsic background in the form of neutrons, which could mimic a CEνNS signal in Ge/Zn detectors. High-energy reactor neutrons (above 1 MeV) in particular make it through the concrete shielding surrounding the reactor core and can then interact with our detectors.

4.1.3 Ricochet Backgrounds

These high energy neutrons create the need for additional polyethylene shielding around the detector to absorb this high-energy neutron background. This underscores the need for accurate information on both the shape and overall normalization of the neutron energy spectrum over a wide range of energies. In order to achieve this neutron monitoring, we deployed a $^3_2$He detector that had previously been used to monitor neutrons produced in neutral-current reactions at the Sudbury Neutrino Observatory (SNO) together with incrementally thicker PVC layers in a Bonner cylinder approach. The $^3_2$He detector as shown in Figure 4-3, has a high neutron sensitivity at thermal neutron energies, but this drops off quickly at higher neutron energies [81]. Akin to a Bonner sphere, by increasing the amount of shielding around the detector one samples progressively higher energy components of the incoming neutron spectrum, which have been thermalized to the sensitive region of the $^3_2$He detector. For each NCD shielding configuration, we then record energy deposited in the $^3_2$He detector as well as the rise time of each pulse for use as a pulse-shape discriminator (discussed in Section 2).

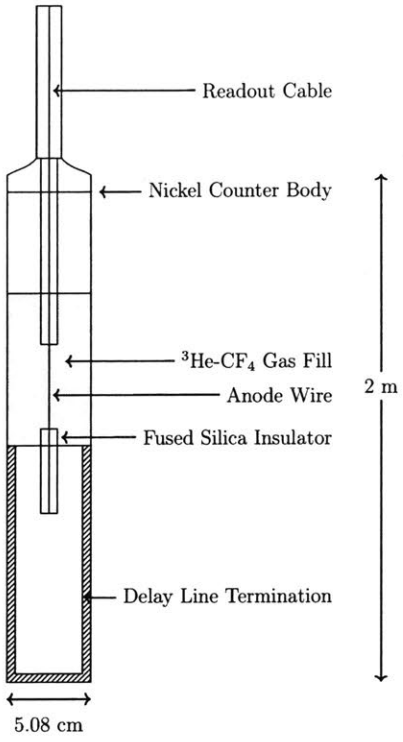

Figure 4-3: Labeled schematic of the NCD detectors taken from [82]

After collecting the event rates from the various shielding configurations, we then unfold both the neutron spectral shape and the normalization. This is achieved by creating a series of transfer functions for each shielding configuration in Geant4 by simulating the detector response to various mono-energetic neutron sources. This suite of transfer functions is then used to calculate the likelihood of various binned neutron spectral shapes, which allows us to then optimize the spectral shape and normalization that maximizes the likelihood. For calibration and as a cross-check of our unfolding procedure we also deployed a $^{252}_{98}$Cf source at the MITR site. Finally, we ran additional Geant4 simulations, using our calculated neutron spectrum as an input, which sought to measure the possibility of reducing the overall neutron background to a level below the expected CEνNS signal rate.

4.2 Experimental Setup

4.2.1 The Neutral Current Detectors - SNO Lab background

In 1998, the "solar neutrino problem" represented one of the biggest open questions with regards to neutrino physics. The neutrino flux coming from the sun was measured to be only a third of what all the solar neutrino production models were predicting. The SNO experiment [83] located 2070 meters below ground at the INCO Creighton nickel mine near Sudberry, Ontario was a tank of 1000 tonnes of 99.92% pure heavy water (D_2O). This 1000 tonne water heavy water was designed to measure

the neutrino flux coming from the sun via the following four particle interactions:

$$d + \nu_e \rightarrow \mathrm{p} + \mathrm{p} + \mathrm{e}^- + 1.44 \text{ MeV} \tag{4.2}$$

$$d + \nu_x \rightarrow \mathrm{p} + \mathrm{n} + \mathrm{e}^- + 2.22 \text{ MeV} \tag{4.3}$$

$$d + \bar{\nu_e} \rightarrow \mathrm{n} + \mathrm{n} + \mathrm{e}^- + 4.03 \text{ MeV} \tag{4.4}$$

$$e + \nu_e \rightarrow e + \nu_e \tag{4.5}$$

The first interaction, called the charge current reaction, could only happen with electron neutrinos. The second interaction, called the neutral current reaction, provided a channel to measure the total neutrino flux coming from the sun as it was insensitive to the specific flavor of neutrino. As at the time one of the biggest unknowns about the solar neutrino problem dealt with determining the exact composition of the neutrino "beam" coming from the sun. By tagging the neutral and charged currents event in your experiment one could measure the overall solar neutrino flux and determine the composition of the incoming neutrinos at the same time. The crux of the matter was tagging the neutral current events, in particular the neutrons. Neutrons have a notoriously long lifetime in particle physics and can be produced via a wide variety of other processes, for example the photo-disintegration of Deuterium via 2.2 MeV gammas. Once the neutron was produced in an signal event one needed to tag and preferably capture the neutron as their long lifetime ($\approx$ 10 minutes) can mean they linger as a background in your detector for some time. The ideal detector for this came in the form of Neutral [3]) Current Detectors (NCD). [84] The NCD detector consists of one 2-meter-long cylinder filled with a 85:15 percent mixture of $^3_2$He and CF_4[4] with a collection anode wire running coaxially through the gas. 112 of these NCDs were lowered into the SNO experiment to collect all the background neutrons. The exact design specifications of the NCDs were heavily constrained by the requirements of operating inside the SNO experiment, for example all the materials used in

[3]or Neutron in some circles

[4]CF_4 operates as a quenching gas which stabilizes the avalanche process that occurs when the induced charge gets to within tens of microns of the anode collection wire

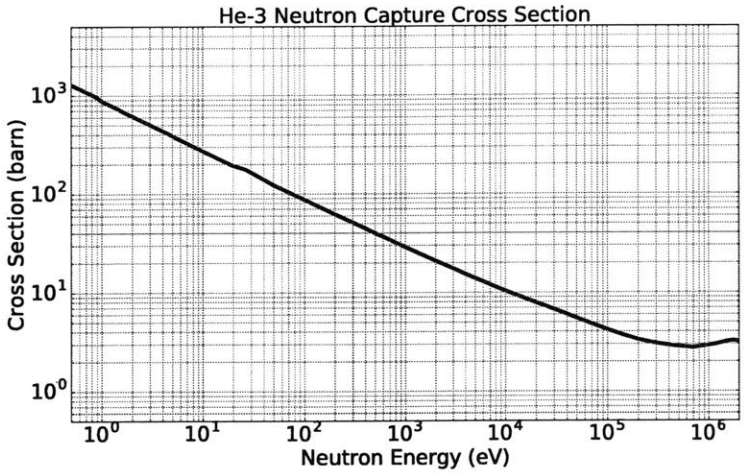

Figure 4-4: $^3_2$He Neutron capture cross section in as a function of energy. It is important to note that the strong energy dependence of the cross section on energy. Data taken from [85]

the construction of these NCDs had to pass rigorous background test to ensure they themselves would not constitute an additional background in the SNO experiment. For our purposes, the main design considerations we worried about were the internal pressure of the He-3 as well as the overall $^3_2$He to quenching gas ratio, both of which are parameters in the simulation discussed later. These both had been set by the SNO collaboration years prior to optimize the capture of neutrons. Even at normal room temperature and pressures the $^3_2$He gas has an incredibly high cross section of about 1000 barns at thermal neutron energies - see section 4-4. When we discuss neutron energies we often discuss them in terms of temperatures or their thermal speeds. Throughout this thesis, the two most dominant neutron populations that we will discuss are 'slow/thermal' neutrons with energies around 1 eV and 'fast' neutrons with energies around 1 MeV. In between slow and fast neutrons there are numerous other subdivisions with different names and definitions depending on who you ask, but for this thesis we will stick with these two populations and their definitions. The NCD detectors, while their sensitivity is strongly peaked for the thermal neutrons 4-4, the cross section for fast neutrons remains high enough for efficient pickup. However; as we will later see the much higher slow neutron flux will dominate the overall event

rate measured in the NCDs.

Incoming neutrons interact with the $^3_2$He via the following process:

$$\mathrm{n} + {}^3_2\mathrm{He} \rightarrow \mathrm{p} + {}^3_1\mathrm{H} + 764\ \mathrm{keV} \tag{4.6}$$

The proton and the triton share the 764 $\mathrm{keV}_{kinetic}$ between themselves and then ionize the $^3_2$He/CF_4 gas mixture as they lose energy passing through the cylinder. While the ions get collected on the outer grounded shell of the NCD, the resulting induced charge is collected on the anode wire. We performed a series of SRIM simulations [86] to determine the proton and triton track length in the $^3_2$He, determining an average track length of 7.5 and 2.5 mm respectively [87]. We tested 6 different shielding configurations corresponding to an overall shielding thickness that ranged from 0 up to 7.23 cm radially. For each of the 6 shielding configurations we collected data with the reactor on/off and with a $^{252}_{98}$Cf neutron calibration source. Finally, the detectors were biased at 1650 V, which represented the highest gain we could use before screening effects from space charge degraded the NCD energy resolution [5].

4.2.2 The Neutral Current Detectors - Event Topology and Selection

When an event interacts with the NCDs and ionizes the $^3_2$He/ CF_4 mixture, the dE/dx/track orientation determines the event time length, while the overall event amplitude is determined by the total energy of the proton/triton pair collected by the anode wire.

From each event trace, two variables were estimated: the rise time[6] and the event amplitude. From these data, we could then produce a "trapezoid plot" (as seen in Figure 4-5) with two clear populations of events visible: with fast, high-energy events defining neutron captures and generally slower lower energy background events. The main source of background events for the NCDs stem from Compton scattered

[5]Measured to be 44 keV (FWHM) at 764 keV

[6]We defined the rise time as the time it takes for the event trace to go from 10 to 70 percent of the maximum amplitude

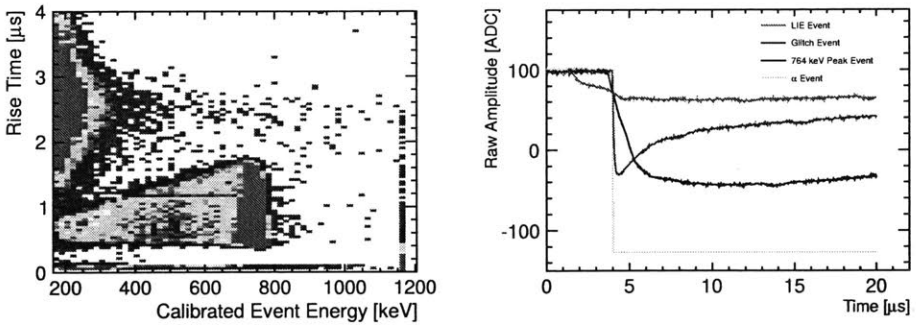

Figure 4-5: The trapezoid plot (a) showcasing the four event populations present and their relative densities in our detector setup, along with four example events (b) taken from each of the event populations discussed in the text below. For a full discussion about the underlying reason for the various event topologies see text below

light particles such as electrons and muons with longer rise times coupled with lower event amplitudes allowing for their classification as Low-Ionizing Events (LIE). We also observed two additional background signal populations with extremely short rise times, corresponding to micro-discharges/glitch events and events that saturated the DAQ system at 1.2 MeV corresponding to α deposition events. For a given energy of event, one can also note the range of rise times which stems from the particular orientation of the event track, with perfectly parallel events resulting in very short rise times and perpendicular events having the longest rise times. Lower energy neutron events produce a smaller range of rise times because of incomplete event collection due to the walls of the NCDs. The NCDs were calibrated by using a three-point calibration fitting scheme using the 191 keV, 564 keV and 764 keV event peaks/shoulders which correspond to: full energy of just the proton collected, full energy of just triton collected and full reconstruction of the entire event-with both proton and triton induced ionization collected on anode wire respectively. The event-selection criteria were defined by a trapezoidal region defined by a series of four linear boundaries as shown in Figure 4-6 in this rise-time/energy-deposition space. The four linear boundaries were defined by looking at the data collected using the maximum PVC thickness as these data had the clearest separation between LIE and neutron events due to the thick shielding around the NCDs.

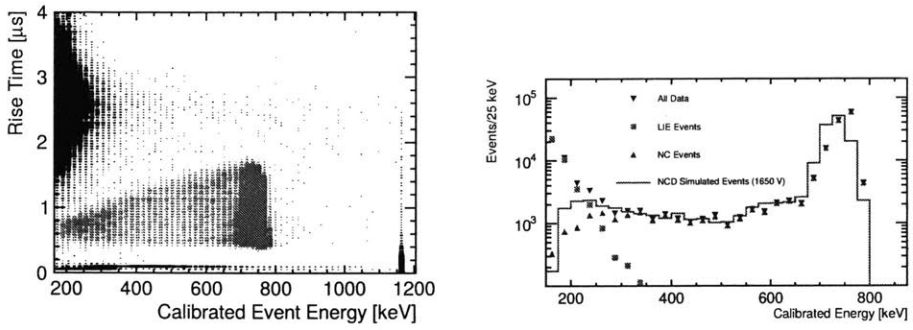

Figure 4-6: Rise-time versus Energy plot taken from a typical NCD run. Red events indicate those events that passed the data quality cuts that identify these events as neutron induced (NR) events, while all black events represent background LIE/Glitch/α events. Calibrated spectrum of events in the neutron capture region. The 764 peaks together with the 564 and 191 keV shoulders were fitted to calibrate the NCD response. The 764 keV peak was fitted using an Exponentially Modified Gaussian (EMG) [88], while the 564 and 191 keV shoulders were fitted with error functions. Note that the error bars on the NR/LIE spectrum may be too small to see NCD nuclear capture event criteria and calibrated NCD spectra (after selecting nuclear capture events) as well as a simulated NCD spectrum. In both plots one can see the 764, 573 and 191 keV features that are the hallmarks of NCD NR events

The gain and shape of the trapezoid region was stable from run to run and over the course of 24+ hour long runs, which justified our use of the same selection criteria for all the data sets collected. The rounded edge of the nuclear recoil band at 764 keV visible on Figure 4-6 was due to space charge screening effects, which were simulated in GEANT4 using the framework established by [89]. At lower anode voltages, space charge effects are minimized as evidenced by the sharp cutoff in the NCD spectrum at 764 keV visible in Figure 4-6 while at lower event energies the space charge effect is even lower. Reasonable agreement was achieved between the simulated and the collected NCD spectrum even at higher anode voltages. Space charge effects were determined to only have a negligible effect on the systematics on the overall event rates extracted from the NCDs due to the excellent signal/background ratio at 764 keV. In order to calculate the event rate accounting for dead time and small changes in the event rate over time, the time between events was measured and fit to an exponential distribution. From Figure 4-7, one can see that the data is well-described by an

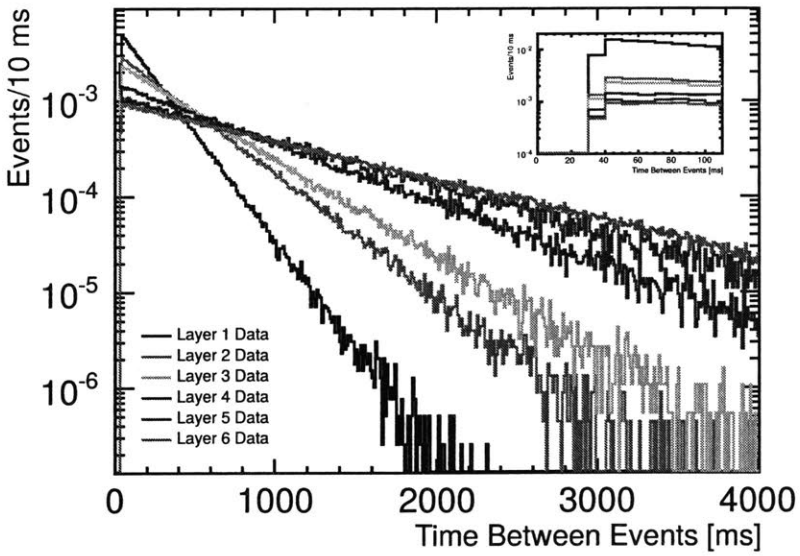

Figure 4-7: Time between subsequent nuclear recoil events for all the shielding configurations we ran, normalized to 1. One can clearly see the monotonic decrease in event rate as a function of layers, consistent with a strong thermal component to the neutron spectrum. **Inset**: Same plot focusing on the short time between events to highlight the 30 ms dead time in our detector setup

exponential distribution and that the detectors had a dead time of approximately 30 ms. These extracted event rates were then fed into the deconvolution procedure outlined below. Background NCD rate measurements, which included cosmic-ray induced neutrons, with the reactor off were subtracted from the reactor on NCD data. In order to determine the effective cosmic ray overburden at the MITR for a possible future Ricochet deployment, we collected cosmic ray background data using desktop muon counters [90] during a 24 hour period where the reactor was turned off and determined the effective overburden to be 1.5 m.w.e.

4.3 MITR site

The MIT (research) Reactor (MITR) is a nuclear reactor that has been in operation since 1958 - see Figure 4-8, when it first achieved criticality. While the overall power

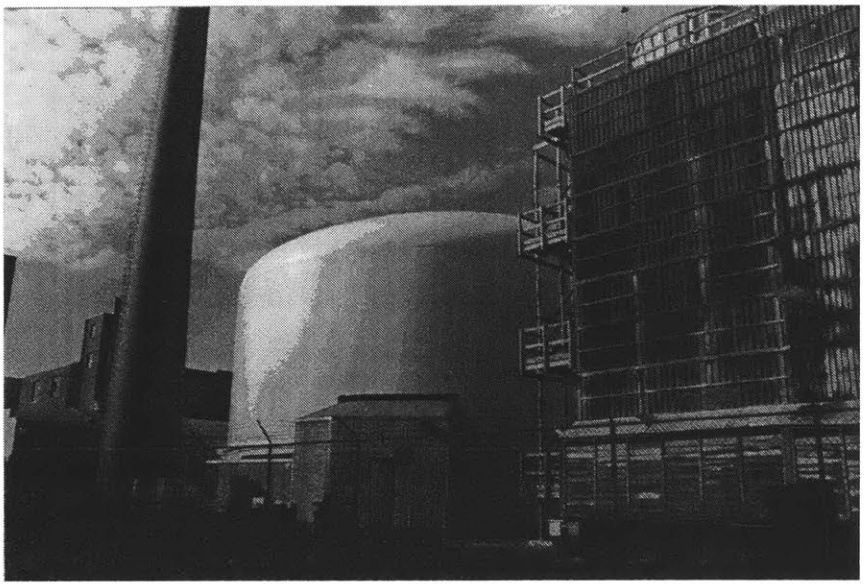

Figure 4-8: Photo of the MITR complex taken from the railroad tracks along Mass Ave. The actual reactor components are located inside the light blue tank shown in the middle. The entire complex is designed to look as unassuming as possible

output at the MITR (5.5 MW[7]) is modest, the site has various advantages compared to power stations. For example, the MITR facility was used to exposure the NTD chips that would eventually be used as readouts [91] for the CUORE experiment discussed in Section 2.4.2. For the Ricochet experiment, the MITR site offered the ability to get very close to the actual reactor core, thus reducing the $\frac{1}{r^2}$ effect that would reduce the neutrino flux seen by the Ricochet detectors. The room where we performed out measurements which was proposed for the Ricochet setup was located only 7 meters away from the reactor core, even closer than the Cowen and Reines experiment. This short baseline distance also had the added benefit of providing the ability to probe various active to sterile neutrino models as discussed in [92].

4.4 MITR Flux Reconstruction Procedure

Given measurements of the reactor neutron rate with various numbers of PVC layers surrounding the detector, we are interested in recovering both the shape and normal-

[7]Compared to the 5.5 GW more typically found in power generating stations such as Double Chooz discussed later

ization of the neutron spectrum which requires unfolding techniques. Although there are various approaches advocated in the literature, nearly all require the calculation of a *transfer function* $T^j(E_i)$, which relates the incident neutron flux ϕ to the event rate R measured by the NCD. In our case, for each shielding configuration j, we require a transfer function, T^j, defined over the same interval as the binned energy spectrum E_i, in order to estimate the theoretical event rate:

$$R^j_{theory} \simeq \sum_i^{N_{bins}} \int_{E_i}^{E_{i+1}} \phi(E_i) T^j(E,n)\, dE. \tag{4.7}$$

We assume that the neutron flux is flat in lethargy space, [8] while showing an inverse energy dependence in energy space throughout a bin. The transfer functions were calculated over a neutron energy range encompassing thermal neutrons up to high energy reactor neutrons. The high-energy cutoff (10 MeV) for the reconstruction bins was selected because less than 1 percent of the emitted neutrons have energies greater than 10 MeV for a thermal reactor core spectrum centered at 1.4 MeV. We then use maximum likelihood to fit the neutron energy spectrum in energy bins to the observed rates for each shielding configuration as discussed further in Section 4.

We estimate the transfer function of the detector and shielding setups using a Monte Carlo simulation based on Geant4 10.00.p02 [83]. To simulate the hadronic physics, including neutron interactions, we use a modular physics list including the QGSP_BERT_HP model containing the "high-precision" neutron physics simulation that uses version 4.4 of the G4NDL data. In addition, our physics list incorporates the "G4ScreenedNuclearRecoil" process that models screened electromagnetic nuclear elastic scattering and is important for accurately simulating the propagation of the proton and triton after a neutron capture on ^{3}He [93]. Unlike the default models in the QGSP_BERT_HP physics list, the G4ScreenedNuclearRecoil processes give physically realistic results for ion track lengths and energy loss in the detector gas,

[8] Lethargy is the logarithmic ratio of energy before/after a collision, given by the relation

$$u = ln(\frac{E_0}{E}) \tag{4.8}$$

which were also found to be in reasonable agreement with results from the widely-used SRIM software [86].

The simulation includes the layers of PVC shielding as described in the section 4.2, correctly accounting for the geometry of the PVC pipes when resting on the ground. Although it is not needed for the transfer function analysis, the simulation also implements models of the charge propagation, space-charge effects, and the preamplifier electronics, similar to [87]. To simulate the transfer functions needed for the unfolding analysis, we simulate 10 million monoenergetic neutrons with each of the 6 shielding configurations and at 34 logarithmically-spaced energies between 10^{-8} MeV and 10^{2} MeV. The neutrons in the simulation are generated on a cylindrical surface immediately surrounding the outermost layer of shielding, with a direction that is chosen isotropically from the surface of the shielding directed inward toward the detector. We have also determined that bias in our calculations due to non-concentric compared to perfectly concentric alignment of the various shells is small due to the approximate radial symmetry of the NCD setup. Another effect of this radial symmetry is that the NCD setup is insensitive to the initial direction of the reactor background neutrons. In addition, the data collected by the NCDs pointed to a strong thermalized component 4-7 to our neutron spectrum at the MITR, which supports the assumption that our neutron flux will be close to isotropic.

Figure 4-9 shows the transfer functions for each layer of shielding as a function of energy. From these plots one can note a few important features, namely that we only gain significant sensitivity for fast 'core' neutrons with 5 or 6 layers of shielding. In addition, we note a significant degeneracy between the transfer functions for each shielding configuration, which limits the sensitivity of the unfolding analysis, which motivated the idea of using a MCMC analysis as discussed below.

4.4.1 Likelihood/MCMC Analysis

Using the transfer functions (see Figure 4-9) calculated from the Geant4 simulations in the previous section, we can calculate an expected theoretical event rate for each shielding configuration, given a binned neutron spectrum shape. By minimizing the

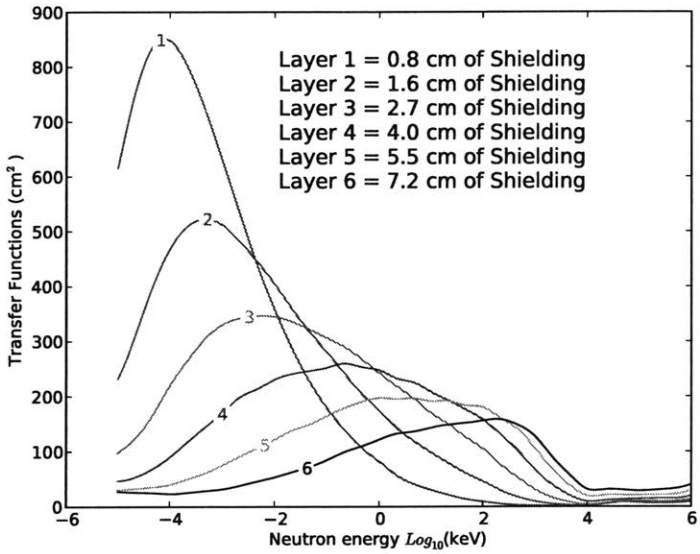

Figure 4-9: Transfer functions for each shielding configuration as a function of incident simulated monoenergetic neutron energy - the large degree of overlap between these transfer functions prompted our use of an MCMC to deconvolve the data. The transfer functions are normalized to the surface area of the shielding configuration used to calculate them.

difference between the theoretical and observed event rates we can then extract a binned neutron spectrum. Due to the high correlation observed between the bins (see Figure 4-10) and to ensure that the best fit χ^2_{fit} that we found truly represents a global best fit we use the maximum entropy method.

First, we define a likelihood $\mathcal{L}$ function for the theoretical event rates for a given binned spectrum (ϕ_i) via the following relations:

$$\chi^2_{fit} = \sum_{i=1}^{n} \frac{(R_i^{obs} - R_i^{theory}[\phi(\vec{E})])^2}{\sigma_i^2} \tag{4.9}$$

$$S = -\sum_{i=1}^{m} p_i \log(p_i) \quad \text{with} \quad p_i = \frac{\phi_i(E)}{\sum_i \phi_i(E)} \tag{4.10}$$

$$\mathcal{L}_\phi = \exp\left(-\frac{\chi^2_{fit}}{2} + \frac{S}{2w}\right) \tag{4.11}$$

where i corresponds to the particular NCD shielding configuration and S corresponds to the entropy. In this context, S represents another quantity that needs to be simultaneously minimized by maximizing the likelihood function. In Equation 4.11, w corresponds to a regulation parameter which determines if our extracted spectrum is prior- (small w) or data-dominated (large w). In this context, a prior-dominated deconvolution would result in essential features smoothed out of the unfolded spectrum as the unfolding algorithm would converge to the prior [9]. On the other hand, a data-dominated unfolding can result in large unphysical fluctuations in the resulting unfolded spectrum. We wish to find a value for w such that we minimize the resulting χ^2_{fit} and such that small changes in the χ^2_{fit} only result in minimal changes in S. In practice, this means finding the point on the $\chi - S$ curve (see Figure 4-11) with the largest curvature. It should be noted that this prescription only gives us an order-of-magnitude estimate for the best value for w. By varying the regularization parameter along this curve we were also able to calculate the systematic error due to this method, which is included in the quoted systematic error in Table 4.1

We assume Poisson fluctuations in the measured values of the R_i^{obs}, which allows

[9] In this analysis, our prior is the result of the Minuit fitting (maximum entropy) plus our choice of regularization parameter

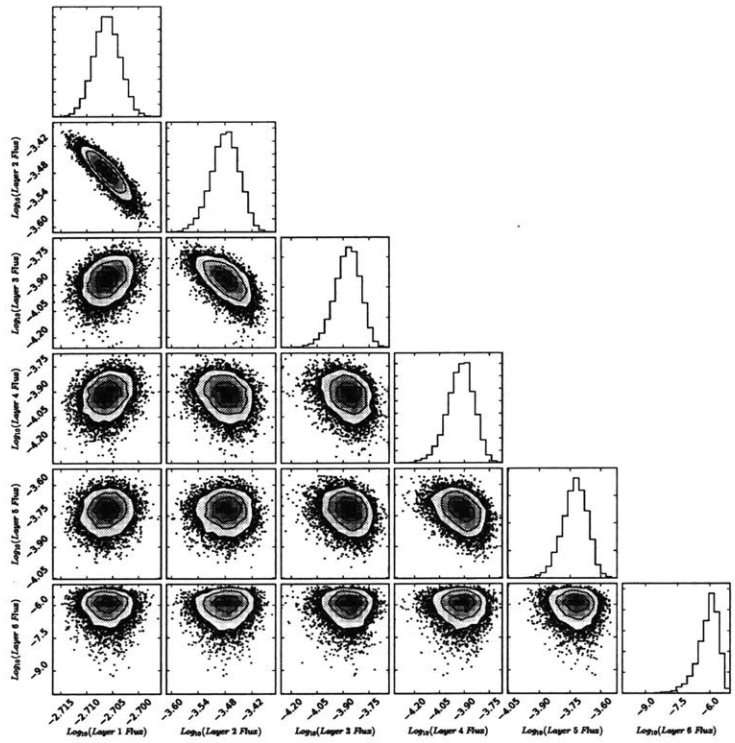

Figure 4-10: Correlation plots for accepted 6-bin MCMC points. Note that the values of each of the MCMC points are shown on a log scale here and in particular bins 1 and 2 have strongest correlations to the other, consistent with the large overlap in the transfer functions

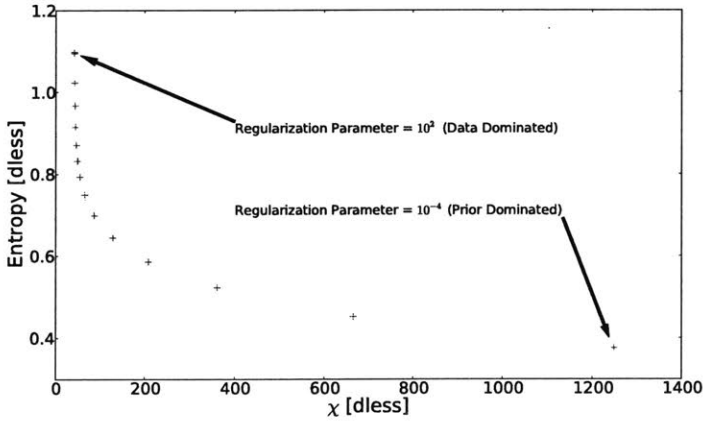

Figure 4-11: χ-Entropy Plot used to calculate the optimal value of the regularization parameter. The optimal value for the regularization parameter was determined to be 10^{-3} by examining the point with the largest curvature. The regularization parameter controls whether the fitting procedure we are using is data or prior dominated.

us to approximate the likelihood as a multivariate Gaussian. We also assume that the neutron flux follows an exponential spectral shape within a bin (flat in lethargy space). By finding the binned spectral shape that minimizes $\mathcal{L}$ via Minuit [94], we generate a preliminary binned neutron spectrum; however, due to the high degree of overlap between the various transfer functions this results in highly-correlated spectral neutron bins, and additional minimization is needed to find a global best fit. In order to better characterize this strong correlation between neutron bins and determine the distribution of expected neutron background events at the MITR, we employed a Markov Chain Monte Carlo (MCMC) analysis based on the framework described in Billard et al. [95].

4.5 MITR Data Collection and Analysis

4.5.1 Measurements undertaken at the MITR

Over the course of May-October 2015, we undertook three sets of measurements at the MITR reactor corresponding to the reactor on/off together with a $^{252}_{98}$Cf calibration neutron source. Using the unfolding techniques discussed above we were able to generate the following neutron spectra - see Figure 4-12. In particular, for the $^{252}_{98}$Cf calibration data we noticed the peak position shifted downward in energy, which we attribute to thermalization of the neutrons coming from the source. It is also important to note that strong thermal component inherent in all the unfolded spectra. This suggests that the surrounding concrete/shielding converts the raw neutron flux into an isotropic neutron gas; however, for all spectra there still exists a strong high energy ($>$ 1 MeV) component to the neutron spectrum, and is it these high energy neutrons that then will contribute the most to any neutron background for a possible Ricochet deployment at the MITR.

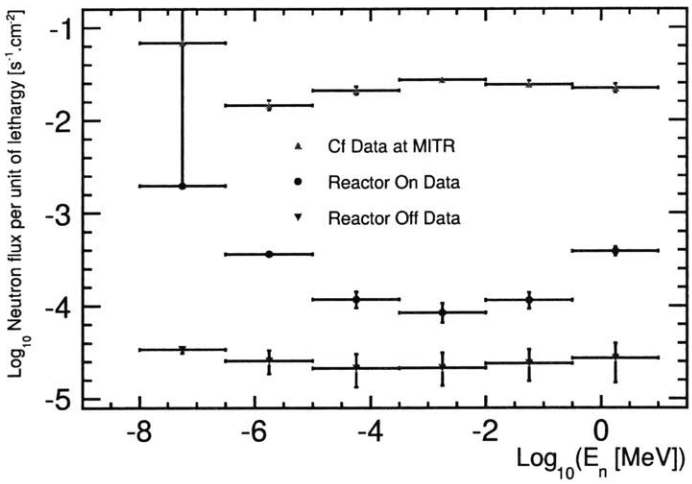

Figure 4-12: De-convolved spectra using the NCD data collected with reactor on, off and with a $^{252}_{98}$Cf neutron source deployed at the MITR. The vertical error bars here correspond to the a $\pm$ 1 σ confidence interval based on the MCMC simulations of the reconstructed flux

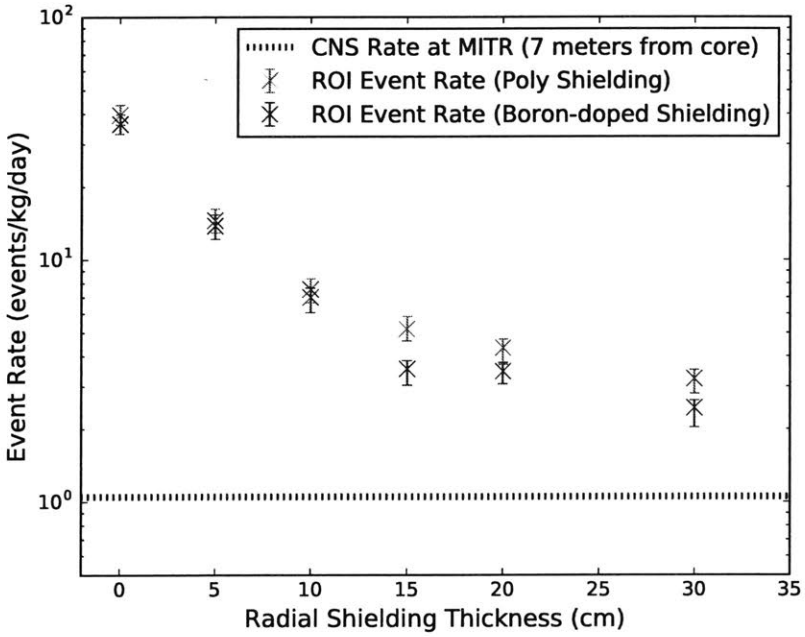

Figure 4-13: Event rate in the Region of Interest (between 0.1 and 1 keV) as a function of various thicknesses of Poly shielding (Normal and Boron-doped) around the sensitive detector region. Note: the error bars on this plot only correspond to statistical errors

4.5.2 Neutron Event Rate for Ricochet Deployment

As discussed in [96], Zn superconducting detectors offer the ability to distinguish between nuclear and electromagnetic recoils due to the differences in quasi-particle propagation inside the crystal lattice. Throughout these calculations, we foresee deploying a 1 kg Zn detector with a 100 eV threshold, which represents an achievable target threshold set by the EDELWEISS experiment [97]. Based on the calculations in [29], we determine the expected CEνNS event rate in Zn at the MITR facility to be approximately 1 events/kg/day at 7 meters from the core. Using the spectra extracted from the NCD data we performed another series of Geant4 simulations with a 1 kg Zn payload deployed in a Adiabatic Demagnetization Refrigerator (ADR)[10] configuration. We simulate neutrons isotropically at a radius of 64 cm from the center of the ADR, drawing from an exponential distribution in energy space across each of the bins used in the MCMC deconvolution. These primary events are then passed through a Geant4 model of the ADR setup to record the energy depositions of any neutrons. By then examining the number of events that fall in the Region of Interest (ROI) between 100 eV_{NR} and 1 keV_{NR} we then weigh each event by its corresponding flux value from the MCMC fit to then then extract an expected neutron background event rate. The high neutron background event rate with no shielding highlights the need to include shielding around our detector setup for any deployment at the MITR. This prompted us to perform an additional simulation surrounding the ADR with 30 cm, both radially and on the top/bottom, of bare and boron-doped (5 % by mass) polythene shielding to determine the feasibility of reducing the neutron background rate to the level of the expected CEνNS event rate. Systematic errors for this shielding simulation were calculated by comparing the neutron stopping power for 0 to 30 cm of poly shielding between 400 keV and 10 MeV to the reduction in flux as seen in [98]. Our systematic error points to our calculated event rate being closer to an upper limit on the actual neutron event rate that we could expect at for a

[10]In the early proposals the Ricochet detectors would also be used to study solar neutrinos, which would require pointing the crystals (and therefore the entire cryogenic system) towards the sun as it tracked across the sky. As the payload increased ADRs no longer provided the amount of cooling power thus necessitating a full dilution refrigerator

Ricochet deployment. With 30 cm of polyethylene shielding around the detector our calculated background neutron event rate becomes comparable to the CEνNSevent rate with our measurements indicating that the actual neutron background event rate will be lower. By taking advantage of MITR duty cycle, coupled with knowing the precise power levels over the course of 1 to 5 years, we have shown it is still possible to extract a CEνNSdiscovery signal even when the signal to background ratio is as high as 1:5 (see Table 3 in [96]). With additional shielding, our neutron background rate could be brought down still more, improving our CEνNSsensitivity further.

Rates (per kg per day)	CEνNSRate	MITR On	MITR Off	Cf
0 cm poly shielding	1.0	$36.3^{+3.2(stat)+6.8(sys)}_{-3.5(stat)-26.0(sys)}$	$5.0^{+1.3}_{-1.7}$	$(4.5^{+.2}_{-.3}) \times 10^3$
30 cm poly shielding	1.0	$3.2^{+0.4(stat)+0.5(sys)}_{-0.3(stat)-2.1(sys)}$	—	—
30 cm borated shielding	1.0	$2.4^{+0.4(stat)+0.4(sys)}_{-0.2(stat)-1.3(sys)}$	—	—
90 % CL (0 cm borated shielding)	1.0	< 41	< 7	$< 5 \times 10^3$
90 % CL (30 cm borated shielding)	1.0	< 2.9	—	—
90 % CL (30 cm bare poly shielding)	1.0	< 3.8	—	—

Table 4.1: Summary of the neutron background rate expected by a Ricochet deployment at the MITR for the three experimental configurations discussed in this thesis. All borated tests conducted with 5% (by mass) boron-doped poly shielding

4.6 Alternate Ricochet Site - Moving to Chooz

Due to the unfavorable signal to background rate at the MITR site an alternate reactor location had to be found and examined for its suitability, reusing many of the tools developed at the MITR site. Ideally the reactor site would still have a high CEνNS event rate while at the same time reducing the backgrounds that were present at the MITR site. Over the course of the Neutrino2018 conference, an alternate location of the Chooz reactor site (see figure: 4-14) was discussed as the Double Chooz experiment was in the process of decommissioning, opening the experimental hall for new experiments. The Chooz reactors are located in north eastern France and has been the site of the similarly named Double Chooz <NOTE: INSERT CITATION HERE> experiment for many years. <NOTE: briefly summarize the Chooz experiment> During the operation of Double Chooz there were two neutrino

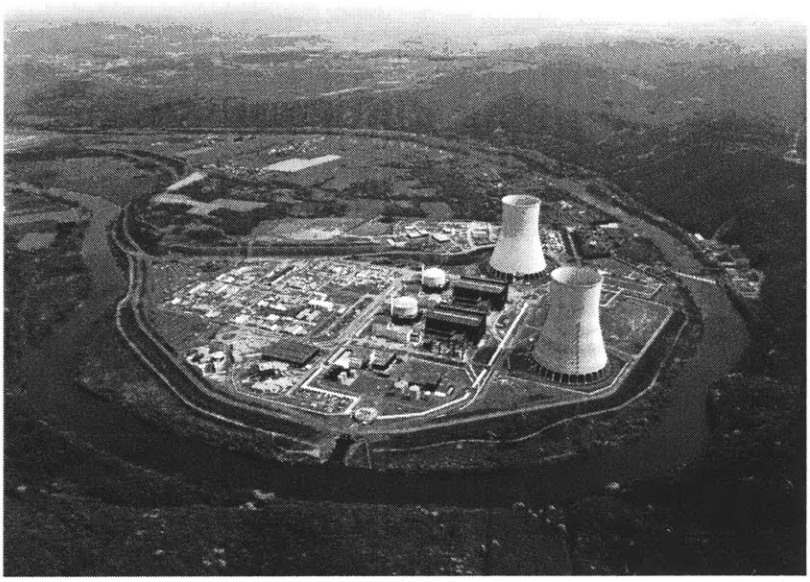

Figure 4-14: DoubleChooz Reactor Site

detector sites, appropriately named the near and far sites, with the near site only 350 meters from the reactor core. The first step in determining the suitability of this new location would be to rerun the CEνNS event rate calculation developed in the previous section to determine the what CEνNS event rate we could expect. Then we could develop a background model drawing from Double Chooz experimental data to determine the signal to noise ratio at the new site paying particular attention to the neutrons backgrounds.

Parameter	Value
Average reactor power	8.5 GW
Baseline distance to cores (near site)	355.39 m and 468.76 m
Overburden (near site)	140 m.w.e.
Cosmic Ray flux	$(3.74 \pm 0.21)\ \mu/\mathrm{m}^2/\mathrm{s}$ [99]

Table 4.2: Summary of the Double Chooz Reactor site parameters that went into the CEνNS event rate calculations

4.6.1 Expected CEνNS Event Rate at Chooz

In the proposed Ricochet CEνNS measurement setup at Chooz, we would deploy a 5+5 kg payload with 5 kg of Germanium and 5 kg of Zinc bolometers placed in the center of the near site experiment pit. As discussed previously with the CDMSlite detector setup, the threshold of your detectors plays a critical role in determining the expected signal event rate. For the initial setup we assume a detector threshold of 100 eV, but as shown in Table 4.1 any improvement of this threshold could result in the increase of our expected event rate by up to 50 percent. This 100 eV threshold was chosen as an achievable goal with current detector technologies, but future developments in Dark Matter detectors R&D have opened the exciting possibility of even lower thresholds. The choice of two distinct target materials would open up the possibility of probing the CEνNS event rate as a function of N, which would allow for probes of the nuclear structure functions as well opening up the possibly of additional beyond the standard model searches. Using the maximum reactor power for the Chooz site, one can calculate the maximum CEνNS event rate which ends up being close to 4.85 events per kg day see Figure 4-15 with the total proposed payload of 10 kg. Other materials were examined for their suitability as a Ricochet target detector and their respective event rates were calculated - see Table 4.3. One other important item to note is that this event rate assumes that you are running with your reactors at full power at all times, such that your duty cycle is nearly 100 percent. In real life, the reactors at the Chooz site change their power output depending on maintenance such as reactor refueling. It is very rare for both reactors to be turned off at the same time, which means that you will never be able to perform a "background-only" detector measurement. However; this has a unique benefit, namely that all the backgrounds we will discuss here are constant in time, while the CEνNS rate which we are attempting to measure correlates strongly with the reactor output over time. By specifically looking for this signal oscillation in time, one can then extract a CEνNS measurement more quickly than through a event rate excess alone, even with possibly large signal to noise/background ratios.

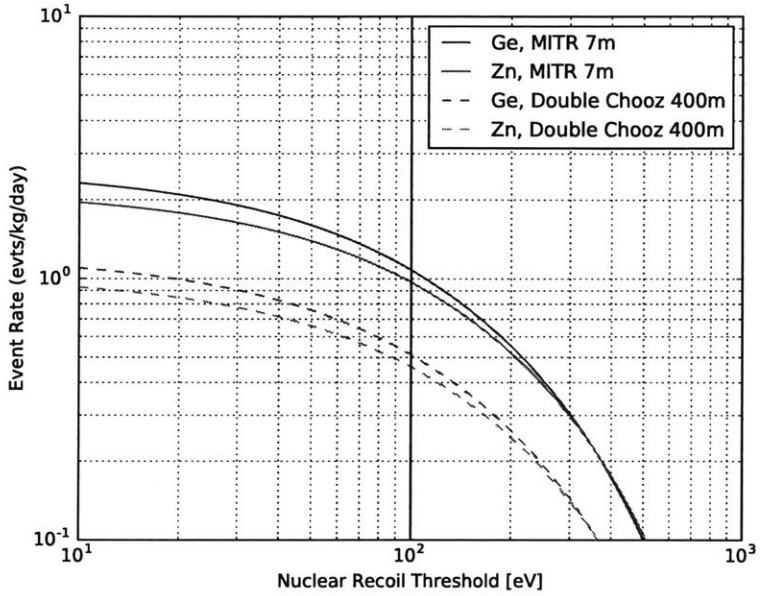

Figure 4-15: Differential event rate as a function of threshold for Ge and Zn at the Double Chooz site, notice the rapid die off of the event rate as threshold, again highlighting the need for the lowest possible threshold in all your detectors

Detector Threshold	Rate (per kg per day) Si	Zn	Ge	Os
50 eV	0.32	0.66	0.76	1.25
100 eV	0.26	0.46	0.51	0.55
200 eV	0.19	0.25	0.26	0.14

Table 4.3: The predicted CEνNS event rate for various detector materials and recoil threshold energies. Rates are calculated for fission fractions ^{235}U = 55.6%, ^{239}Pu= 32.6%,^{241}Pu = 7.1%, and ^{238}U = 4.7%. We assume an overall $\pm$5% uncertainty on the predicted rate of neutrino interactions. Taken from Table 1 in [96]

4.7 Neutrons Backgrounds at Chooz Site

Given the CEνNSevent rate, that we determined in the previous section one can now go about comparing that rate to background sources that we would expect at the reactor site using many of the same tools developed at the MITR site. In this analysis, we will focus on neutron backgrounds, which formed the largest background to the deployment of Ricochet at the MITR although additional background sources also make up a large part of the total background budget. In particular, we will look at neutrons induced by cosmic rays striking the environment surrounding the near site. Cosmic rays are an umbrella term for a wide variety of very high energy cosmic radiation that once it reaches earth, results in a shower of additional particles that can then form a background for many different experiments. The incident energies associated with the initial cosmic radiation can reach upwards into the range of 10^6 GeV, which opens up various production mechanisms to generate extremely high energy daughter particles. Experiments such as the Pierre Auger Cosmic Ray Observatory [100] have nearly 1660 detectors which cover an area of approximately 24 km^2 in order to catch the largest possible percentage of one of these showers. One of the largest components of these showers are muons, which can individually have energies in the hundreds of GeV. These muons can then interact with the environment via a variety of mechanisms (see appendix in [101]) to generate additional daughter particles which can spall into your detector and contaminate your signal region of interest. In particular these muons have the potential to generate high energy neutrons, which from the previous section we showed could make an site unsuitable for a CEνNS search. The daughter particles produced by these reactions can have energies in excess of 100 MeV, with the majority being being produced at less than 10 MeV [102], still more than enough to induce signals in the CEνNSregion of interest. In order to determine the effect these induced neutrons would have we turned to the same toolbox that we had previously ultilized in the MITR feasibility study, particle physics simulation with GEANT4 [103].

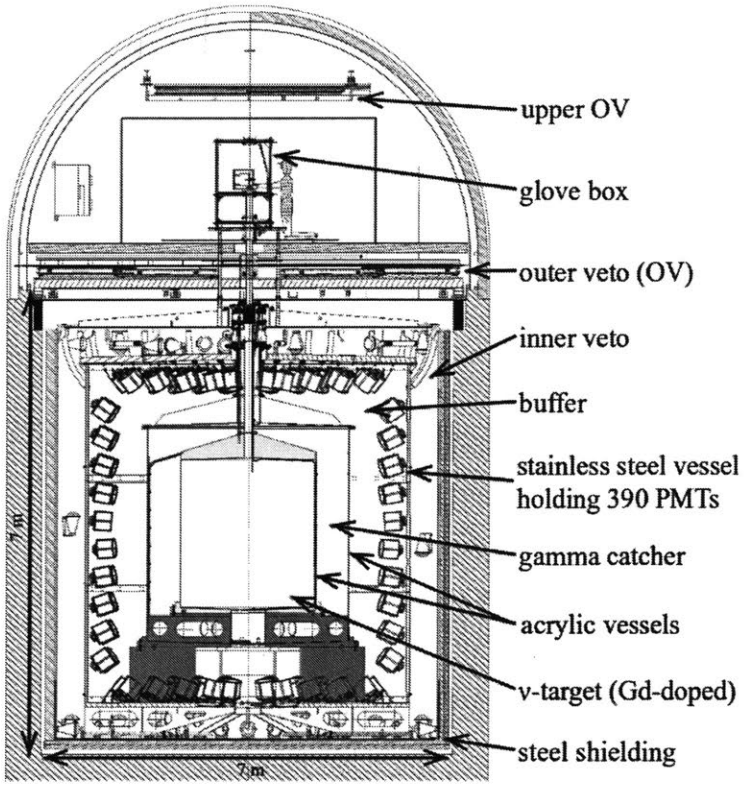

Figure 4-16: Cross Section of the Double Chooz detector taken from [106]

4.8 GEANT4 Chooz Simulation Setup

The Double Chooz detector represents nested layers of various volumes that are each designed to detector and/or shield a specific signal and/or background source. For these simulations we approximated the detector as a series of concentric cylinders for the ν-target, γ catcher and inner (water) veto as shown in Figure 4-16. The individual demensions that were used in the simulation are summarized in Table 4.4 and come from [104] or [105] unless otherwise noted. For the first part of our simulation we had to recreate the full Double Chooz experimental setup in order to recreate the cosmic ray data they had collected during their experimental run. We needed to exact the 'fudge factor' by which we would have to scale all our comic ray fluxes in order to mirror the actual conditions at the Double Chooz site. This meant we had to simulate the exact composition of the neutrino-target scintillator

Parameter	Value	Units	Notes
Chooz Detector Pit Surface Area	3.16×10^6	cm^2	Inner surface area of Pit used to house detector and various shielding layers, includes bottom surface and water tank geometry
ν Target Detector Surface Area	3.80×10^5	cm^2	Only sides of the ν Detector
ν Target Detector Surface Area (top)	1.78×10^5	cm^2	Only topside of the ν Detector

Table 4.4: The surface areas that would act as the source surface areas in the Geant4 simulation, for the (α-N) - induced spectrum discussed later we converted the inner surface area into a cylinder with wall thicknesses of 50 mm as those calculations required source volumes instead of just a surface.

Parameter	Value	Units	Notes
Dodecane	74.5	percent (mass)	$C_{12}H_{24}$
PXE	24.6	percent (mass)	$C_{16}H_{18}$
PPO	0.8	percent (mass)	$C_3H_6O_1$ 6 g/L by volume
Gd	0.1	percent (mass)	1 g/L by volume

Table 4.5: Makeup of the scintillator inside of ν Target scintillator (taken from [105])

as summarized in Table 4.5. Note the abundance of Carbon and Hydrogen in all the detector materials, increasing neutron scattering rates and prolonging the CPU-hours needed to run these simulations. Inside the γ catcher (inner veto) the same liquid composition was used, while mineral oil $C_{25}H_{43}$ was used to fill in all remaining detector components Important to note here is that we were not attempt to recreate any light yields or scintillation physics, each volume was treated independently and only used to record the energy deposited in each volume by environmental particles.

4.8.1 Geology of the Chooz Site

The Chooz site lies in the Andennes region of Europe, whose geology represents a melting point of geologic formations starting from sedimentary formations deposited during the Devonian era ($\approx 360 - 420MYr$ ago) when the north sea extended far inland from the modern day boundaries - see Figure 4-17b. Over time these initial

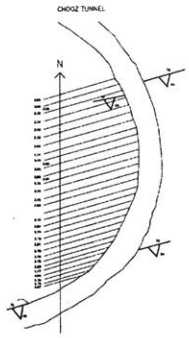

(a) Geology of the Chooz Site, labeled with the dip, strike and density of the rocks near the experiment. While there are variations of the rock geology across the entire experiment, the systematic errors as assumed to be small when taking the entire site in aggregate. Taken from [107]

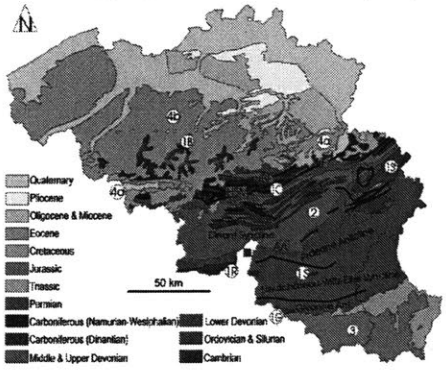

(b) Full Geology of surrounding region taken from [108]. The Chooz reactor site is highlighted in with a red square.

large scale sedimentary formations started fusing together into more complex strata with interchanging layers of sedimentary and metamorphic rocks. The Chooz reactor site, with the Meuse river surrounding it on three sides slowly exposed these strata resulting in the highly localized structures seen in Figure 4-17a. While fascinating for geologists, this results in careful studies required to account for all the different minerals present in all the various layers of rock that surround the near site. During commissioning of the Double Chooz experiment, the experiment undertook detailed studies of far site[11] summarized in the report [107] and presented in Table 4.6: Using

[11]We assumed that on the overall rock composition does not dramatically change from the near to the far sites

Mineral Name	Value	Units	Chemical Formula
Quartz	58	percent (mass)	SiO_2
Dodecane	19	percent (mass)	Al_2O_3
Rust	17	percent (mass)	FeO
Mg Oxide	4	percent (mass)	MgO
K Oxide	2	percent (mass)	KO
Overall average density	2.81	g/cm^3	

Table 4.6: Rock composition surrounding the near site pit, the abundance of Quartz can be attributed to the large portion of sedimentary rock present at the Chooz site

Element	Total mass	Units	Notes
Oxygen	1.87e7	grams	
Silicon	1.11e7	grams	
Iron	5.39e6	grams	
Magnesium	9.85e5	grams	Not included in final spectrum
Potassium	5.73e5	grams	Not included in final spectrum
Aluminum	1.10e6	grams	

Table 4.7: The total mass of the individual elements that go into the final neutron background spectrum described below. Total mass of all the elements 4.1e7 grams of rock based on the average rock density and the dimensions in the previous section

the mineral composition presented in Table 4.6, one can then work out the exact proportion of each element (by mass) that are present in the rock surrounding the near site. Note that this calculation assumes a 50 mm thick 'shell' surrounding the near site pit, taken to be the source of the (α-N) background discussed in the next section.

4.9 Input Neutron Spectra

4.9.1 Cosmologically Induced High Energy Neutrons

Most rare-event searches install their detectors as deep underground as possible to mitigate the effects of the naturally occurring cosmic ray background. As experiments grow in sensitivities, their background levels must drop correspondingly resulting in

experiments getting installed in ever deeper locations as discussed in [102]. Important to note is that the shallowest site used in this analysis is the Waste Isolation Pilot Plant or WIPP [109] site near Carlsbad, New Mexico at a depth of $\approx$ 1.6 km.w.e. Due to its shallow depth, the WIPP data was chosen as most closely mirroring the conditions that would be seen at Chooz site. In order to compare our simulated results to the data collected at the Chooz site, we needed to simulate the muon energy spectrum in Geant4 and then normalize the corresponding event rate to the Chooz data. Using the framework provided in [110], we can write down an analytic form to the induced neutron spectrum, parameterized by a_i and the average muon energy(E_μ), the values for each were determined experimentally for various sites:

$$\frac{dN}{dE}_{neutron} = A_\mu(\frac{\exp^{-a_0 E_n}}{E_n} + B_\mu(E_\mu)\exp^{-a_1 E_n}) + a_2 E_n^{-a_3} \tag{4.12}$$

$$B_\mu(E_\mu) = .324 - .641 * \exp^{(-0.014 E_\mu)} \tag{4.13}$$

The values used in out calculations are summarized in Table 4.8. Another important item to note is that while this is an empirically fitted function this particular formula breaks down for average muon energies below $\approx$ 50 GeV as $B_\mu(E_\mu)$ goes negative, which results in a differential spectrum with unphysical (negative) values. The actual average muon energy was measured to be 32.1 GeV([111]), which meant that for the Mei and Heim parameterization presented here, we had to cap the input value at 50 GeV. While average muon energy has an parameterization presented in [110] as a function of depth, this parameterization results in an unphysical spectrum at shallow depths, which prompted us to simply use the measured average muon energy at Chooz as presented in [111]. As an additional cross check, we also used a different neutron spectrum parameterization as presented in [112], using the same input parameters as before (all energies in MeV):

$$\frac{dN}{dE}_{neutron} = A(\frac{\exp^{-7E_n}}{E_n} + B_\mu(E_\mu)\exp^{-2*E_n}) \tag{4.14}$$

$$B_\mu(E_\mu) = .52 - .58 * \exp^{(-0.0099 E_\mu)} \tag{4.15}$$

Parameter	Value	Units	Notes
A_μ	1.71×10^{-10}	$\frac{1}{cm^2 \cdot s^1 \cdot GeV^1}$	Normalization Constant picked such that it matches the WIPP spectrum at E_n = 2 GeV
E_n	number	GeV	Neutron Energy
E_μ	50	GeV	Average Muon energy, which caped at 50 GeV due to the B_μ term
a_0	6.86		WIPP value
a_1	2.1		WIPP value
a_2	2.971e-13		WIPP value
a_3	2.456		WIPP value

Table 4.8: Table of the values that went into the neutron spectrum parameterization used in Equation 4.12

This parametrization, henceforth called the Formaggio parametrization, had the advantage that it would still produce a physical spectrum with an average muon energy of 32.1 GeV. Both these parameterizations are presented in Figure 4-18, both normalized to unity. Bear in mind for these plots, that the neutron spectrum we observed at the MITR only went up to 10s of MeV and that background was enough to contaminate our signal region, here the generated neutron energies reach much higher energies up to the cutoff value of 3.5 **G**eV. The flux of these higher energy neutrons does fall off much more quickly, but these higher energy neutrons will form the bulk of any events that will fall into our signal range of interest.

The final piece of the neutron puzzle comes from determining the overall neutron flux that we could expect at a specific depth (h). Equation 13 in [102] also provides us with the cosmogenic neutron event rate and when using the numbers provided in the paper one arrives at the following equation (height h is in km.w.e):

$$\phi_n[cm^{-2} \times s^{-1}] = (4.6 * 10^{-6}) \exp^{\frac{-h}{0.86}} \tag{4.16}$$

This results in a raw event rate of $4.2 \times 10^{-6} \frac{1}{cm^2 * s}$, multiplying by the surface areas of the side and the bottom of the water tank (see Table 4.4) one obtains an expected

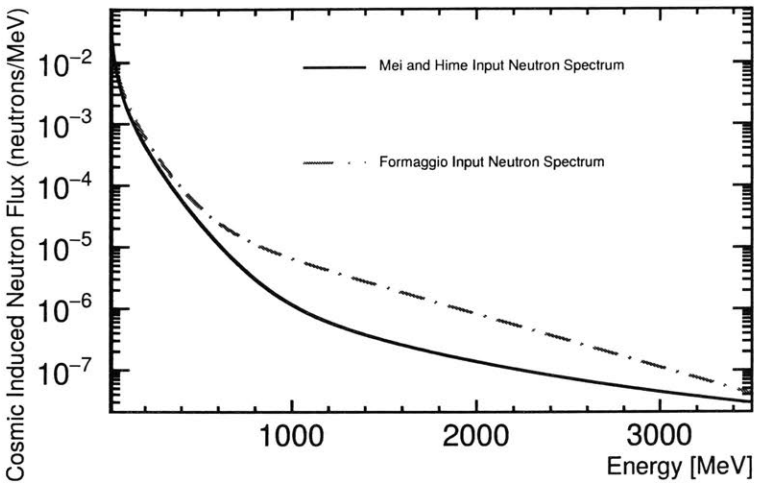

Figure 4-18: Formaggio and Mei Input Cosmogenic Neutron Spectrum parameterizations used for DoubleChooz neutron simulations

raw neutron flux of 1.2×10^6 neutrons/day.

4.9.2 (α, n) Input Neutron Spectrum

Another potential source of neutrons comes from neutrons emitted when the rock around the detector pit are bombarded by αs, that occur naturally in the rock, generating a neutron spectrum in the 1-10 MeV range. We refer to these neutrons as alpha-induced neutrons or (α, n). Starting with the rock composition discussed in the previous section and using the induced neutron flux for each element listed in [110], one can generate a neutron spectrum for each element present in the rock at the Chooz site. Using the masses of the various elements calculated previously one can then weigh each spectrum component to generate a composite (α, n) neutron energy spectrum shown in Figure 4-19, which when results in an event rate of of 2.0×10^4 neutrons/day, well below the cosmogenic neutron flux discussed in the previous section. Note that when simulating the neutron flux we simulate the neutrons coming from a 50 mm thick shell around the entire bottom half of the pit volume. Also all neutrons are simulated with an isotropic velocity vector distribution at their starting point, which means most of the generated neutrons will initially be pointing towards

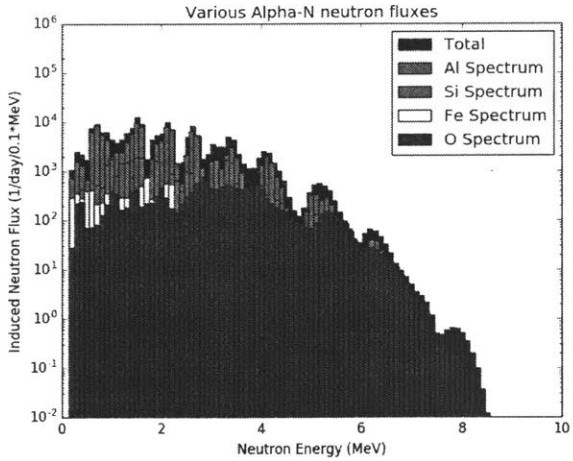

Figure 4-19: Input (α, n) differential Spectrum for Chooz simulation, note that each elemental contribution is weighed by the total mass of each element present in the rock surrounding Chooz. Mg and K were not included in the final calculation as their (α, n)contributions were at least an order of magnitude below these contributions

Flux Source	Value	Units	Notes
μ Induced Neutron Flux	1.2e6	$\frac{neutrons}{day}$	Number of neutrons coming from pit surface
(α, n) induced Neutron Flux	2.0e4	$\frac{neutrons}{day}$	

Table 4.9: Expected neutron flux using the parametrization presented in [110]. The true value of the flux would have to be normalized via the Chooz Gd-tagged events discussed in the next section.

the outside walls when they are first generated.

The final expected event rates from the pit stemming from both cosmic ray and (α, n) induced neutrons and are summarized in Table 4.9. This event rate was only used to determine a rough order of magnitude estimate for the relative fluxes that we could expect, as particularly for the Mei parameterization we are using the parameterization at an extremely shallow depth compared to the data that it was fit to. This was then taken into account in the systematic error calculation, which is beyond the time I have for this thesis, but can be discussed upon request.

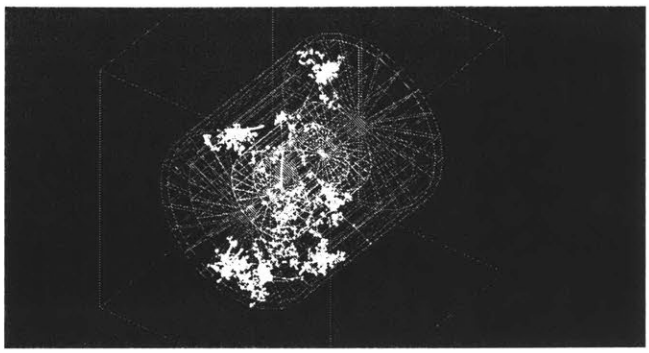

Figure 4-20: Example Output for the Chooz Simulation. These simulations were computationally very intensive and required the combined computing power of our local 40 core cluster together with the 200+ core 'hot potato' cluster cobbled together and generously loaned out to us by the MITERS student club

4.10 Neutron Event Rate Calculation

Using the (α, n) and cosmogenically induced neutron spectra as inputs, we simulated the full Chooz detector to perform a cross check with the number of fast neutron events measured in [113]. The Chooz main detector volume contains some Gadolinium specifically for the purpose of detecting fast neutrons that make into the neutrino detector, producing a clear γ signal that the Chooz PMTs can then pick up. We performed comprehensive analyses utilizing Gd-captures only [113] or Gd and H-captures [114] in Chooz and only the most pessimistic scenario was retained (Gd-captures only). Using both the Mei and Formaggio input spectrum parameterizations we determined the following benchmarked neutron fluxes (Table 4.10)for the near site detector pit: Using these benchmarked event rates, we could then determine the expected neutron fluxes coming off the walls for the cosmogenic induced neutrons, which would form the the dominant background we observed.

4.11 Ricochet at Chooz Simulation Results

Once we had the benchmarked neutron rate we could proceed to replace the Chooz geometry with the proposed Ricochet deployment in the near site pit. This meant an ADR geometry with a 9x9x9 cm Zn crystal (corresponding to about 1 kg sample)

Parameterization	N_{Sim}	N_{obs}	Benchmark Neutron Rate (per day)
Mei (1 MeV Min Energy)	992 M	15	265 M
Formaggio (10 MeV Min Energy)	64 M	19	13.5 M

Table 4.10: Neutron event rate normalized to the observed rate in the Gd analysis performed in Chooz. Important to note that one can not directly compare the two parameterizations due to the different minimum energies associated with input neutrons. The N_{obs} reflects events in the simulation that make it into the region and at follow a similar event topology as the Gd-neutron tagged events in terms of energy deposited in the region of the interest.

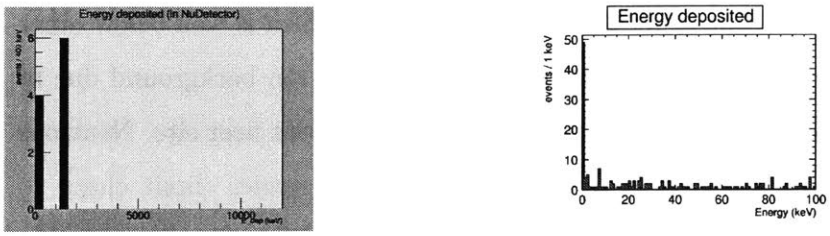

Figure 4-21: (a) Neutron events that enter into the detector crystal, generated by (α, n) input spectrum. 9.6 M events simulated, 10 total events enter detector crystal. Coupled with the low initial (α, n)flux this means that the total (α, n)contribution to the final background budget will be small. (b)Ricochet simulation energy deposited in the detector crystal, cosmogenic (Formaggio Parameterization) input spectrum. Shown here are the results for 450M events simulated, region of interest for our search [0.1, 1] keV

floating in the middle of the pit, surrounded by a 3 meter thick (2 meters on the bottom) wall of water. This water wall would act as shielding for neutrons, but also many other background processes that we will not discuss here. For the (α, n)contributed we determined that we would only see 10 events in the region of interest (0.1 - 1 keV) in our detectors, with 9.6 M events simulated, corresponding to <0.01 events per day in our detectors. Once we simulated 450M events with the Formaggio parameterization we were able to determine that the predicted neutron background in our detectors would be 3.0 ± 1.0 $\frac{events}{day}$ for the 10 kg deployment at the Chooz site. An additional check, using the parametrization of Mei and Hime [102] we were able to produce a 95 percent confidence level of a neutron background of less than 4 $\frac{events}{day}$ in the same region of interest).

Background Source	Rate ($\frac{events}{kg*day}$)
Cosmogenic Induced Neutron Flux	0.3 ± 0.1
(α, n) induced Neutron Flux	< 0.01

Table 4.11: Total neutron background event rate

4.12 Chooz Site Summary for Ricochet

Combining existing measurements of the rock composition at the Double Chooz far site [115] and simulations of the U/Th decay spectra (using GEANT4 [103]), we are able to model the neutron spectrum from (α, n) reactions, which is well below other contributions. A similar procedure is used to assess the neutron background due to cosmogenic activity surrounding the cavern of the Double Chooz near site. Neutrons from cosmogenic activation tend to possess much higher energies (limit closer to ≤ 100 GeV), and pose a more serious background source. The initial neutron energy spectrum is modeled to follow the parametrization as reported in [116], assuming a generating muon energy of 32.1 GeV. The cosmogenic neutron spectra are propagated through GEANT4-based simulations of both the Double Chooz near detector [104] and the Ricochet-style detector as shown in Figure 4-22. The number of events observed for the Double Chooz simulation is normalized to the fast neutron rate as measured by the Double Chooz near detector, thereby providing the equivalent run time of the simulation. For the Ricochet-style detector/simulation, we assume a cylindrical water shield with 3.25 meters of water buffering the detector cryostat on its side, and 2 meters of water shielding from the bottom. The estimated background rate from fast neutrons is $(2.3 \pm 2.3) \times 10^{-4}$ neutrons/kg/eV/day, leading to a total rate of (0.3 ± 0.1) neutrons/kg/day for recoil energy depositions between 0.1 and 1 keV. For the total background budget expected for a Ricochet deployment, please refer to Table 4.12, which also includes several background sources not discussed in this thesis. For full details on these sources please read [96]

At first glance it may seem as though the signal to background might be unfavorable at the Chooz as well, due to the correlated/uncorrelated nature of the signals and backgrounds respectively, one can more easily extract the signal from a rate mea-

Table 4.12: A summary of correlated and uncorrelated backgrounds to reactor power on a 5 kg Ge + 5 kg Zn recoil detector located at the Chooz near site underground hall. The region of interest (ROI) is defined between 100 eV and 1 keV. The tritium estimate(†) on differential rate includes only beta-spectrum contribution. From [96]

Background Source	Rate ($kg^{-1}day^{-1}eV^{-1}$)	Total Rate in ROI (events/day)
Uncorrelated Rate		
Gammas (Compton)	$(2.0 \pm 0.2) \times 10^{-4}$	1.8 ± 0.18
Fast Neutrons	$(3.3 \pm 1.1) \times 10^{-4}$	3.0 ± 1.0
(α, n)	$< 1.1 \times 10^{-5}$	< 0.1
β decays from ^{210}Pb	$(9.3 \pm 3) \times 10^{-4}$	8.8 ± 2.8
$^3H^\dagger$	$(0.36 \pm 0.04) \times 10^{-4}$	0.5 ± 0.05
^{206}Pb	$(2.6 \pm 0.4) \times 10^{-5}$	0.25 ± 0.03
$^{70}Zn\beta^-\beta^-$	$(3.9 \pm 7.0) \times 10^{-5}$	< 0.1
$^{64}Zn\beta^+\beta^+$	$(1.3 \pm 3.9) \times 10^{-6}$	< 0.1
$^{76}Ge\beta^-\beta^-$	$(4.0 \pm 0.3) \times 10^{-8}$	< 0.1
Total Uncorrelated Rate		14.4 ± 4
Correlated Flux Rate		
CEνNS		4.85
$\bar{\nu}_e e^-$-scattering		9.2×10^{-5}
Total Correlated Rate		4.85 ± 0.25

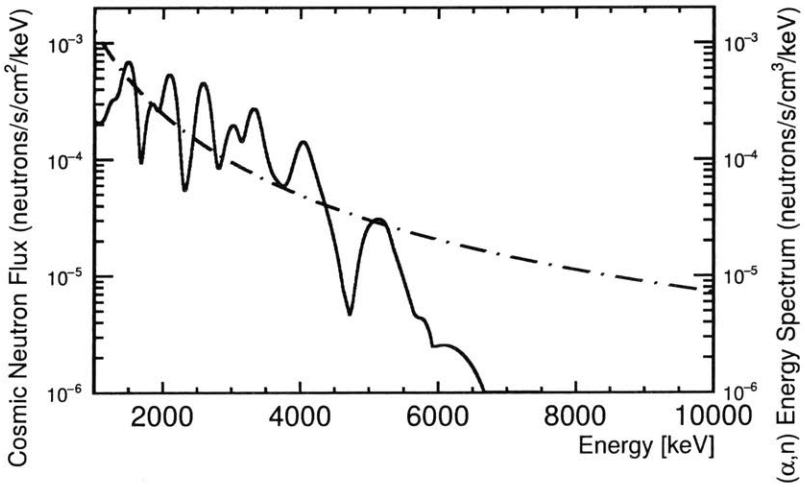

Figure 4-22: Input Spectra (cosmogenic and (α, n)) used for DoubleChooz neutron calibration and background simulations, both spectra are normalized to 1. Taken from [96]

surement by dividing the measurements into time bins. By looking at the change in rate as a function of time in detectors and correlating it with changes in the expected CEνNS due to reactor refueling/maintenance etc..., and noting that most of these backgrounds remain constant in time, one can extract a 5 σ CEνNS signal with only 500 kg days of exposure ($\approx$ 50 days of running with proposed Ricochet deployment). Once this first goal has been achieved, it then becomes possible to start the characterization of CEνNS , probing several standard model physics models and simultaneously opening the door to the numerous applications of CEνNSsuch as reactor monitoring with small scale detectors.

4.13 Conclusion

The Ricochet experiment seeks to measure CEνNS , a tree-level Standard Model process, using a nuclear reactor as a neutrino source. The measurement and characterization CEνNS would have several applications in particle physics as well as applied applications such as reactor monitoring. This process, while having a fairly high cross section, requires the use of low threshold detectors such as the ones used on dark matter experiments such CDMS. Due to the low threshold requirements, many possible background sources must be taken into account, in particular neutrons can mimic a CEνNS signal and thus contaminate your signal region. The MIT (research) Reactor (MITR), was the site initially selected for a first deployment of the Ricochet experiment, with the main advantage of having a deployment location that was only 7 meters from the reactor core, which would allow for a high CEνNS despite the modest power output. This proximity also had the drawback that neutrons from the reactor core would interact with the Ricochet detector, prompting the need for neutron monitoring at the proposed deployment site using Neutral Current Dectectors (NCDs) borrowed from SNOlab. We successfully deployed NCDs at the MITR site in order to measure the neutron background across several orders of magnitude. After applying pulse shape discrimination event-selection criteria we extracted an event rate for each of the 6 different NCD Bonner cylinder shielding configurations, each

of which were used to probe different components of the overall neutron spectrum. We applied an optimized maximum likelihood coupled with a MCMC (discussed in appendix) analysis framework to characterize the high correlations between the various neutron bins in the final reactor on, reactor off and $^{252}_{98}$Cf calibration data. Using the final unfolded neutron spectrum we simulated a 1 kg Ricochet deployment with a Zn target at the MITR with and without 30 cm of polyethylene shielding. While the raw unfolded spectrum points to an intrinsic neutron background rate higher than the expected CEνNS signal rate, which 30 cm of shielding this background event rate was brought down closer to the CEνNS signal level as shown in Figure 4-13. This low signal to noise ratio makes a CEνNS signal detection search challenging, prompting a search for an alternate site, while continuing to use the MITR site for Ricochet Bolometer R&D efforts. The Double Chooz experiment site, located near the nuclear power station in Chooz,France vacated their experimental halls opening the possibility of deploying Ricochet to France. The longer baseline distance of 350 meters coupled with the much higher expected neutrino flux meant that the expected CEνNS event rate (4.85 events/day) would be similar to the rate expected at the MITR. This longer baseline would have the added benefit of shielding the Ricochet experiment from the direct reactor core neutrons. However; the dominant neutron background now would take the form of neutrons induced from cosmic rays and α particles in the rock surrounding the near site pit. We generated expected neutron spectra for both the cosmic induced and the α induced neutron spectra based on parameterizations found in literature. Geant4 simulations were run to perform cross checks between these incoming neutron spectra and the data recorded by the Double Chooz experiment as well as determining our systematics errors. Once the cross checked were performed with the Double Chooz geometry, we could then change to the proposed Ricochet geometry to be deployed in the near site pit. With these simulations we determined that the main neutron contribution would be 3.0 ± 1.0 events/day in the signal region of interest stemming from the cosmogenic induced neutrons, while the α induced neutron spectrum would be negligible. Coupled with the other possible background sources (see Table 4.12), it might seem at first glance

that the Chooz site would be unsuitable for the deployment of Ricochet, however; most of the backgrounds are uncorrelated with the CEνNS rate which is tied to the reactor output. As the reactor output changes as a function of time, it therefore becomes possible to unfold up to a 5 σ CEνNS signal with only 500 *kg days* of exposure at 100 eV threshold.

Chapter 5

Measurement of λ for Neutrino-less Double Beta Decay ($0\nu\beta\beta$) Searches

"..whilst the number of accurate instruments was daily increasing, we were still ignorant"
— Alexander von Humboldt, Personal Narrative of Travels to the Equinoctial Regions of America, During the Year 1799-1804 - Volume 1

5.1 Introduction to Neutrino Mass

Whenever a new particle is discovered one of the first questioned asked by the physics community is, "What is its mass?". Within the Standard Model (SM), the neutrino has taken a very different discovery path compared to other particles. The theory behind neutrinos has been established for over 80 years and experiments have only been able to measure it for 50 years. Yet for all the neutrino experiments currently running, the neutrino's mass remains an unknown value, we have only been able to place upper (and a lower) limits on it. One of the great breakthroughs in particle physics from the past 20 years was to determine that the neutrino does have mass, but the exact mechanism by which the neutrino obtains this mass still eludes us. All this is what makes the neutrino one of the great "known unknowns" of the SM.

We also do not know how best to fit the neutrino into the framework that we have used to describe the other particles in the SM. One possibility is through the

Majorana mechanism, which postulates that a neutrino and an anti-neutrino are actually the same particle. The measurement of neutrinoless double beta decay ($0\nu\beta\beta$) offers a possible way to determine if the neutrino follows this mechanism. The conversion between a measured $0\nu\beta\beta$ half-life and an effective Majorana neutrino mass ($m_{\beta\beta}$)requires the use of complex nuclear modeling to account for the complex interactions occurring within the nucleus during $0\nu\beta\beta$. All these nuclear calculations are highly dependent on many parameters, but we will focus on one parameter in particular λ. λ is defined as the ratio between the axial (g_A) and vector coupling strengths (g_V)[1] during a transition. The measurement of this value would provide insights into the dynamics involved in weak decays. In the past, the value of this parameter has been assumed to always be the value measured in free neutron decays, but recent work has pointed out that this value gets quenched in larger more complex systems such as those in $0\nu\beta\beta$ decays.

There has yet to be a definitive measurement of $0\nu\beta\beta$ in any nucleus, making it difficult to determine to what degree quenching takes a role in $0\nu\beta\beta$. The modeling of a second order weak decay process, such as $0\nu\beta\beta$, requires an understanding of the numerous intermediate states available to this process, each of which are affected to different degrees. One method to measure the effect of quenching on $0\nu\beta\beta$ is to look at the effect quenching has on specific single-β decays which can act as proxies for some of the intermediate states in $0\nu\beta\beta$. One particular single-β decay that has a similar dependence on the value of the quenching and has similar nuclear structure to isotopes used in $0\nu\beta\beta$ searches is In-115. What follows is a measurement of this nuclear quenching factor in In-115 and a discussion of its effect on the determination on an effective neutrino mass $m_{\beta\beta}$ based on $0\nu\beta\beta$ half-live measurements performed by various experiments.

[1]Note that in many references the vector coupling strength is normalized to 1 as a result of the Conserved Vector Current (CVC) hypothesis, which makes λ equivalent to g_A

5.2 History of the neutrino

In 1930, with a now famous letter to the members of a conference at the Eberhard Karls University of Tübingen, Wolfgang Pauli proposed a existence of a light neutral particle that could explain the odd shape of the single β decay spectrum. β decay represented a unique challenge to both theoretical and experimental physics at the time. At its core β decay represents the turning of a neutron into a proton, using just charge conservation one might expect the following equation to represent this neutron conversion process:

$$n \rightarrow p + e^- \tag{5.1}$$

When the single β decay spectrum was studied for the first time, experimentalists observed a spectrum instead of fixed energies for the protons and the electrons as one would expect for a simple decay into two daughter particles as both masses were known and fixed. Only with the inclusion of a third particle, would there be a distribution (read a spectrum) in the energy carried off by each daughter particle as the three daughter particles share the energy between them, but where was the third particle? Nils Bohr was prepared to throw conservation of energy out of the window[2] in order to explain this phenomenon. With the development of quantum theory, another issue was seen with 5.1, namely that of the conservation of spin. Protons, neutrons and electrons are fermions with spin $\frac{1}{2}$ and no matter how you add together the spins of the proton and the electron daughter particles, you can never recover the original neutron spin of just $\frac{1}{2}$. All this pointed to the need for an additional particle, which somehow eluded detection. This is where Pauli's proposal came in to modify Equation 5.1 to look like:

$$n \rightarrow p + e^- + \overline{\nu_e} \quad ^3 \tag{5.2}$$

[2]For the third time I might add...

[3]The bar over the neutrino means that an anti-neutrino is emitted, something that will become more important during our discussions of the Majorana neutrino, for right now is it merely a symbol

5.2.1 Mass Measurements

Almost as soon as this little neutral particle was proposed [4], measurements were undertaken to first detect the particle and then to measure its mass. The first detection occurred at the Savannah River Reactor in 1956, discussed in the previous chapter [117]. Various experiments were then performed to search for neutrino mass, but no evidence was found. For this reason as the Standard Model came into being in the 1960's and 1970's, the neutrino was incorporated into this framework as a massless particle [118]. One of the other features about neutrinos that I have glossed over are that there are three different types of neutrinos, e,μ and τ, characterized by the reactions they take part in and their corresponding charged leptonic partner. Neutrinos that, for example, take part in reactions inside of nuclear reactors and/or in fusion inside the sun tend to fall into the e (for electron) category and are labeled as ν_e, as they are often emitted with a corresponding electron. Starting in the late 1960's the famous Homestake Experiment in South Dakota undertook a simple elegant measurement of the electron neutrino flux coming from the sun via the induced reaction:

$$^{37}Cl + \nu_e^{solar} \rightarrow ^{37} Ar + e^- \tag{5.3}$$

This is the same reaction as Equation 5.2, only now instead of emitting a neutrino, a neutron in the Chlorine absorbs a solar neutrino transforming into a proton and an electron, which turns Chlorine into Argon. The large number of chlorine targets (remember that neutrino interaction probabilities are small) could be easily provided with large tanks of perchloroethylene (used in dry-cleaning). The induced Argon atoms would be tagged by their subsequent radioactive decays, which would be measured at the end of every month. Each Argon decay therefore corresponded to a known proportion of the total expected flux of solar neutrinos, calculated via complex solar models. Just to highlight the difficulty in detecting these events, the total expected neutrino-induced Argon production rate was measured to be approximately 0.5 events/day [119] Month after month, the argon measurements pointed to a simple

[4] Initially this new particle was to be called the neutron, but with Chadwicks discovery of what we now know as the neutron, Fermi proposed a new name of 'neutrino' or little neutral one

fact every flux measurement of these solar neutrinos seemed to fall short by a factor of three resulting in the so-called "Solar Neutrino Problem" The nuclear models of the sun were soon confirmed by other experiments/observations and other solar flux measurements pointed to a similar shortfall. This meant that while the solar models predicted the correct number of neutrinos produced at the sun, as they traveled towards the earth, something happened to these neutrinos. In 2002, the SNO experiment[5] [120] undertook an additional measurement of the solar neutrino flux, but this time building their experiment to collect data from all three flavors/types (e,μ and τ) of neutrino simultaneously. The SNO experiment observed that the combined fluxes of all three types of neutrinos matched the solar prediction. The KamLAND [121][122] experiment then measured a deficit of electron anti-neutrinos coming from a nuclear reactor showing that even these reactor neutrinos were changing into other flavors as they traveled. The various probabilities for neutrinos changing from one flavor to another have been summarized and encoded into the Pontecorvo-Maki-Nakagawa-Sakata (PMNS) matrix,U, [123][124] and using the parameterization in [125].

$$U = \begin{bmatrix} c_{12}c_{13}e^{-i\frac{\alpha_1}{2}} & s_{12}c_{13}e^{-i\frac{\alpha_2}{2}} & s_{13}e^{-i\delta} \\ (-s_{12}c_{23} - c_{12}s_{23}s_{13}e^{i\delta})e^{-i\frac{\alpha_1}{2}} & (c_{12}c_{23} - s_{12}s_{23}s_{13}e^{i\delta})e^{-i\frac{\alpha_2}{2}} & s_{23}c_{13} \\ (s_{12}s_{23} - c_{12}c_{23}s_{13}e^{i\delta})e^{-i\frac{\alpha_1}{2}} & (-c_{12}s_{23} - s_{12}c_{23}s_{13}e^{i\delta})e^{-i\frac{\alpha_2}{2}} & c_{23}c_{13} \end{bmatrix}$$

where:$c_{ij} = \cos\theta_{ij}, s_{ij} = \sin\theta_{ij}$ and α_i, δ are three CP-violating phases that we will discuss more later. I am going to assume that the reader is familiar with the specific details of neutrino oscillations and how to use the PMNS matrix to calculate the various probabilities of converting for example a ν_e into a ν_τ. The conclusion, neutrinos were changing as a function of time which has profound implications for neutrino physics. Since the only way that a particle can experience time is if that particle does not travel at the speed of light, which means that it is getting slowed down by its intrinsic mass. Neutrinos with mass had broken one of assumption encoded into the Standard Model, but what was the mass of these neutrinos?

The very first limits on the neutrino came from mass/decay width measurements on

[5]Yes the same experiment that lent us the NCDs for the Ricochet measurement

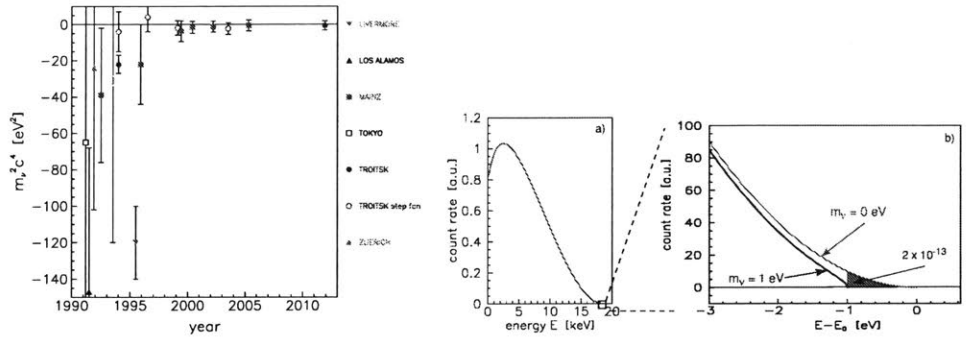

Figure 5-1: (a) Compilation of direct neutrino mass measurements from 1990 onwards. The measurements here combine data taken from Magnetic and Electrostatic measurements. For all individual references for each experiment I point the reader towards Figure 7 in [127] (b)Tritium endpoint measurement example used in the KATRIN experiment. Note the scales of the overall beta spectrum compared with the energy endpoint we are attempting to measure. Taken from [128]

the weak force neutral current mediator, the Z^0 boson, putting the first limits on neutrino mass at around $\lesssim \frac{m_Z}{2}$ or 45 GeV[6]. In addition, all experiments sensitive to the neutrino mass seemed to point a massless or at the very least an extremely light neutrino mass, which meant that for most practical purposes the neutrino was massless. There were extensions to the standard model that would add mass to the neutrino, but for many years there was no direct evidence that the neutrino had mass, leaving these theories as an sidenote. Starting in the late 1980s, there was a renewed interest in directly measuring the neutrino mass to confirm or deny the assumption that the neutrino was actually massless. Supernovae, discussed in more detail in section 3.3.3, specifically SN1987a, provided an early bound on the neutrino mass, by looking at the delay between the light and neutrino signals from SN1987a. The resulting time delay indicated an upper limit on the neutrino mass of approximately 5.8 eV, with further improvements proving to be difficult due to uncertainties related to supernova evolution [126].

Lab based measurements in the 1990's (summarized in Figure 5-1) also began to push down upper limits on the neutrino mass with some initial positive signals later

[6]Current the mass limits lie in the range of $\lesssim .120$ eV, which is an amazing reduction in orders of magnitude considering we started in the Giga range

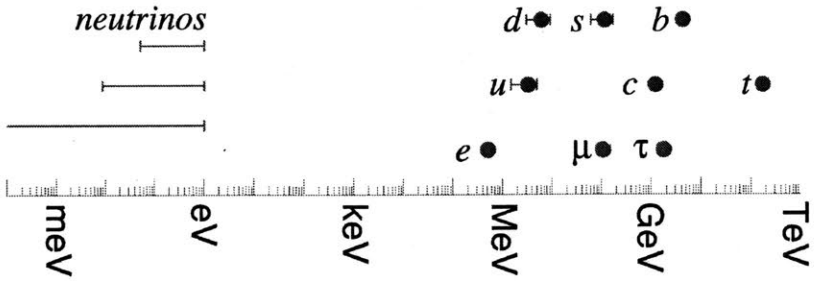

Figure 5-2: Overview of the mass for all the constituent fermions in the Standard Model(SM). While most ferimons have masses above $\approx$ 1 MeV, neutrinos prove to the be exception to the rule. This is still one of the major open questions in particle physic todays. Also note that the neutrino masses are the only ones that have yet to be pinned down, we can currently only set upper bounds on their masses. Note the log scale. Figure from [129]

being disproven due to misunderstood systematics. The majority of these experiments attempt to directly measure the mass of the neutrino by looking at the end point of a low-energy beta spectrum, for example Tritium beta decay with its end point of 18.6 keV - see Figure 5-1. The non-zero mass of the neutrino would appear in these experiments as a shift from the normal endpoint of the spectrum as the neutrino "soaks" up some energy to create its mass via the famous relationship $E = mc^2$. This method of directly measuring the neutrino mass via spectroscopy has started to run into issues with scalability as seen with the massive KATRIN experiment experiment [128], posed to start data taking in the next few years. At the time of these thesis, we have yet to assign a mass value to the neutrino, we can only set upper limits to the mass of the neutrino. With the latest limits on the neutrino mass, the mass separation between neutrinos and their nearest SM partners ends up being about about six orders of magnitude. To put that in perspective, the total loaded running weight of a German Railways Class 01 steam locomotive[7] is about 120,000 kgs. If we equate the mass of the locomotive to the lightest measured fermion mass (the electron), the neutrino mass limits at the moment put the neutrino mass somewhere in the vicinity of an apple- see Figure 5-2 Why neutrinos end up being so much lighter than their lepton partners is still an open question in physics, but one way we might

[7]Wikipedia Link

be able to shed light on this is by determining a mechanism within the Standard Model (SM) through which neutrinos get assigned their mass.

5.2.2 Neutrino Mass from other measurements

Direct spectrum endpoint measurements from experiments such as KATRIN or Project8 are just one probe into neutrino masses. Precision measurements of the CMB offer another probe into the neutrino mass by measuring the cumulative effect of a high density of neutrinos on the early structure formalization in the universe. Broadly speaking, if you make neutrinos too light they simply fill out the entire universe equally like air in ballon. However; as you increase their masses you can create over and under densities of neutrinos where gravity then forms clumps of higher density which contributes to seeding the early structures of the universe. These early structures can then help form the anisotropies seen in the CMB as shown in Figure 3-4. Working backwards one can then try to set a limit on the neutrino mass [130][131]. This method does have its drawbacks, any limit you set on the neutrino mass using this method is highly dependent on how you set up your initial interactions between neutrinos and regular matter and how you propagate through those interactions. This means that any comparison between results from say PLANCK [132] and results from KATRIN or $0\nu\beta\beta$ searches (discussed in the following section) must be taken with a fair grain of salt.

5.3 Current $2\nu\beta\beta$ and $0\nu\beta\beta$ measurements

While so far we have only discussed single β decays, there exists a small subset of isotopes where two βs are emitted from a decaying nuclei, resulting in the following reaction:

$$(Z, A) \rightarrow (Z + 2, A) + 2e^{-} + 2\bar{\nu}_e \tag{5.4}$$

The Standard Model predicts the lepton-conserving process ($2\nu\beta\beta$), first published by Maria Goeppert-Mayer in 1935 [133], but experimental verification of this process

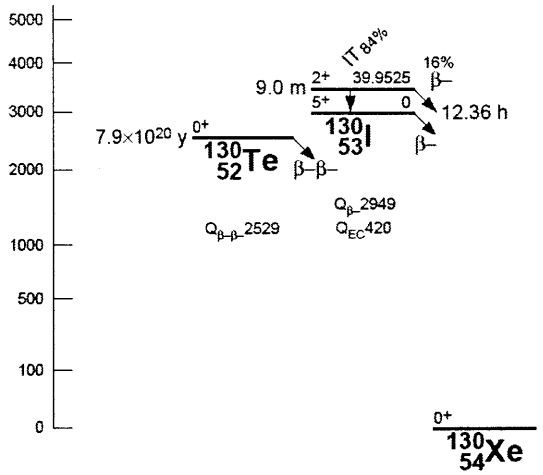

Figure 5-3: A = 130 Isobars figure adapted from [135]

had to wait until the mid-1980's - see Table 3 in [134]. Double β decays only occur at a suppressed level compared to single β decays due to the second order nature of this process. It is this suppression that results in the extremely long half-lives of $2\nu\beta\beta$decay (measured at 8.2×10^{20} years in CUORE-0[38]), making this the slowest *measured* process in physics[8]. This means that $2\nu\beta\beta$ will only dominate the overall decay if the single β process is kenematically or forbidden through some other mechanism this means only a handful of isotopes fulfill these conditions.

From Figure 5-3 there is one particular item to note, the transition from Te-130 to Xe-130 is not a direct double β decay, rather it does pass through intermediate nuclear states, which have higher angular momenta. This means that the "effective" angular momentum change that $2\nu\beta\beta$ and $0\nu\beta\beta$ have to overcome result in highly (5+) forbidden decays. This explains the large gap between the theory proposal and the experimental verification. In terms of experimental signal, $2\nu\beta\beta$ decays act as a five body decay with Q-values of $\approx$ 1.5+ MeV. The rarity of this process coupled with the fact that neutrino have such tiny interaction cross sections, means that the two emitted neutrinos are often ignored and experimental searches focus on

[8]barring proton decay, I said measured

detecting the emitted electrons or the resulting daughter nucleus. The shape of the resulting combined electron spectrum can be approximated via the Rosen-Primakoff equation [136] (all energies in MeV):

$$\frac{dN}{dE} = CE(Q-E)^5(1+2E+\frac{4}{3}E^2+\frac{E^3}{3}+\frac{E^4}{30}) \tag{5.5}$$

Note: E = total energy of both electrons

For all energies between 0 keV (neutrinos carry alway the entire Q value of the reaction) up to the Q-value of the reaction (neutrinos emitted at rest). For each one of the $2\nu\beta\beta$ decay isotopes there is an additional decay channel that mirrors $2\nu\beta\beta$ except that no neutrinos are emitted during the decay thus the name neutrino-less double beta decay ($0\nu\beta\beta$), first proposed in [137]. If observed, this process would provide the first evidence for a process that breaks lepton conservation. In addition, this decay channel would test the idea that neutrinos are Majorana fermions[9] (aka they are their own antiparticles - see next section). Finally an observation of $0\nu\beta\beta$ would allow for an alternate measurement of the neutrino mass mass based on the observed decay rate. For a fuller discussion of the theory details behind both $0\nu\beta\beta$ and $2\nu\beta\beta$, I point the reader to [138].

5.3.1 Neutrino Mass Theory

All the discussions on the neutrino mass have glossed over the fact that within the Standard Model, neutrinos are massless. Within the Standard Model, the standard procedure when discussing a new particle is to summarize all the various interactions (summarized as a field Ψ[10]) that it can undertaken in the form of a Lagrangian. This describes motion in all three (and later four) dimensions. For all other fermions, that we have discussed so far, a specific mass term often appears upon writing out this

[9]The observation of $0\nu\beta\beta$ would imply that the neutrino is a Majorana particle, but there are a few theories in the literature that allow for $0\nu\beta\beta$ without the need for a Majorana neutrino mass

[10]In this thesis, we will not go too in depth about what this field actually or how you construct them, for now we will simply assume you have created an ansatz and go from there

Lagrangian namely:

$$\mathcal{L} = \alpha\bar{\Psi}\Psi + \text{other terms} \tag{5.6}$$

where Ψ represents some field that describes the particle/interactions in question and α is just some collection of constants. Getting a theory into this form can often be tricky, requiring redefinitions of parameters/normalizing to non-zero ground states, but in the end all fermions, so far, have a term like this. α is the mass term which describes the mass of the fermion in question. For all other fermions this is the famous "Higgs Mechanism", where $\alpha \propto \lambda$ is a measure of how strongly the particle couples to the Higgs which correlates with the particle's mass.

For all fermions, we have to take into account one more phenomenon, namely handedness, which is a measure of how the intrinsic spin of a particle lines up with the direction of travel. The two terms that we used to describe this handedness are called chirality and helicity (also known as apparent chirality). When neutrinos travel at very near the speed of light, the two are almost identical for our purposes[11]. If the intrinsic spin lines up with the momentum vector we say that that particle exhibits a "right-handedness" and "left-handedness" if the spin and momentum are anti-aligned. We can therefore decompose the Ψ into a left and right handed component, labeled ψ_L and ψ_R respectively and represent interactions that favor one handedness or the other. We can rewrite Equation 5.6 where the $\psi_L\bar{\psi_L}$ terms go to zero due to orthonormality.

$$\mathcal{L} = \alpha(\bar{\psi_L}\psi_R + \bar{\psi_R}\psi_L) + \text{other terms} \tag{5.7}$$

From the Goldhaber experiment [139], which determined the neutrino helicity by determining the helicity of the emitted γ from the electron capture of Eu^{152} [12], we know that the neutrino overwhelmingly favors only left handed interactions. This implies that Ψ_R either does not exist or do not interact with any of the three standard neutrino flavors found in the standard This means that there is no term in the original Langranian that would account for neutrino masses. While it is possible for Ψ_R to be

[11] Helicity comes into play if you can switch into a reference frame where the apparent direction of travel of the observed particle is reserved, aka moving faster than the particle

[12] I am not doing this experiment justice, for a nice overview please see [140]

non-zero, it would have to describe a right-handed neutrino-like particle that interacts even less frequently than its left handed cousin.

The search for this right-handed neutrino-like particle has been an active area of research for many years see [141]. The challenge therefore is to define a field such that it only has a left handed component yet still allows for a $\Psi_L\bar{\Psi}_L$ term to "create" a mass term. Starting this time from the Dirac Lagrangian:

$$\mathcal{L} = \bar{\Psi}(i\gamma^\mu\partial_\mu - m)\Psi \tag{5.8}$$

Spiting the Ψ into its left and right handed components and after some Feymann algebra that takes advantage of the properties of the γ matrices as well as the derivatives you can create a series of coupled equations:

$$\begin{aligned} i\gamma^\mu\partial_\mu\psi_L &= m\psi_R \\ i\gamma^\mu\partial_\mu\psi_R &= m\psi_L \end{aligned} \tag{5.9}$$

It is interesting to note is that if you let the mass go zero you can recover the Weyl equations, which describe wave propagation for massless fermions. Now we want to try and see if there is some formulation where we can write the right handed component in terms of the left handed component and vise versa. Taking the hermitian conjugate of the second equation, followed some more algebra followed by taking the transpose of everything with some more algebra results in the following equation:

$$-i\gamma^{\mu T}\partial_\mu\bar{\psi}_R^T = m\bar{\psi}_L^T \tag{5.10}$$

Writing this now in terms of the charge conjugation operator (C) with $C\gamma^{\mu T} = -\gamma^\mu C$, which normally take a particle and turns it into its anti-particle we recover an equation of the form:

$$i\gamma^\mu\partial_\mu C\bar{\psi}_R^T = mC\bar{\psi}_L^T \tag{5.11}$$

which by comparison looks like first equation in Equation 5.9 only now with the substitution $\psi_R = C\bar{\psi_L}^T \equiv \psi_L^C$, which we call the charge conjugate field. This charge

conjugate field now has some interesting properties namely that:

$$\Psi^C = (\psi_L + \psi_R)^C = (\psi_R + \psi_L) = \Psi \quad [13]$$

So this new field and its associated particle are equivalent to its anti-field/particle, which is a property that can only hold true for neutrinos, as all other fermions have very distinct anti-particles. Rewriting Equation 5.7 with this new definition you now end up with a mass term written written as:

$$\mathcal{L} = \frac{1}{2} m_{Majorana} \bar{\psi}_L \psi_L^C + \frac{1}{2} m_{Majorana} \bar{\psi}_R \psi_R^C \tag{5.12}$$

This property ($\nu = \bar{\nu}$) is the defining characteristic of Majorana fermions.

In order to now account for why the neutrino mass is so much smaller than all the other fermions found in the Standard Model, we look to the "See-Saw" mechanism. These models support Majorana and Dirac mass terms, but with the right handed components represented through the addition of N very heavy neutrinos along with the 3 light mass states observed in oscillation experiments so far. In the Type 1 See-Saw, these additional heavy N neutrinos act as an alternate solution to your Lagrangian, but now the constant in front of the lighter observed neutrino flavors mass terms includes a term of $\frac{1}{M_N}$, where you can make M_N as large as you need. In essence, it means that normally the neutrinos should have masses comparable to the other fermions in the standard model, but through the inclusion of these additional N heavy right-handed neutrinos you suppress the lighter neutrino masses by this additional neutrino mass term. In these models it is still an open question if there N=1,2,3+ heavy right-handed neutrinos, but their effect is always the same. It is important to remember that these heavy neutrino partners have yet to be observed, but act as a mechanism to explain the relative smallness of the observed neutrino masses.

[13] This is actually one of the very few times where you can treat an operator linearly in particle physics

Isotope	$2\nu\beta\beta$ Half Life (years)	Method	Citation/Notes
^{48}Ca	$4.4^{+0.6}_{-0.5} \times 10^{19}$	Averaged	[142]
^{76}Ge	$1.65^{+0.14}_{-0.12} \times 10^{21}$	Averaged	[142]
^{128}Te	$2.0 \pm 0.3 \times 10^{24}$	Averaged	[142]
^{130}Te	$8.2 \pm 0.2(\text{stat.}) \pm 0.6(\text{syst.}) \times 10^{20}$	Direct	[144] - from CUORE experiment
^{96}Zr	$3.9 \pm 0.9 \times 10^{19}$	Geochemical	[145]- based on a 5.39 gram Zr sample
^{96}Zr	$2.35 \pm 0.14(\text{stat.}) \pm 0.16(\text{syst.}) \times 10^{19}$	Direct	[146] - from NEMO-3 experiment

Table 5.1: Table summarizing some of the current measurements of $2\nu\beta\beta$ in selected isotopes, for a full list see Table 2 in [142]. Note the large error bars (and disagreement) between the direct and geochemical measurements of the half-lives of Zr-96

5.3.2 Current Experimental Status

The first experimental evidence for $2\nu\beta\beta$ decays started appearing in the mid-1980's [134] looking for signals of this process via one of three methods radiochemical, geological and direct measurements (current status summarized in [142]). Geo/radiochemical measurements seek to pick out traces of accumulation of $2\nu\beta\beta$ daughter nuclei from large mineral deposits of the parent isotopes. While this method provided some of the earliest evidence for $2\nu\beta\beta$ in Tellurium, Selenium and Uranium, geochemical measurements in particular have large systematic uncertainties associated with their measurements and provide no information regarding the $2\nu\beta\beta$ spectrum, these methods only provide a limit on the half-life [143]. The vast majority of $2\nu\beta\beta$ searches utilize a direct search method attempting to map out the full $2\nu\beta\beta$ spectral shape. The status of the current measurements are summarized in Table 5.1

As of the writing of this thesis, no definitive measure of $0\nu\beta\beta$ has been reported by any experiment. All experiments currently looking for $0\nu\beta\beta$ can only report upper limits on the rate they see for $0\nu\beta\beta$. Currently the most stringent limits on the the $0\nu\beta\beta$ half-life in terms of the raw half life come from CUORE ($T^{0\nu\beta\beta}_{\frac{1}{2}} > 9.5 \times 10^{25}$ year - projected 5 year sensitivity) and from the Kamland-Zen experiment ($T^{0\nu\beta\beta}_{\frac{1}{2}} > 1.1 \times 10^{26}$ years) [147]. However; how does one then go from a half-life rate limit to

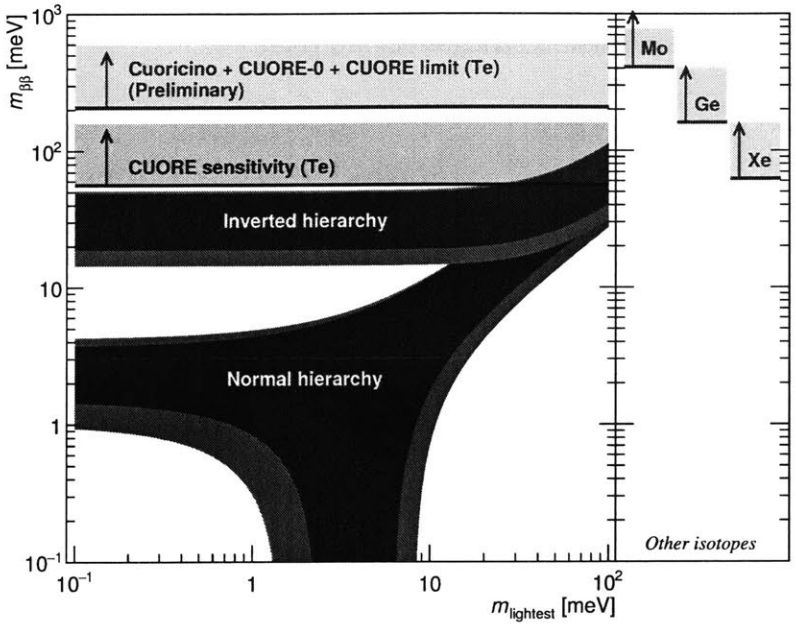

Figure 5-4: Figure of merit for $0\nu\beta\beta$ experiments. $0\nu\beta\beta$ can occur in either the green (inverted hierarchy) or red (normal hierarchy) regions of this parameter space. Experiments, such as CUORE, can only place a limit on the half-life of $0\nu\beta\beta$ and then exclude the regions of parameter space above the limit lines shown here. The limits from other experiments that measure $0\nu\beta\beta$ in other isotopes are included for completeness

neutrino mass?

5.4 Introduction to Nuclear Modeling

All $0\nu\beta\beta/2\nu\beta\beta$ experiments can only measure the half-life/decay rate of $0\nu\beta\beta$or $2\nu\beta\beta$, and it is up to the background theory to take into account all the nuclear physics that occurs within the nucleus and convert the half-life into a physics result. For $2\nu\beta\beta$ reactions the relation is straightforward [148]:

$$[T^{2\nu}_{\frac{1}{2}}]^{-1} = G(Q,Z)^{(0)}_{2\nu}|M_{2\nu}|^2 \tag{5.13}$$

where:

- $T^{2\nu}$:This is the measured half-life of the reaction, provided from each experiment taking into account all the various backgrounds present in each experiment. For a full review of all the current half-life measurements as of the writing of this thesis [149]

- $G(Q,Z)^{(0)}_{2\nu}$: This is the phase space parameter for $2\nu\beta\beta$ and describes the phase space available for $2\nu\beta\beta$ to occur within a specific isotope. The key difficultly in the determination of this phase space parameter comes in the form calculating the electron wave functions before and after the $2\nu\beta\beta$ decay as well correctly accounting for various corrections. Many methods have come about to calculate these wave functions [150], steadily reaching higher and higher precision as computational power has increased with the errors associated with these calculations broadly landing at around $\lessapprox 1$ percent for any $2\nu\beta\beta$ reaction.

- $M_{2\nu}$: This is the nuclear matrix element that contains all the nuclear physics that is occurring inside the nucleus during $2\nu\beta\beta$ decay. As nuclei represent extremely complex systems with multiple interactions occurring within the nucleus simultaneous, these calculations requires approximations which have to be

tested and verified. For $2\nu\beta\beta$, the verification is provided by direct measurements of $2\nu\beta\beta$ provided by experiments such as CUORE or Kamland, which means that the errors associated with these nuclear matrix elements have decreased dramatically in recent years as more experimental data comes in. Important to note is the fact that you can not compare one to one the matrix elements used in $2\nu\beta\beta$ and $0\nu\beta\beta$ calculations, which we will discuss in much more detail shortly.

For $0\nu\beta\beta$ decays, equation 5.13, now has to be modified to account for the additional interactions that are now possible within the $0\nu\beta\beta$ framework. Specifically we will follow the parameterization given in [151]:

$$[T_{\frac{1}{2}}^{0\nu}]^{-1} = G(Q,Z)_{0\nu}^{(0)} |M_{0\nu}^{Light} \frac{m_{\beta\beta}}{m_e} + M_{0\nu}^{Heavy} \frac{m_p}{M_{\beta\beta}}|^2 \tag{5.14}$$

G is still a phase space factor calculated as before, but we split the nuclear physics contributions into two classes, the light and the heavy corresponding to the moderator particle involved in the $0\nu\beta\beta$ reaction. If the moderator particle behaves like a Majorana light neutrino discussed previously, whose mass can be parameterized via the known neutrino mass states m_i and the well measured PMNS neutrino mixing matrix(see section 5.2.1), U, [123][124]then:

$$m_{\beta\beta} \equiv |\sum_i U_{ei}^2 m_i|$$

There are alternate theories that would allow for $0\nu\beta\beta$ using a heavy Majorana neutrino as a moderator which were discussed in the Type 1 See-Saw model section. In a similar vein to the light neutrinos models, we can write down an effective mass term now summing over the m_j mass states corresponding to these heavier right-handed neutrinos:

$$[M_{\beta\beta}]^{-1} \equiv \sum_j \frac{U_{ei}^2}{m_j}$$

The observation of $0\nu\beta\beta$ would help narrow down which one of these two regimes dominate the physics of $0\nu\beta\beta$, but within the literature the contribution from the

heavier Majorana neutrino theories are ignored. This stems from the fact that within the momentum transfer, q , that is occurs within a nucleus tends to be of order 100 MeV (generated from the approximate size of the nucleus $\approx$ 2 fm) which is one way to gauge the energy available to a reaction. As current heavy neutrino models predict masses $\gg$ 100 MeV, this does not leave a lot of available phase for these reactions to occur. On the other hand light neutrino masses $\ll$ 100 MeV, open up large areas of phase space which makes these models more attractive in the short term. This is also the simplest model out there as it does not require additional particles to be added to the standard model or any complex mechanisms to generate the neutrino mass. Only a definitive measurement of $0\nu\beta\beta$ would determine which one of the two models dominates, but due to the simplicity of the light neutrino models, in literature the half-life is often written out as:

$$[T^{0\nu}_{\frac{1}{2}}]^{-1} = G^{(0)}_{0\nu}|M_{0\nu}|^2 \frac{\langle m_{\beta\beta}\rangle^2}{m_e^2} \tag{5.15}$$

This equation states is that if we were to see a $0\nu\beta\beta$ signal, we could convert that half-life into a additional measurement of the effective Majorana mass of the neutrino $m_{\beta\beta}$. What would the measurement of $m_{\beta\beta}$ mean for the field of neutrino physics as a whole?

5.4.1 Implications on measuring $m_{\beta\beta}$

It is important to remember that throughout this discussion, we can only take the experimentally measured half-live as a given, any inferences from that stem from that value are highly model dependent and will heavily depend on specific details of the detection. If in the future, we were to record a half-life for $0\nu\beta\beta$ in an experiment we could then deduce the following from that result:

1. We would have confirmation that the neutrino is a Majorana particle, which then opens up specific mechanisms by which the neutrino can get its mass, discussed in the theory section of this thesis. In the event of a $0\nu\beta\beta$ measurement this is the only statement that we can say for sure and is not affected by any of

the subsequent deductions.

2. From there we would still need to accurately measure the nuclear matrix elements, $M_{0\nu}$, reducing the error bars on these calculations. However; these calculations are still sensitive to the value of g_A/λ. From there we could then calculate a value for $m_{\beta\beta}$, which would represent the key equation for the determination of the neutrino masses given that the neutrino is a Majorana particle.

3. From other measurement discussed in previous sections were then to also generate a value $m_{lightest}$ for the neutrino sector we could then zero in on a specific point on the phase space diagram for $0\nu\beta\beta$ decays - see Figure 5-5

4. If these two measurements were to lie in one of the allowed regions of $0\nu\beta\beta$ phase space, we would have effectively measured the mass of the neutrino and derived the mechanism by which neutrinos obtain their mass. However; if the combined $m_{lightest}$ and $m_{\beta\beta}$ point ends up lying outside of the allowed inverted or normal allowed phase space, this now opens up the possibility of additional corrections the equations that govern the neutrino mass. We could then test the validity of the specific assumptions made in steps 2-4, such as only including the light neutrino masses in Equation 5.15

5.5 Nuclear Matrix Element Calculation, $M_{0\nu}$

The general procedure of calculating the probability of any reaction in particle physics involves finding the "overlap" between the initial and final states of the reaction you wish to describe where your final state has been modified from your initial state through various potentials. This probability is encoded into the term called the $0\nu\beta\beta$ nuclear matrix element, $M_{0\nu}$ or NME, which also serves as the constant of proportionality between a half life measurement and the Majorana mass term, as seen in equation 5.15. There are multiple ways of writing out this terms, but here we

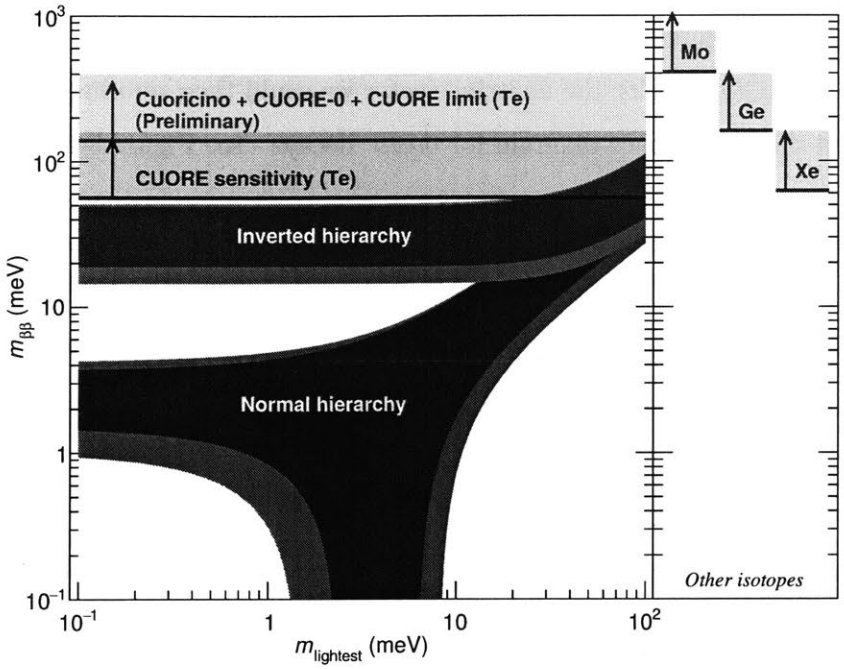

Figure 5-5: The available phase space for $0\nu\beta\beta$ searches. Mass measurements from direct measurements, such as KATRIN will set limits on this phase space with horizontal lines. Cosmological measurements of the neutrino mass will also set vertical line limits, but the values are highly model dependent and come with their own fair share of caveats

will stick to the following two paramcterizations:

$$M_{0\nu} \equiv \sum_{n,n'} \langle \psi_i(n_i, n_i') | \tau_n^\dagger \tau_{n'}^\dagger H_{nn'}(q) | \psi_f(n_f, n_f') \rangle \text{ alternatively}$$
$$\sum_{n,n'} \langle \psi_i(n_i, n_i') | \tau_n^\dagger \tau_{n'}^\dagger | \psi_f(n_f, n_f') \rangle \times \langle n_i, n_i' | H_{nn'}(q) | n_f, n_f' \rangle \tag{5.16}$$

with n_i and n_f being the respective initial and final nuclear spin states of the the nucleons involved in the $0\nu\beta\beta$ reaction. The best way to think about these calculations to think backgrounds, starting from the pair of nucleons that "finished" the $0\nu\beta\beta$ reaction. We need to then look at the probability that any other pair of nucleons could decay into that final pair (second term) followed by looking at the probability that you pick a pair of nucleons inside the nucleus that actually interact (first term). You finally sum over all the various possible final state nucleon pairs that could take part in your reaction. When discussing the nuclear matrix elements in literature the nuclear matrix element often gets split up into three components, the Gammow-Teller(GT), the Fermi (F) and the Tensor (T) terms as shown in Equation 5.17.

$$M_{0\nu} = M_{0\nu}^{GT} - \frac{g_V^2}{g_A^2} M_{0\nu}^F + M_{0\nu}^T \text{ with:}$$
$$\lambda \equiv \frac{g_V}{g_A} \tag{5.17}$$

The relative strength of each of these terms depends on the exact transitions dynamics, but for transitions down to the $J^P = 0^+$ states found at the end of many $0\nu\beta\beta$ decay paths, the GT and F term dominate, with the tensor term being smaller by a factor of ≈ 10. The GT and F contributions tend to be within a factor of 2 of each other, but there is an additional factor of $\frac{g_V^2}{g_A^2}$ in front of the Fermi contribution. If we now factor out the λ contribution the relationship between a measured half-life and $m_{\beta\beta}$ now looks like:

$$[T_{\frac{1}{2}}^{0\nu}]^{-1} = G_{0\nu}^{(0)} g_A^4 |M_{0\nu}|^2 \frac{\langle m_{\beta\beta} \rangle^2}{m_e^2} \text{ with:}$$
$$M_{0\nu}' = \lambda M_{0\nu} \tag{5.18}$$

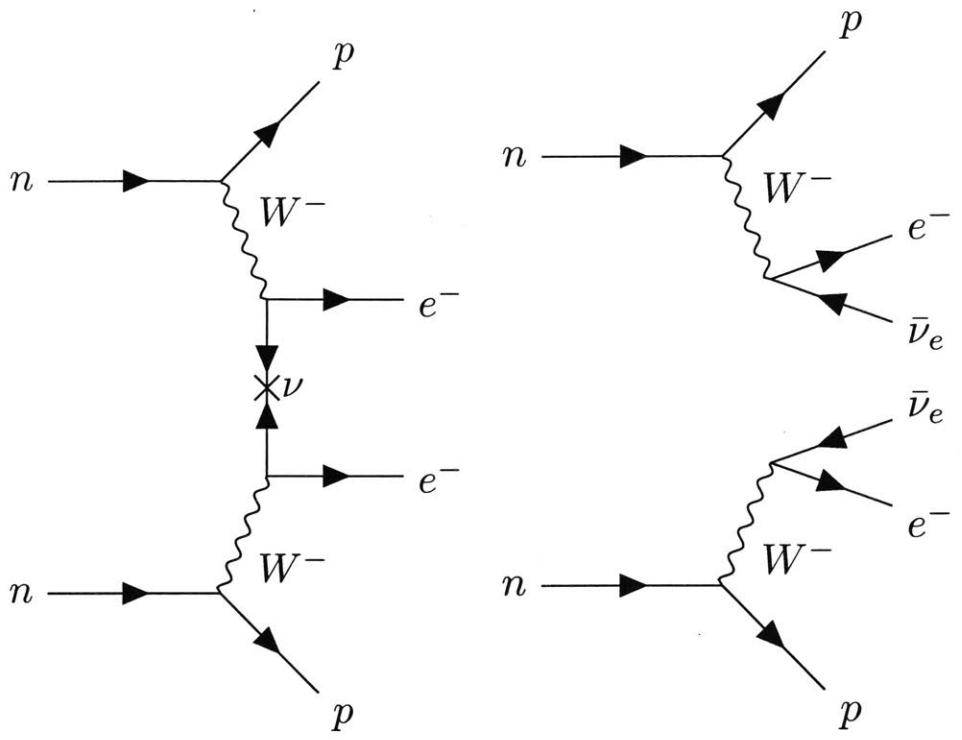

Figure 5-6: Feymann diagrams for neutrino-less (a) and two neutrino (b) double β decay. Important to note here is that the $0\nu\beta\beta$ decay diagram allows for direct momentum transfer between nucleons, thus opening up additional intermediate nuclear states

In this form it becomes apparent that λ now represents another parameter needed to to convert between the measured half-life and $m_{\beta\beta}$ For all calculations up to now, λ has been assumed to follow the same value as measured in free neutron decay (1.2723), however; additional theoretical calculations have begun exploring the possibility of this value getting quenched in more complex bound states such as nuclei [152][153]. This $\lambda \equiv \frac{g_V}{g_A}$ is the nuclear quenching factor that we seek to measure with the $LiInSe_2$ crystal.

5.5.1 Nuclear Matrix Element Calculation methods

In nuclear physics the calculation of the NMEs represents a particularly difficult problem as you have the possibility of interactions between many different nucleons within the nucleus which increases the number of nucleon combinations that have

to be taken into account and thus increases the computational complexity involved. At the same time the nuclear potentials that govern these decays are quite complex and require various approximations in order to bring the calculations to a reasonable level. In general, though, the process for the calculation of nuclear matrix elements involves a three step process:

1. Grouping the nucleons in the initial nuclear states in advantageous ways and determining a Hamiltonian, H, that describes interaction between these various groupings of particles

2. Calculating the intermediate states in terms of energy and their corresponding density of states that play a role in the decay process within the energy budget allotted to you by your reaction - see Figure 5-7.

3. Finding the probability that particle/groups of particles then decay out of the intermediate states into the final nuclear state and with what energies they "arrive" at the final nuclear state of $0\nu\beta\beta$decay. This is often reflected by assigning relative weights to each of the energy levels calculated in Step 2 - see Figure 5-8

These calculations represent an active area of research within the theoretical nuclear physics community. In $2\nu\beta\beta$, these calculations tend to be more straightforward as the momentum transfer, q, that is available to the nucleons in this reaction tends to be smaller, which means less intermediate stages can play a role in the final transition probability - see Figure 5-6. For $0\nu\beta\beta$, more intermediate states can play a role, including the highly forbidden[14] states -see Figure 5-7.

For $0\nu\beta\beta$ NMEs, the lack of a confirmed signal represents another problem for theorists. As you move to more highly forbidden states, the approximations that are used to reduce the calculation times, may begin break down. Without a signal confirmation, though, it becomes increasingly difficult to ascertain which approximations

[14]Forbidden-ness is a measure of the angular momentum (and parity) change between two states, the larger the change that has to be overcome, the less likely the transition $\Longrightarrow$ longer half-life

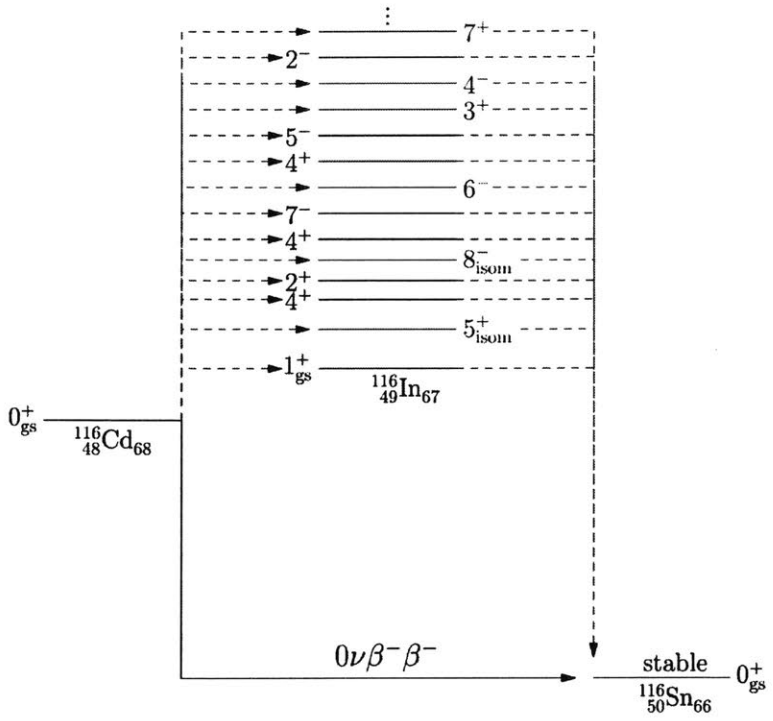

Figure 5-7: Diagram showcasing the intermediate nuclear states that play a role in the Nuclear Matrix Element calculation for Cd-116. $2\nu\beta\beta$calculations only need to deal with the $J^\pi = 1^{+-}$ states, while the $0\nu\beta\beta$calculations must taken into account all the higher order forbidden states that are assessable to it. Taken from [153]

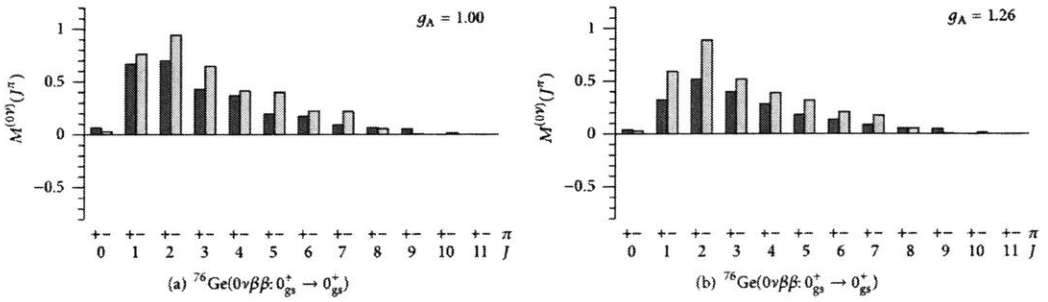

Figure 5-8: The relative weights of the various intermediate states that contribute to the final Nuclear Matrix Element (NME) value for Ge-76. Taken from [154]

are value and which are not. This combination of uncertainties leads to the confused state of the field shown in Figure 5-9

There has been tremendous progress in recent years to reduce these error bars, but without a definitive measurement of $0\nu\beta\beta$ it will difficult to know for sure what models/approximations work best. There is another set of measurements that could be undertaken, namely looking at single-β highly forbidden decays, which can stand in as a proxy for the intermediate states that play a role in $0\nu\beta\beta$ decays. The various methods used to calculate these rates are named after the various approximations that they implement. In this thesis we will discuss the following methods for determining the nuclear matrix elements.

- Shell model: This is the oldest method of calculating the Nuclear Matrix Element. The most fundamental version of this model is to calculate all the energy levels in a nucleus by treating all the nucleons as independent particles in a harmonic oscillator potential. Initially limited to calculations for light nuclei up to approximately N =50; This method was most limited by the sheer computational power needed to calculate the contribution of each shell and the interaction strength between all the various combinations of in the nuclear model. This method also has the trade off of summing over a larger number of possible energy state configurations at the cost of only summing over the first few energy states. Work in recent years has improved this model, allowing for its use in heavier elements by varying the number of particles that are allowed to jump between p/f subshells [156]. In many respects this is the nuclear model that is used as a baseline for other models, as this methods makes the least assumptions regarding the physics involved inside the nucleus.

- IBFM/IBM (Interacting Boson-Fermion Model/Interacting Boson Model): First proposed in 1975 [157], these method builds upon the shell model, by noticing that the majority the lowest energy states in nuclei are predominantly populated by spin $\updownarrow$ nucleon pairs. By pairing up nucleons into independent particles of spin 0, 2 or 4, one can drastically reduce the calculations needed to

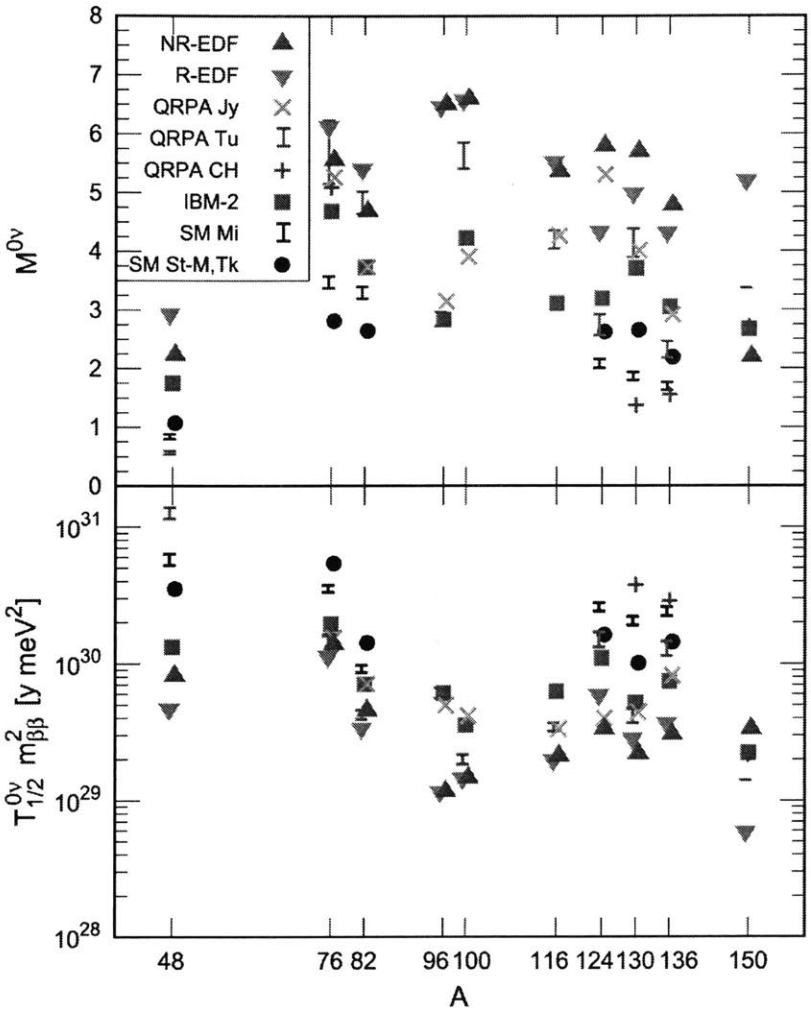

Figure 5-9: Overview of all the various Nuclear Matrix Elements calculations and their respective error bars (top graph). Using those nuclear matrix elements, one can then calculate the relative error bars on the half-life limits on the current set of experiments. Taken from [155]

model a nucleus. More advanced techniques for This method has achieved success calculating the nuclear energy levels present in nuclei up to about N=120 and in particular for calculating the spectra of even-even nuclei [158]. Additional refinements to this method comes in the form of creating additional paired particle interactions between the bosons and another individual nucleon (Interacting Boson-Fermion Model) or additional pair of nucleons (Interacting Boson-Fermion-Ferimon Model).

- MQPM (Microscopic Quasiparticle-Phonon Model): So far all the methods we have discussed so far perform at their best describing even-even nuclei since divide up the interactions between various particle pairs as pair-wise interactions. The Microscopic Quasiparticle-Phonon Model, treats the nucleon as a lattice and akin to superconducting Cooper Pairs, the nucleons form pairs which are then treated as quasi-particles. Instead of then pairing this quasi-particle up with another quasi-particle, the quasiparticle now gets paired up with one of the collective phonon excitations of this nuclear lattice. This now makes up a three particle system which more easily divides up the odd-odd nuclei. For fuller details on how this model is constructed/its effective range of nuclei this model can be applied to see [64][159].

- pnQRPA or QRPA (proton-neutron Quasiparticle Random-Phase Approximation). One of the older methods of calculating the nuclear matrix elements, it comes from a generalization of the ordinary Random Phase Approximation. This is a "tall" method for calculating the NMEs, namely is sums over a wider range of energy levels (including higher states in Figure 5-7), but at the cost of more coarsely approximating total number of possible nuclear state configurations. In addition this method has the downside that it has a strong sensitivity on a g_{pp}, which parameterizes the strength of the correlation between the various nucleons inside the nucleus. The method begins to break down for extremely large values of g_{pp} at which point the nuclear models become unphysical as they treat all the nucleons inside the nucleus as pairs of deuterons [155]. QRPA can

handle much larger model spaces than the shell model, but at the cost of only considering pair-wise [15] correlations between nucleon pairs [63]

5.6 $LiInSe_2$ Setup

5.6.1 $LiInSe_2$ Theory Background

Ever since its proposal, single β decay has been extensively studied, characterized and tested in the literature. Single β decay and its underlying structure still remains an active area of the nuclear theory research in order to better understand the role of the weak force in these decays. Up until now all the properties of most beta spectrum have been determined using leading order calculations, but for highly forbidden decays, such as the one in In-115, the additional terms are needed to fully describe the shape. The full theory of why how these additional terms play a role in the deformation of the spectral shape are covered in [160] [154] [161] and beyond the scope of this thesis. For our purposes, thanks to our collaborators in Finland [154], we obtained a library of various In-115 spectra that had been calculated using three of the methods described in the previous section, Shell, IBM and MQPM and over a range of effective g_A[16] values. The effect of changing this g_A parameter is summarized in Figure 5-10. The main item to notice here is the fact that the biggest change in the spectral shapes happens at the lowest energies, which means the lower the energy threshold we can achieve, the better the sensitivity to g_A we we ill have. This make cyrogenic bolometers the perfect candidate for the investigation of g_A. Note that up until this point the highest resolution beta spectrum for In-115 had been measured in 1979 [162].

[15] pair-wise here means that you group the nucleons inside your nucleus up as pairs of either particle or holes and then consider only the correlations between nucleons

[16] technically all these spectra vary as a function of both the axial (g_A) and vector (g_A) coupling constants, but the (g_V) value is often normalized out to 1

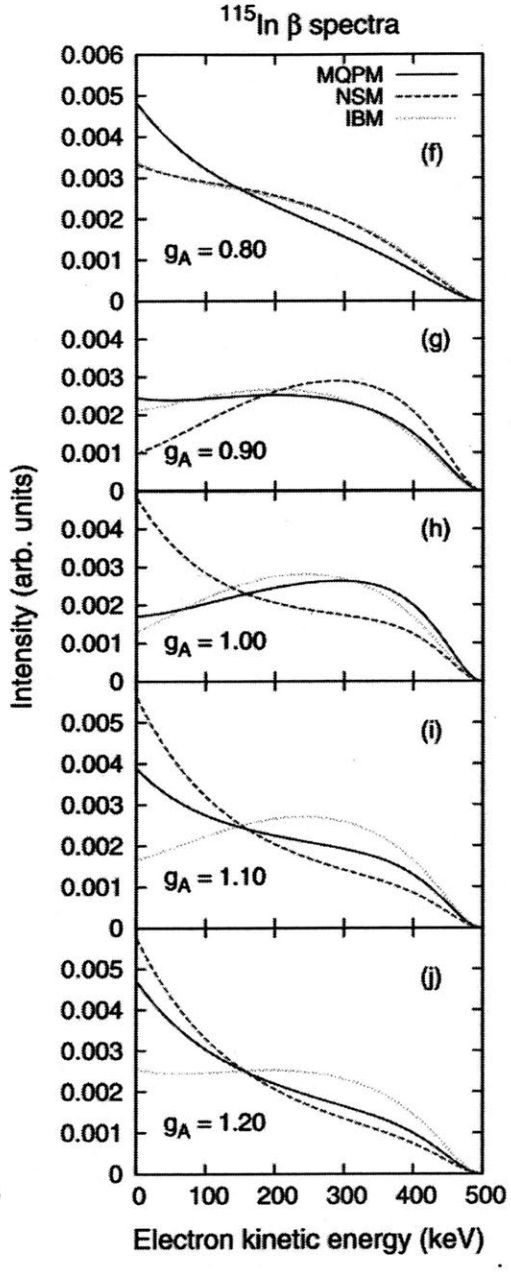

Figure 5-10: The shape of the In-115 spectrum as a function of g_A taken from [154]

5.7 Growing the $LiInSe_2$ Crystal

Due to the worldwide shortage of $^3_2$Hecoupled with the increased demand for thermal neutron detectors for national security applications has prompted many companies, such as our collaborator Radiation Monitoring Devices (RMD) in Watertown, MA, that specialize in radiation detectors to look into using semiconductor neutron detectors. Similar to $^3_2$He, the low Z offered by Lithium allows for a large cross section for thermal neutrons coupled with a large signal (Q-value: 4.8 MeV) makes inclusion of Lithium in these crystals an attractive possibility. These detector compounds fall broadly into the category of $LiMX_2$ where M is either In or Ga while X can be S, Se or Te. The art of crystal growth is a bit like black magic, everyone who performs it closely guards their secrets and often times the process can rely heavily on pure chance. The timescales for growing these crystal can easily be close to weeks requiring large amounts of patience and nerves of steel... The whole process started with ultra pure Se, In and Li[17], which particular care taken to make sure that the Lithium did not react with any other elements during the crystal growth process. Once the elements were loaded into a non-reactive crucible and melted a crystal was extracted via the vertical Bridgeman technique [163], wherein you create a melt of your crystal in the top part of the crucible. You then create a gradient of temperature differences with the lower temperatures being at the bottom of the crucible and slowly (very slowly)move the crucible so that phase boundary between the liquid and crystal phases eventually passes through the entire crucible. Once the crystal formed you can then proceed to cut the resulting boule into the pieces that you need for your detector crystal. The final result for our 10.3 gram $LiInSe_2$ detector, (shown in Figure 5-11) that we used is a bright red crystal[18] which we then proceeded to install in the Centre de Sciences Nucléaires et de Sciences de la Matière (CSNSM) in Orsay, France (near Paris). It is important to remember that the source that we wish to examine is the single β decay spectrum of In-115, which makes LIS crystal, both the

[17]The lithium metal used in our crystal has been enriched to 95 percent Li-6, which has the highest neutron capture cross section

[18]which we nicked named the jolly rancher

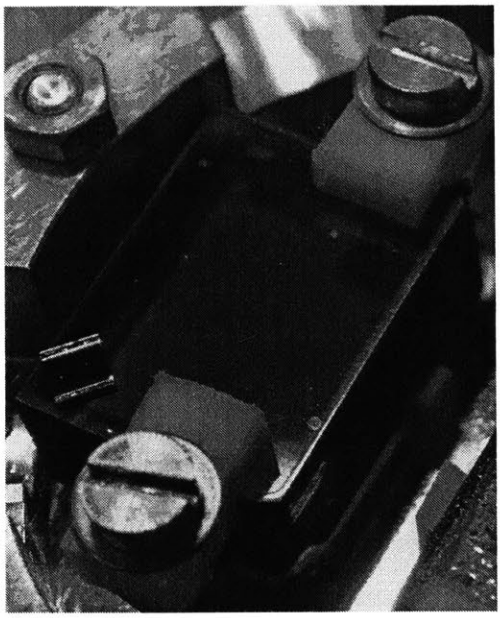

Figure 5-11: The jolly rancher $LiInSe_2$ crystal, interestingly the color of the crystal depends on the Lithium concentration present in the crystal, with red indicating a deficiency. If all available lattice spots were occupied by Lithium, the resulting color of the crystal would be closer to a yellow-green

readout mechanism and the source.

5.8 LIS Data Taking

The basic data taking setup is illustrated in Figure 5-12, with the $LiInSe_2$ crystal in the place of the absorber and included a thin semiconductor light detector used for light collection. The light detector was operated as a Luke-Neganov detector (for more details on how that works see section 3.5)to collect scintillation produced in the $LiInSe_2$ detector. By collecting the scintillation light produced by the $LiInSe_2$ crystal we would be able to calculate an event-by-event yield for every event in the detector, which would aid in rejecting background signals - discussed more in section 2 This second light detector also had the added benefit of producing faster readouts due to its smaller mass. This would then aid us during the determination of the pile-up events in our detector, created by the longer tails of the signal events in the $LiInSe_2$ crystal.

The $LiInSe_2$ crystal data was taken over two distinct periods, November 2016

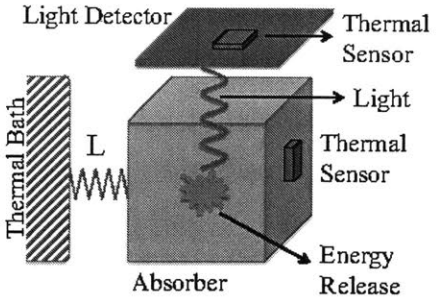

Figure 5-12: Detector readout was performed using an Neutron Transmutation Doped (NTD- discussed in the introduction to bolometers chapter) chip glued onto the $LiInSe_2$ and light detector respectively.

and then again over October/November 2017 at the CSNSM. During these runs there was an additional detector crystal installed right next to the $LiInSe_2$ crystal, which allowed us to monitoring the background sources present in our setup. In the 2017 run, this second crystal was a LMO crystal that had been used for detector R&D studies for next generation CUORE studies, under the CUPID umbrella. While the light detector performance was better, operating at a higher voltage, during the November 2016 run, the lessons learned during that first run allowed us to design additional studies to better characterize the $LiInSe_2$ crystal run, presented here. For the November 2017 data, the total raw exposure times for the background and the barium dataset was and 29 hours and 34 minutes (leading to a total exposure of ≈ 12.7 gram·days of exposure). For more details on the hardware setup, I refer the reader to the results published in [164], whose setup very closely mirrored the setup discussed in this thesis. For the remainder of this chapter we will refer to the crystal by the following acronyms $LiInSe_2$(LIS)[19], Light Detector (LD) and the $LiMoO_4$ (LMO).

5.9 LIS Analysis

The analysis procedure used for the LIS analysis presented here closely follows the outline of the CUORE low energy analysis [165], which was used to push down the

[19]In our discussions we would often refer to this entire project as Linsey, asking, "Hows Linsey" much to the confusion of any visitors

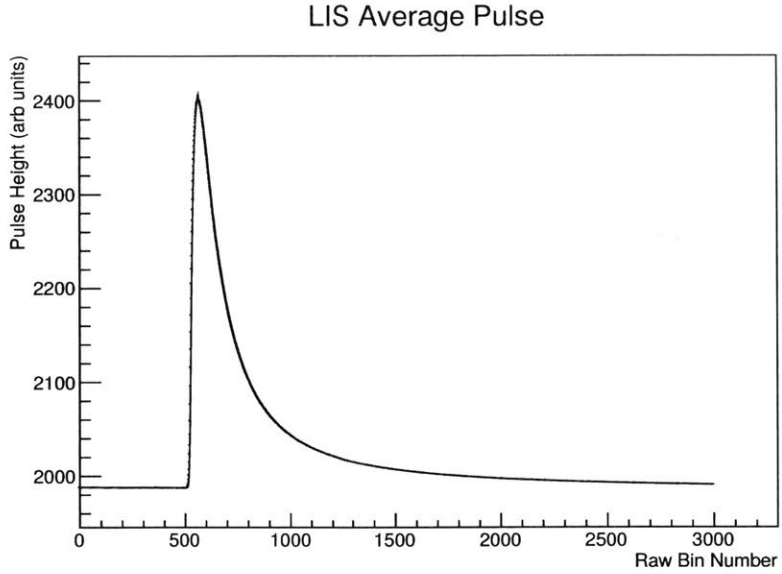

Figure 5-13: The average pulse used in the LIS analysis, drawn from the barium datasets due to their higher event statistics. Note the longer signal pulse times compared to similar heat-only pulses from CDMS

effective threshold of the CUORE detectors to look for WIMP Dark Matter. However; there is one particular difference from the CUORE analysis chain that should be brought up/discussed, namely the readout frequency used in this analysis is 5 kHz, faster than the standard CUORE 1 kHz readout rate. This faster readout used in this analysis particular will come in handy when looking at the pileup effects via pulse shape discrimination. In order to bring down the analysis threshold of the CUORE detectors, the CUORE collaboration implemented a optimal trigger [166][167] similar to the one discussed in the CDMS chapter (section 3.5.1). The first step once the data had been converted into a CUORE readable format was to generate an average pulse from the derivative trigger[20] pulse data, which was done using a 50 σ noise cut, of which all the passed pulses were then averaged together to create the pulse shown in Figure 5-13 This average pulse acts as an ideal pulse template, which we can then scale up or down in energy in order to compare a triggered event to the ideal and from that generate series of pulse quality parameters. It should also be noted that one of

[20]Here derivative trigger means a minimum voltage signal level in order for the signal to register, similar to how you would set the trigger on an oscilloscope

the features of the CUORE analysis tools is that the it is a "streaming" data tool, which means that it takes a continuous data-stream and simply notes the timestamps that correspond to an event. From Figure 5-13 we can also note several pulse features that we will reference throughout the text.

- *Baseline*: In this analysis we defined the baseline as the first 100 ms of the pulse before the trigger flag was issued. Using these samples one can then define additional quantities such as the

- (*OF*) *Decay Time*: For pulses identified via the Optimal Filter (OF), the decay time is defined by the time it takes for the pulse to go from 90 to 30 percent of the maximum amplitude (this is approximately $1/e$)

- (*OF*) *Rise Time*: This is defined by the time it takes it takes the pulse to go from 10 to 90 percent of maximum amplitude (approximately $1/e^2$)

- (*OF*) *Delay Time*: The optimal filter will reconstruct a pulse based on the filtering performed on the FFT component of the spectrum, however; this reconstructed pulse can sometimes end up shifted slightly in time-space. This variable tracks the time at which the reconstructed pulse is triggered. For most events the reconstructed pulse will end up reconstructing with a similar baseline (100 ms) as the original triggered pulse. At the very lowest energies these pulses will reconstruct poorly due to the inability to discriminate between statistical fluctuations in the noise and the actual pulse.

- $OF\chi^2$: In this instance, $OF\chi^2$ is a measure of how closely the reconstructed pulse matches the optimal filter template and proved to be one of the most effective cuts applied in this analysis - see

5.9.1 Calibration Procedure

Once the data had been read in the first step was to calibrate our detector response as a function of energy on both the LMO and LIS crystals simultaneously (due to the smaller size and high energy of the Barium sources the LD detector was not calibrated

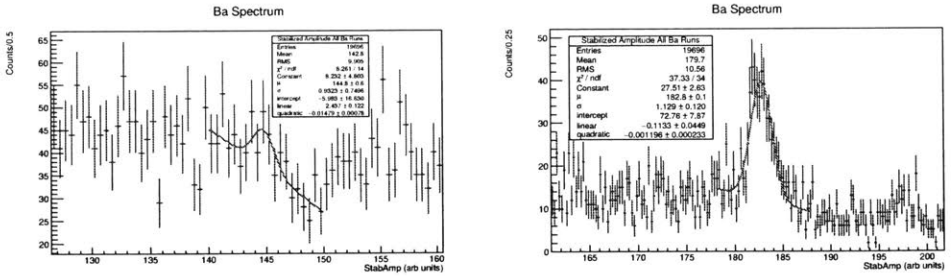

(a) LIS 276 keV Barium Peak (b) LIS 356 keV Barium Peak

Figure 5-14: Example fits to the Barium data, note that particular for the 276 keV peak, the fitter has a difficult time fitting the peak due to the low statistics and the low peak to background rate.

this way) Inbetween our background data taking, we inserted a barium calibration source as close as possible to the detector crystals, via a fishing line that was lowered between the outer cryostat wall and the inner lead shield wall. Barium is a γ emitter that is commonly used as a calibration source in nuclear/particle physics with the most commonly used γ peaks at 276.40, 302.85, 356.02,383.85 keV. Due to the fact that the LIS crystal would generate its own intrinsic background that the Barium data would overlap special care would have to be taken to reduce pile-ups between these event populations as well as approximating the In-115 decay spectrum (locally) around the region of each γ peak. The model used to fit each peak was a combination of a standard Gaussian with parameters μ and σ for the peak region added together with a second degree polynomial fit used to model the local background of the In-115 β spectrum. In the fits shown in Figure 5-14, the StabAmplitude parameter represents a raw pulse amplitude generated by the CUORE OT/OF analysis chain. The main cuts for the data employed for these calibration pulses were multiplicity $= 2$, requiring that the LD and the LIS detector both trigger within 5 ms of each other, a pile-up cut discussed later and that the number of pulses observed in the LIS crystal during a 600 ms window equal 1. These two cuts were designed to ensure that we had a cleanest population of events possible. While these cuts were not optimized to ensure the maximum signal passage fraction, as the statistics available to us in the Barium data sets were much higher than during the typical background running,

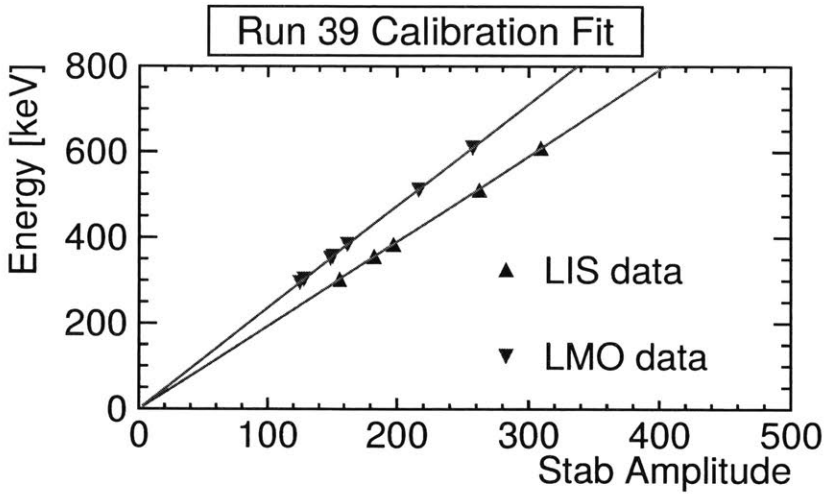

Figure 5-15: Quadratic Calibration Fits

which meant we could be more selective about which peaks to use.

- μ - this corresponds to the mean or the maximum of the Gaussian peak, it is these values that we then fit to when calibrating the detector.

- σ - this corresponds to the width of the fitted Gaussian, throughout this thesis unless otherwise noted when discussing the width of each peak I will discuss the '1-σ' width of the peak not one of its' derivative quantities such as the Full Width Half Maximum (FWHM)

Once we had fitted all the peaks in the barium data, we were able to fit all the respective μ's to a second degree polynomial. To first order the detector response should be linear, however; slight irregularities could induce additional corrective factors summarized in the second order term. One other item to note, while we were fitting the detector response we fixed the y-intercept of our calibration fit to zero to mirror what had been done on CUORE/CUORE-0 analyses. Once we had the calibration fits determined we could then go ahead and calculate the energy resolution of our detectors as a function of energy. The energy resolution would allow us to "smear" out the ideal detector response assumed in the theory calculations of the spectral shape provided to us, discussed more below.

From this data we did not notice any major dependence on the energy resolution

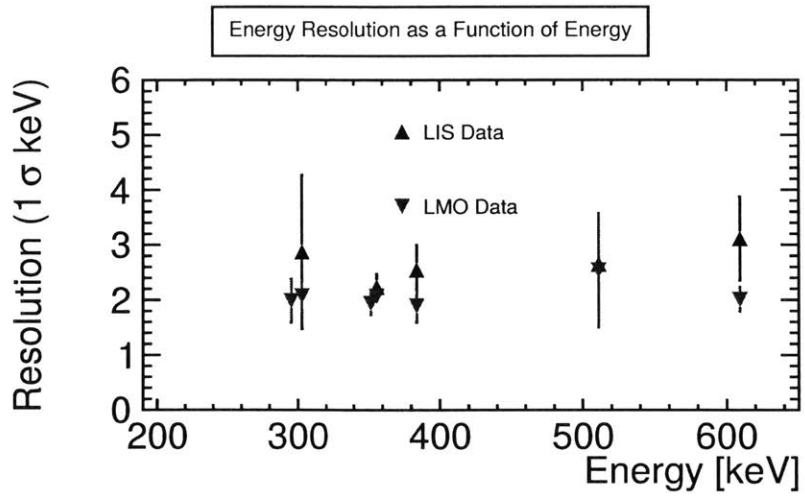

Figure 5-16: LIS and LMO energy resolution, note these values are the 1 σ energy resolutions, LIS average resolution: 2.4 $\pm$ 0.2 keV with LMO average resolution 2.0 $\pm$ 0.1 keV

as a function of energy which allowed us to approximate the detector response as a constant across the energies we are interested in.

5.10 LIS Cut Selection

Once we had the calibration we could then proceed to define a series of data quality cuts, which were designed to pick out specific types of events, such as glitch or pile-ups or ensure that only the best pulses were included in our final fits. All the data quality cuts that we defined here are based on variables derived in the CUORE DIANA software.

5.10.1 Glitch and Pileup

If you were to scan through each individual event collected in our analysis setup, there there would be two population of events that would be easy to pick out based on their pulse shapes, the glitches and pileups (Figure 5-17) Pile up events stem from the the comparatively slow readout times of the LIS crystal coupled with the fact that the LIS crystal is both the source and our detector. Despite the long half-life

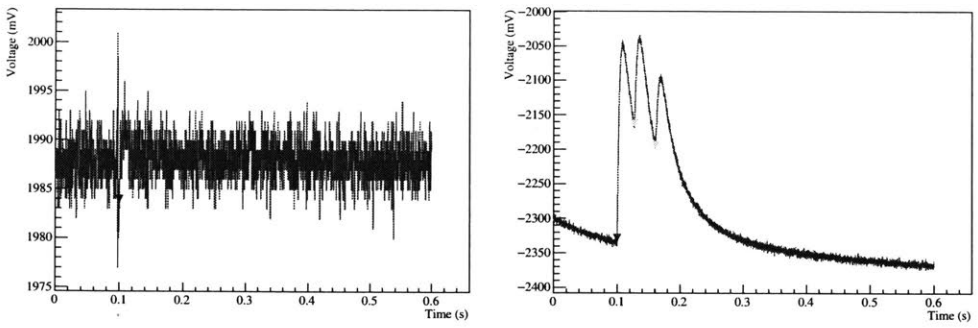

Figure 5-17: (a)Example Glitch Event and (b) Example Pile-up events, the small green arrows represent the CUORE software registering those peaks as individual pulses. Note that this particular event is actually a 4-pulse pileup, the first pulse registers off to the left of the pulse window, as seen by the slope visible in the baseline

associated with highly forbidden In-115 decays (4×10^{14} years), this still results in an overall event rate in our detector of approximately $\approx$ 1 Hz. However; due to the long signal trace recorded by the hardware setup the and slow pulse decay times this means that the majority of our events (51.6 percent) recorded in our detector will have at least one pileup within a 600 ms time window associated with them. These events do not fit the overall template provided by the average pulse, resulting in energy mis-reconstruction, which can distort the overall energy spectrum we are attempting to measure. If the pileup events end up getting too close to each other in time, they can form an irreducible background, which can not be cut with these analysis cuts - see below. For all the other glitch and pileup events, we designed a series of pulse shape variable cuts designed to identify and cut out pile-up events out of the overall LIS event population.

For these pileup/glitch analysis cuts, we opted for using 3 σ cuts on the cut variables as our baseline acceptance rate setting a precedent that we could continue using for optimizing the main analysis cuts. For glitch cuts, the most effective method of singling them out was cutting on a combination of OFRisetime and $\Delta_{Max-Min}$ (defined simply as the difference between the maximum and minimum elements in a pulse) in the pulse window. This particular combination worked well as most of the glitch events fell into a specific amplitude range but the OFRisetime variable would

often mis-reconstruct the overall pulse shape from the average pulse, generally calculating unrealistically short OFRisetimes for the glitch pulses. This meant that glitch pulses occupied a corner of the Risetime-$\Delta_{Max-Min}$ space and we were easily able to define 3σ cuts appropriately. For pileup events, the analysis cut was determined by looking at the ratio the baselineslope/baselineRMS for each event and then defining a 3 σ signal selection cut to select good events. Good events would generally have a baselineslope/baselineRMS value centered around zero, while pileup events would be shewed to more negative values of this ratio.

5.10.2 Main Analysis Cuts

In line with the CUORE-0 low energy/threshold analysis, a series of four data quality parameters; Rise Time, Decay Time, OF Delay and the χ^2 (goodness of fit for the average pulse), were selected to be optimized for use with this analysis. These four variables were chosen to mirror the methodology utilized in the CUORE-0 DM analysis [167]. The four data quality variables shown below were optimized in such as way as to include at a 3 σ level the events contained in each 5 keV energy bin from 0 up to $\approx$ 1000 keV. Beyond these energies, these statistics on the LIS crystal became poor and the cut was defined to include all events. At extremely low energies, below around 10 keV, the cuts were flattened, seen most clearly in the Energy-χ^2 and Energy-Risetime plots below. This was done due to the large spread in the event distributions at these energies, which resulted in fits that included all events and is reflected in the poor cut efficiencies seen at the lowest energies. All these cuts were determined independently, except for the $OF\chi^2$ cut. Once the cuts had been defined for the other pulse shape variables, we then had a population of clean single-pulse events, which were then plotted in Energy-$OF\chi^2$ space, resulting in the drop off in event statistics below 20 keV. Each point in Figure 5-18 represents a single event/pulse superimposed with the analysis cuts in red. We performed a similar cuts-based analysis on the data from the LMO crystal, not shown here. In general, the LMO crystal performed better in terms of energy resolution and noise which allowed to apply the same thresholds to the LMO detector as to the LIS detector, without additional systematic errors.

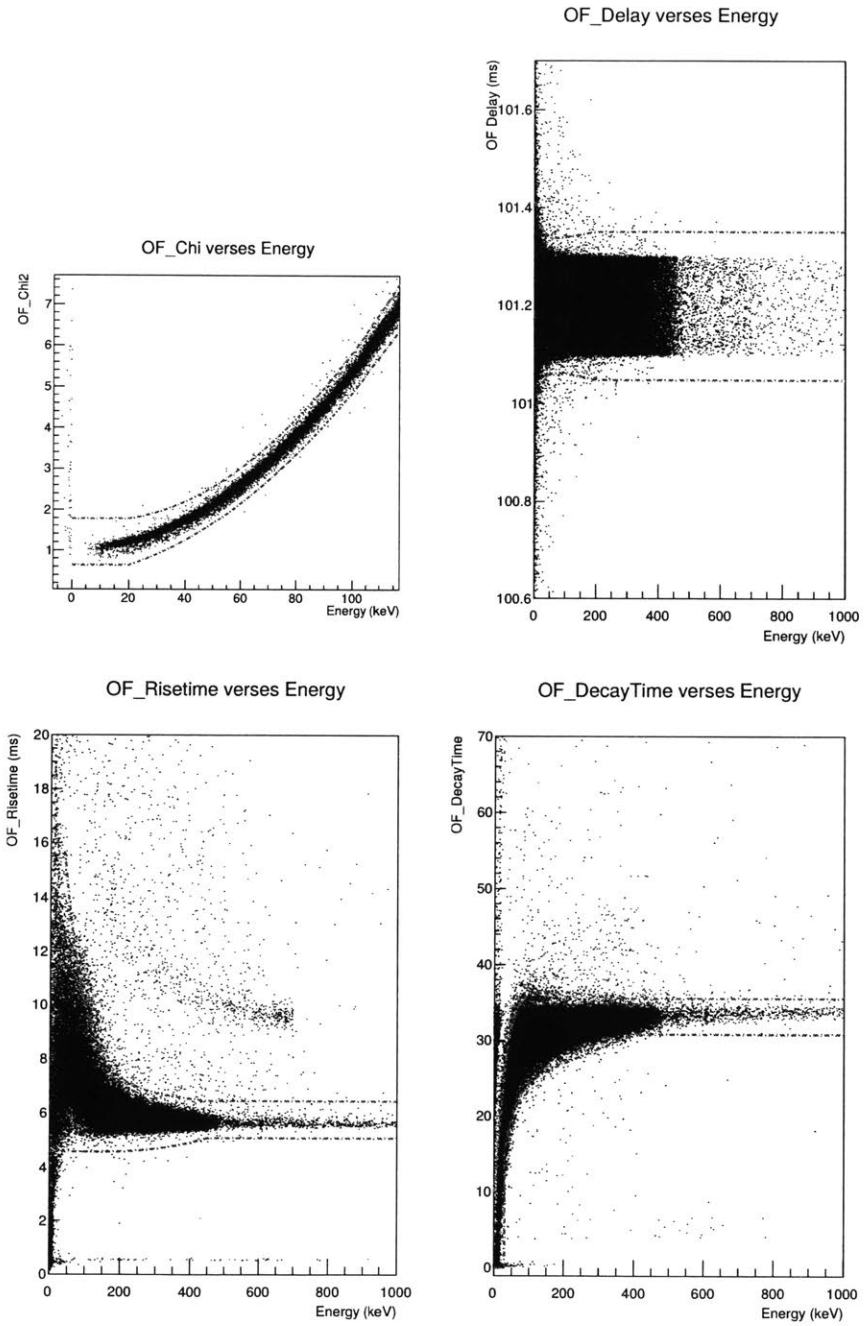

Figure 5-18: The 4 main analysis cuts employed in this data analysis, with the finalized cuts imposed on top of these plots in red. The specifics of why the pulse shape parameters change as a function energy (especially near the noise wall) often boils down to the optimal filter having difficultly in determining the exact start position of the pulse, which then throws off the various pulse shape calculations

5.10.3 Analysis Efficiencies

Within this analysis there are multiple thresholds and efficiencies at work: the crystal absorption efficiency, the physical trigger threshold, the effective analysis threshold outlined below.

- The crystal absorption efficiency represents the probability that if an event between 0 and the 497 keV (the Q value of the In-115 decay) occurs somewhere within your crystal volume that even will then get absorbed within your detector and result in a usable signal. This was tested using a GEANT4 simulation of the LIS crystal, where β events were simulated uniformly between 0 and 750 keV and isotropically throughout the crystal volume. The reason why the efficiency rises above 100 percent at low energies is due to the down-shifting of high energy events into lower energy bins. The simulation simply records the amount of energy deposited in the crystal for each event, but higher energy events can scatter inside your crystal volume and only deposit a fraction of their total energy. The number of events recorded in each energy volume is then recorded - see Figure 5-19.

- The physical trigger threshold corresponds to the probability that smaller and smaller pulses will result in a trigger flag issued by the optimal trigger software. Using the injected pulser events we were able to determine the effective 50 percent trigger threshold as 2 keV using the procedure outlined below - see Figure 5-19 .

- Once the cuts were finalized we test their respective signal passage efficiencies by generating a series of low energy pulse event, scaled from the optimal filter average pulse template event. After scaling these fake pulses to a specific energy value, noise events drawn from data were then added to these scaled pulses to create a series of fake pulses shown in Figure 5-20. With this library of fake pulses generated at specific energy values we were then able to calculate the cut efficiencies for all the cuts we defined earlier. From these efficiencies we were able

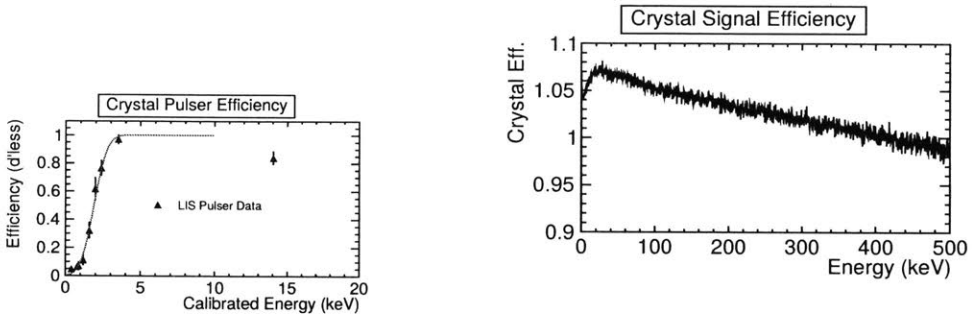

Figure 5-19: Pulser efficiencies (a), defined as the probability that an event will call the analysis chain to register an event. Data shown with error function fit superimposed. The crystal efficiencies(b) is defined as a probability that an event with an initial energy will be recorded as an event with a different energy

to see that the cuts we had defined, for example OFRiseTime, began losing their signal efficiency at around 20 keV, which is what prompted setting our effective analysis threshold at 20 keV. This does not mean that the threshold could not be lowered further, but for this first analysis 20 keV is well above the noise trigger threshold (2 keV) providing a conservative estimate to our threshold and reducing the possible noise wall effects.

In order to calculate the effective LIS physical trigger threshold a series of pulser runs which were run with the following procedure:

- Using a signal generator pulse the LIS crystal through the attached heater element every 5 seconds with a 4 V signal pulse. This amplitude was chosen as during the experimental runs with a 4V signal a clearly visible pulse was seen on the readout electronics. At the same time this signal was used to generate a pulser flag on channel 4 (usually the light collection channel). This pulser flag was used to set an analysis window in the DIANA code that we could then use to determine the overall trigger efficiency (see below)

- After about 4 minutes, the signal generator was run at a smaller voltage, namely xV for up to 15 minute pulsing every 5 seconds. The x was chosen so that the corresponding energy being injected into the LIS detector was linearly decreasing in power assuming that the heater was a perfectly Ohmic resistor at cryogenic

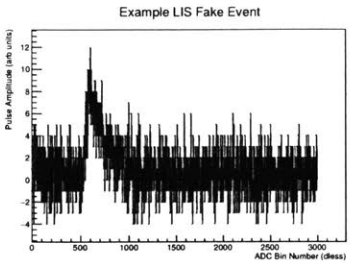

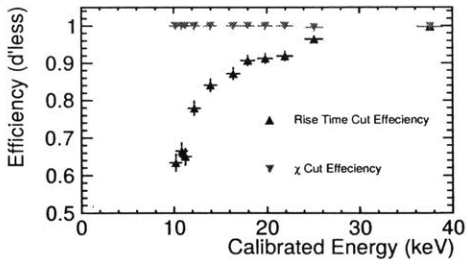

(a) Cut Efficiencies

Figure 5-20: An example fake event scaled to $\approx$ 20 keV (a) used in this analysis. The cut efficiencies were then tested by injecting the various scaled fake pulses into the analysis pipeline and recording the percentage of events that made it out

temperature and at these very low energies.

5.11 MCMC Fitting and Results

Once we have the finalized spectrum that passes all the cuts described above we can generate a In-115 single pulse spectrum that can then be fitted to the library of theoretical models that we obtained from our theory colleagues. The analysis threshold used in this analysis was set at 20 keV, driven by the cut efficiencies described earlier. Our data fitting model was driven by a three component fit outlined below. The first component was the scaling amplitude of the theory spectrum at a given $\lambda = g_A$. The second component was the scaling amplitude of the background spectrum recorded on the LMO crystal, which we used as a stand-in for the background spectrum expected on the LIS crystal. The third component is related to events ms-reconstructed as a single pulse in the LIS crystal, particularly two pulses that occurred very close together in time resulting in them getting reconstructed as a single event. These misreconstructed sum events would have a resulting spectrum beyond the Q-value of the In-115 decay (497 keV). These close pulses were events that no pile up or glitch cut could account for and therefore had to be treated as an irreducible background. From preliminary measurements, we determined the smallest time delay between two pulses that resulted in a misconstruction to a single pulse was about 6 ms. This meant that

given a $\lambda = g_A$ value and its corresponding theoretical spectrum, we would perform the autocorrelation of that spectrum to create the background component we would expect for these events as they now form a background in our spectrum. This also meant that the amplitude of this auto-correlation component was related to the amplitude of the In-115 beta decays based on the frequency of these mis-reconstructed pulses. For each $\lambda = g_A$, the theoretical spectrum and its associated autocorrelation spectrum were then convolved win the the measured energy resolution which was constant in energy. The resulting two parameter fit was then fitted using a Markov Chain Monte Carlo (see section 4.4.1) search at each $\lambda = g_A$ point in our spectral library. The best fit, in terms of likelihood, was then recorded at each $\lambda = g_A$ generating a profile likelihood spectrum across all the values we tested- see second column of Figure 5-21. From these profile likelihood fits I was then able to extract the following best fit and error bar values for each the nuclear models we tested summarized in Table 5.2. The double peak visible in the profile likelihood across all models is due to the similar spectral shapes in all the theoretical models at lower energies see Figure 5-10 (focus on the blue line below 100 keV). This degeneracy in spectral shape is then lifted via the higher energy behavior of the individual spectra.

Nuclear Model	g_A Value	Error
Shell Model	0.83	$\pm$ 0.03 (stat)
MQPM Model	0.94	$^{+0.03}_{-0.04}$ (stat)
IBM Model (region I)	0.880	$\pm$ 0.06 (stat)
IBM Model (region II)	1.22	$\pm$ 0.08 (stat)

Table 5.2: Summary with 1 σ error bars of the final LIS g_A quenching factor results. Note that these numbers are purely statistical errors and do not take into account systematic errors, which will be included in the final analysis

These values seem to point to a quenching factor well below the free decay value measured in neutrons. This will shift all the $0\nu\beta\beta$ published limits up by a factor of ≈ 2.

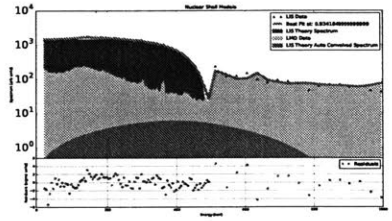

(a) Shell Model Stacked Fits

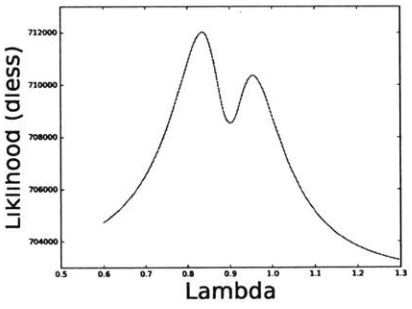

(b) Shell model Liklihoods

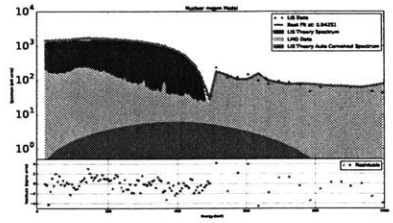

(c) MQPM Model stacked fits

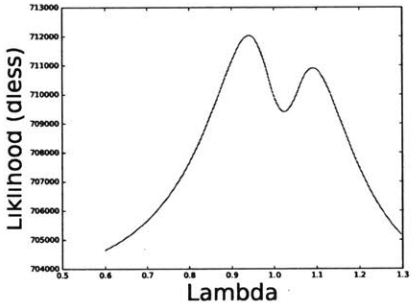

(d) MQPM Model Liklihoods

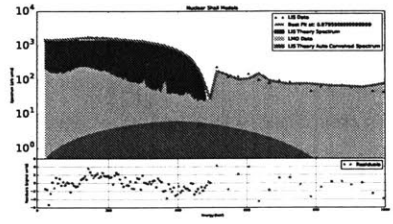

(e) IBM model stacked fits

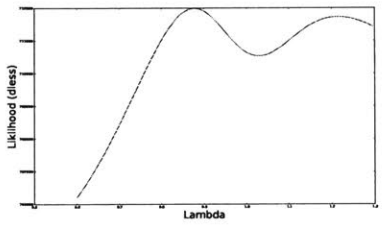

(f) IBM Model Liklihoods

Figure 5-21: The resulting MCMC fits for the LIS theory spectrum (Blue), the LMO background spectrum(Yellow) and the LIS autocorrelation spectrum (green)

5.12 Closing Thoughts

The numbers and analysis presented in this thesis will continued to be improved by the collaboration after this thesis is finished and turned in. These results will be presented at the Neutrino 2018 conference and are on track to be published in the summer of 2018.

Chapter 6

Conclusion

There is no perfect experimental setup that can measure every possible physics signal simultaneously. Each setup must be carefully constructed to maximize the chances of seeing your signal while minimizing any background that could mask it. Rare event searches, such as CDMS, Ricochet and CUORE, have all taken advantage of bolometers. These detectors convert a particle interaction into a readable (by definition heat-based but sometimes with additional light/charge parallel readout channels) signal. In this thesis, we have examined the optimization of three different bolometric detectors with three distinct physics goals: discovery of Dark Matter, exploration of the CEνNS process and the precision measurement of β spectrum in In-115 to verify the nuclear models used to extract a $m_{\beta\beta}$ sensitivity for all neutrino-less double beta decay searches. The measurement of each of these rare phenomena places strict requirements on background, energy resolution, energy threshold and size. Recent advances in cryogenic engineering and nano-fabircation techniques have facilitated the rapid advancement of bolometric detectors and made them a mainstay of rare-event searches. As these technologies continue to evolve, we will have the ability to explore new parameter spaces in physics. It will also open the door to applications with impacts in the "real world". For example, these Ricochet-style detectors offer the exciting possibility of small-scale detectors capable of reactor monitoring via the monitoring of reactor neutrino emission.

With the analyses discussed in this thesis, we have set the stage for rare-event

searches using arrays of bolometers up to the tonne-scale. The operation of voltage assisted calorimetry, such as that used on CDMSlite for reducing the threshold, has worked as a proof-of-concept for lower thresholds on CDMS. This in turn motivated the use of solely CDMSlite-style detectors on proposals for the next generation of CDMS (CDMS-Sudbury), which will focus on scanning over lower mass dark matter models. Low threshold detectors, such as the ones proposed for the Ricochet measurement, would allow for the characterization of coherent neutrino-nucelon scattering thanks to the high neutrino flux found close to the reactor core. However; as discussed in this thesis, this proximity comes at the cost of needing to provide shielding from reactor neutrons as well as mitigating the effect of vibrations induced by your cyrostat system. Finally, the CUPID-LIS analysis demonstrates that a precision physics result, the measurement of the nuclear quenching factor g_A, can be performed with a scintillating bolometer. This measurement of g_A has profound consequences for all current and future neutrino-less double beta decay experiments. While all these examples showcase the great physics reach achievable with bolometers, they also highlight the need for the accurate understanding of all backgrounds in order achieve their maximum sensitivity. To the experiment builders of the future, I wish you good luck.

Bibliography

[1] Kurt Rieseelmann. Weak Neutral Current. *Symmetry Magazine*, pages 1–5, 2009.

[2] Teresa Marrodan Undagoitia and Ludwig Rauch. Dark matter direct-detection experiments. *J. Phys. G*, 43(1), 2016.

[3] S. A. Hertel and M. Pyle. Phonon pulse shape discrimination in SuperCDMS soudan. *Journal of Low Temperature Physics*, 167(5-6):1173–1178, 2012.

[4] P. N. Luke, J. Beeman, F. S. Goulding, S. E. Labov, and E. H. Silver. Calorimetric ionization detector. *Nuclear Inst. and Methods in Physics Research, A*, 289(3):406–409, 1990.

[5] Ritoban Thakur. *The Cyrogenic Dark Matter Search Low Ionization-Threshold Experiment.* PhD thesis, University of California, Berkeley, 2015.

[6] Matt Pyle. *Optimizing the Design and Analysis of Cryogenic Semiconductor Dark Matter Detectors for.* PhD thesis, Stanford University, 2012.

[7] Shin Ichiro Tamura. Spontaneous decay rates of LA phonons in quasi-isotropic solids. *Physical Review B*, 31(4):2574–2577, 1985.

[8] E P N Damen, A F M Arts, and H W De Wijn. Experimental verification of Herring ' s theory of anharmonic phonon relaxation : TeO 2. 59(1):263–4, 1999.

[9] Claude A. Klein. Bandgap dependence and related features of radiation ionization energies in semiconductors. *Journal of Applied Physics*, 39(4):2029–2038, 1968.

[10] Steven H. Simon. *The Oxford Solid State Basics.* Oxford University Press, Oxford, 1st edition, 2013.

[11] J. Dubeau, L. Hamel, and T. Pochet. Radiation ionization energy in a-Si:H. *Physical Review B - Condensed Matter and Materials Physics*, 53(16):10740–10750, 1996.

[12] Glenn F. Knoll. *Radiation Detection and Measurement.* John Wiley & Sons, 4th edition, 2010.

[13] Z. Ahmed, D. S. Akerib, S. Arrenberg, et al. Search for inelastic dark matter with the cdms ii experiment. *Phys. Rev. D*, 83:112002, Jun 2011.

[14] J.D. Lewin and P.F. Smith. Review of mathematics, numerical factors, and corrections for dark matter experiments based on elastic nuclear recoil. *Astroparticle Physics*, 6(1):87–112, dec 1996.

[15] J. Lindhard, V. Nielsen, and M. Scharff. Approximation method in classical scattering by screened coulomb fields. *Kgl. Dan. Vidensk. Selsk., Mat.-Fys. Medd., 36: 31p(1968).*, 1 1968.

[16] C. Ligi, C. Alduino, F. Alessandria, et al. The CUORE Cryostat: A 1-Ton Scale Setup for Bolometric Detectors. *Journal of Low Temperature Physics*, 184(3-4):590–596, 2016.

[17] Jonathan Ouellet. The Coldest Cubic Meter in the Known Universe. pages 2–5, 2014.

[18] M Barucci, C Brofferio, A Giuliani, E Gottardi, I Peroni, and G Ventura. Measurement of Low Temperature Specific Heat of Crystalline TeO 2 for the Optimization of Bolometric Detectors. *Journal of Low Temperature Physics*, 123:303–314, 2001.

[19] Christian Enss and Seigfried Hunklinger. *Low-Temperature Physics.* Springer-Verlag, Berlin, 2005.

[20] W. E. Gifford and R. C. Longsworth. *Advanaces in Cyrogenic Engineering.* 1965.

[21] E. I. Mikulin, A. A. Tarasov, and M. P. Shkrebyonock. *Low-Temperature Expansion Pulse Tubes*, pages 629–637. Springer US, Boston, MA, 1984.

[22] Jingtao Liang, Yuan Zhou, and Wenxiu Zhu. Development of a single-stage pulse tube refrigerator capable of reaching 49 K. *Cryogenics*, 30(1):49–51, 1990.

[23] Takayuki Tomaru, Toshikazu Suzuki, Tomiyoshi Haruyama, Takakazu Shintomi, Akira Yamamoto, Tomohiro Koyama, and Rui Li. Vibration analysis of cryocoolers. *Cryogenics*, 44(5):309–317, 2004.

[24] S. Caparrelli, E. Majorana, V. Moscatelli, E. Pascucci, M. Perciballi, P. Puppo, P. Rapagnani, and F. Ricci. Vibration-free cryostat for low-noise applications of a pulse tube cryocooler. *Review of Scientific Instruments*, 77(9), 2006.

[25] A. M.J. Den Haan, G. H.C.J. Wijts, F. Galli, O. Usenko, G. J.C. Van Baarle, D. J. Van Der Zalm, and T. H. Oosterkamp. Atomic resolution scanning tunneling microscopy in a cryogen free dilution refrigerator at 15 mK. *Review of Scientific Instruments*, 85(3):1–6, 2014.

[26] E. Olivieri, J. Billard, M. De Jesus, A. Juillard, and A. Leder. Vibrations on pulse tube based Dry Dilution Refrigerators for low noise measurements. *Nuclear Instruments and Methods in Physics Research, Section A: Accelerators, Spectrometers, Detectors and Associated Equipment*, 858(December 2016):73–79, 2017.

[27] J. R. Fienup. Phase retrieval algorithms: a comparison. *Appl. Opt.*, 21(15):2758–2769, Aug 1982.

[28] Matt Pyle, Enectali Figueroa-feliciano, and Bernard Sadoulet. Optimized Designs for Very Low Temperature Massive Calorimeters. 2015.

[29] Joseph A. Formaggio, E. Figueroa-Feliciano, and A. J. Anderson. Sterile neutrinos, coherent scattering, and oscillometry measurements with low-temperature bolometers. *Phys. Rev. D*, 85:013009, Jan 2012.

[30] A. J. Anderson, S. W. Leman, E. Figueroa-Feliciano, et al. Simulations of noise in phase-separated transition-edge sensors for superCDMS. *Journal of Low Temperature Physics*, 167(3-4):135–140, 2012.

[31] Andrew Jastram. *CDMS Detector Fabrication Improvements and Low Energy Recoil Measurements in Germanium.* PhD thesis, Texas A&M, 2015.

[32] J. Bardeen, L. N. Cooper, and J. R. Schrieffer. Theory of superconductivity. *Physical Review*, 108(5):1175–1204, 1957.

[33] Michael Tinkham. *Introduction to Superconductivity.* Dover Publications, 2nd edition, 2004.

[34] E. E. Haller, N. P. Palaio, M. Rodder, W. L. Hansen, and E. Kreysa. *NTD Germanium: A Novel Material for Low Temperature Bolometers*, pages 21–36. Springer US, Boston, MA, 1984.

[35] C. Alduino, K. Alfonso, D. R. Artusa, et al. CUORE-0 detector: Design, construction and operation. *Journal of Instrumentation*, 11(7), 2016.

[36] R Lobo, Z Barber, and G L Carr. Photoinduced time-resolved electrodynamics of superconducting metals and alloys. *Physical Review B*, 72(2):1–10, 2005.

[37] C E Aalseth, P S Barbeau, J Colaresi, J Collar, et al. CoGeNT: A Search for Low-Mass Dark Matter using p -type Point Contact Germanium Detectors. 3:1–20, 2013.

[38] C. Alduino, K. Alfonso, D. R. Artusa, et al. The projected background for the CUORE experiment. *European Physical Journal C*, 77(8), 2017.

[39] Norbert Straumann. The history of the cosmological constant problem. pages 1–12, 2002.

[40] Yoshiaki Sofue and Vera Rubin. Rotation Curves of Spiral Galaxies. *Annual Review of Astronomy and Astrophysics*, 39(1):137–174, 2001.

[41] Douglas Clowe, Marusa Bradac, Anthony H. Gonzalez, Maxim Markevitch, Scott W. Randall, Christine Jones, and Dennis Zaritsky. A direct empirical proof of the existence of dark matter. *The Astrophysical Jounal*, 648:L109–L113, 2006.

[42] A. A. Penzias and R. W. Wilson. A Measurement of Excess Antenna Temperature at 4080 Mc/s. *apj*, 142:419–421, July 1965.

[43] R. H. Dicke, P. J. E. Peebles, P. G. Roll, and D. T. Wilkinson. Cosmic Black-Body Radiation. *apj*, 142:414–419, July 1965.

[44] Planck Collaboration. Astrophysics Special feature Planck 2015 results. *Astronomy & Astrophysics*, 13:1–39, 2016.

[45] C. Patrignani et al. Review of Particle Physics. *Chin. Phys.*, C40(10):100001, 2016.

[46] Adam Anderson. *A Search for Light Weakly-Interacting Massive Particles with SuperCDMS and Applications to Neutrino Physics.* PhD thesis, 2015.

[47] Steven Weinberg. *Cosmology.* Oxford University Press, Oxford, 1st edition, 2008.

[48] Adam G. Riess, Alexei V. Filippenko, Peter Challis, et al. Observational Evidence from Supernovae for an Accelerating Universe and a Cosmological Constant. *The Astrophysical Journal*, 116:1009–1038, 1998.

[49] Jonathan L. Feng. Dark Matter Candidates from Particle Physics and Methods of Detection. *Annual Review of Astronomy and Astrophysics*, 48:495–547, 2010.

[50] John Ellis, J. S. Hagelin, D. V. Nanopoulos, K. Olive, and M. Srednicki. Supersymmetric relics from the big bang. *Nuclear Physics, Section B*, 238(2):453–476, 1984.

[51] Gianfranco Bertone, editor. *Particle Dark Matter: Observations, Models and Searches.* Cambridge University Press, Cambridge, 2010.

[52] Tansu Daylan, Douglas P. Finkbeiner, Dan Hooper, et al. The characterization of the gamma-ray signal from the central Milky Way: A case for annihilating dark matter. *Physics of the Dark Universe*, 12:1–23, 2016.

[53] M Drees and G Gerbier. PDG Review: Dark Matter. Technical Report December, 2017.

[54] Yao Yuan Mao, Louis E. Strigari, and Risa H. Wechsler. Connecting direct dark matter detection experiments to cosmologically motivated halo models. *Physical Review D - Particles, Fields, Gravitation and Cosmology*, 89(6):39–41, 2014.

[55] R. Agnese, A. J. Anderson, T. Aralis, et al. Low-mass dark matter search with CDMSlite. *Physical Review D*, 97(2):22002, 2018.

[56] Sunil Ramanlal Golwala. *Exclusion Limits on the WIMP-Nucleon Elastic-Scattering Cross Section from the Cryogenic Dark Matter Search.* PhD thesis, University of California at Berkeley, 200.

[57] D. S. Akerib, S. Alsum, H. M. Araújo, et al. Results from a Search for Dark Matter in the Complete LUX Exposure. *Physical Review Letters*, 118(2):1–8, 2017.

[58] R. Agnese, A. J. Anderson, T. Aramaki, et al. Projected sensitivity of the SuperCDMS SNOLAB experiment. *Physical Review D*, 95(8):1–17, 2017.

[59] D. S. Akerib et al. Projected WIMP sensitivity of the LUX-ZEPLIN (LZ) dark matter experiment. 2018.

[60] J. Billard, E. Figueroa-Feliciano, and L. Strigari. Implication of neutrino backgrounds on the reach of next generation dark matter direct detection experiments. *Phys. Rev. D*, 89:023524, Jan 2014.

[61] D. Akimov et al. Observation of coherent elastic neutrino-nucleus scattering. *Science*, 2017.

[62] Daniel Z. Freedman. Coherent effects of a weak neutral current. *Physical Review D*, 9(5):1389–1392, 1974.

[63] K. G. Balasi, K. Langanke, and G. Martínez-Pinedo. Neutrino-nucleus reactions and their role for supernova dynamics and nucleosynthesis. *Progress in Particle and Nuclear Physics*, 85:33–81, 2015.

[64] Irene Tamborra. Supernova Neutrinos : New Challenges and Future Directions Supernova Neutrinos : New Challenges and Future Directions. In *Journal of Physics: Conference Series*, volume 888, 2017.

[65] B. Müller, T. Melson, A. Heger, and H. Th. Janka. Supernova Simulations from a 3D Progenitor Model – Impact of Perturbations and Evolution of Explosion Properties. 513(May 2018):491–513, 2017.

[66] Adam Burrows. Colloquium: Perspectives on core-collapse supernova theory. *Reviews of Modern Physics*, 85(1):245–261, 2013.

[67] C. J. Horowitz, K J Coakley, and D. N. McKinsey. Supernova observation via neutrino-nucleus elastic scattering in the CLEAN detector. *Physical Review D*, 68(2):1–7, 2003.

[68] J. Billard, L. E. Strigari, and E. Figueroa-Feliciano. Solar neutrino physics with low-threshold dark matter detectors. *Physical Review D - Particles, Fields, Gravitation and Cosmology*, 91(9):1–13, 2015.

[69] Juan Barranco, Omar G. Miranda, and Timur I. Rashba. Probing new physics with coherent neutrino scattering off nuclei. *Journal of High Energy Physics*, 12(12):425–438, 2005.

[70] J. Barranco, O. G. Miranda, and T. I. Rashba. Sensitivity of low energy neutrino experiments to physics beyond the standard model. *Physical Review D - Particles, Fields, Gravitation and Cosmology*, 76(7):1–9, 2007.

[71] J. Schechter and J. W F Valle. Neutrino masses in SU(2) U(1) theories. *Physical Review D*, 22(9):2227–2235, 1980.

[72] V. Barger, G. F. Giudice, and T. Han. Some new aspects of supersymmetry R-parity violating interactions. *Physical Review D*, 40(9):2987–2996, 1989.

[73] D. K. Papoulias and T. S. Kosmas. Neutrino transition magnetic moments within the non-standard neutrino-nucleus interactions. *Physics Letters, Section B: Nuclear, Elementary Particle and High-Energy Physics*, 747:454–459, 2015.

[74] Julien Billard, Joesph Johnston, and Bradley Kavanagh. Prospects for exploring New Physics in Coherent Elastic Neutrino-Nucleus Scattering with the Ricochet experiment. *ArXiv preprint*, 5:1–35, 2018.

[75] G. P. Zeller, K. S. McFarland, T. Adams, et al. Precise Determination of Electroweak Parameters in Neutrino-Nucleon Scattering. *Physical Review Letters*, 88(9):4, 2002.

[76] Kelly M. Patton, Gail C. McClaughlin, and Kate Scholberg. Prospects for using coherent elastic neutrino-nucleus scattering to measure the nuclear neutron form factor. *International Journal of Modern Physics E*, 22(06):1330013, 2013.

[77] Vedran Brdar, Patrick Huber, and Joachim Kopp. Antineutrino Monitoring of Spent Nuclear Fuel. *Physical Review Applied*, 8(5):6–11, 2017.

[78] Eric Christensen, Patrick Huber, Patrick Jaffke, and Thomas E. Shea. Antineutrino monitoring for heavy water reactors. *Physical Review Letters*, 113(4):1–5, 2014.

[79] P S Barbeau, J I Collar, and O Tench. Large-mass Ultralow Noise Germanium Detectors: Performance and Applications in Neutrino and Astroparticle Physics. *Journal of Cosmology and Astroparticle Physics*, 2007(09):9, 2007.

[80] Henry Tsz-King Wong. The TEXONO Research Program on Neutrino and AstroParticle Physics. *Modern Physics Letters A*, 19(13n16):1207–1214, 2004.

[81] L. D. P. King and Louis Goldstein. The Total Cross Section of the He-3 Nucleus for Slow Neutrons. *Phys. Rev.*, 75:1366–1369, May 1949.

[82] E Newmann. Neutron Backgrounds in the Ricochet Experiment. Master's thesis, Massachusetts Institute of Technology, 77 Massaschusetts Avenue, Cambridge, MA 02139, May 2016.

[83] John Allison et al. Geant4 Developments and Applications. *IEEE Trans. Nucl. Sci.*, 53:270, 2006.

[84] R G H Robertson. Progress in Particle and Nuclear Physics Neutral-Current Detection via He-3(n,p) H-3 in the Sudbury Neutrino Observatory. *Progress in Particle and Nuclear Physics*, 6410(98):113–121, 1998.

[85] G. Hale, D. Dodder, and P. Young. ENDF/B-VII.1: Nuclear Data for Science and Technology: Cross Sections, Covariances, Fission Product Yields and Decay Data. *Nuclear Data Sheets*, 112:2887, 2011.

[86] James F. Ziegler, M.D. Ziegler, and J.P. Biersack. SRIM – The Stopping and Range of Ions in Matter. *Nucl. Instrum. Meth.*, B268:1818 – 1823, 2010.

[87] B. Beltran et al. Full simulation of the Sudbury Neutrino Observatory proportional counters. *New J. Phys.*, 13:073006, 2011.

[88] Eli. Grushka. Characterization of exponentially modified gaussian peaks in chromatography. *Analytical Chemistry*, 44(11):1733–1738, 1972. PMID: 22324584.

[89] Hok Seum Wan Chan Tseung. *Simulation of the Sudbury Neutrino Observatory Neutral Current Detectors.* PhD thesis, University of Oxford, 2008.

[90] S. N. Axani, J. M. Conrad, and C. Kirby. The desktop muon detector: A simple, physics-motivated machine- and electronics-shop project for university students. *American Journal of Physics*, 85(12):948–958, 2017.

[91] Edoardo Pasca, Emiliano Olivieri, Guglielmo Ventura, et al. *Low Temperature Properities of NTD Ge: Best Choice for CUORE Experiment*, pages 93–97. World Scientific, 2003.

[92] A. J. Anderson, J. M. Conrad, E. Figueroa-Feliciano, C. Ignarra, et al. Measuring active-to-sterile neutrino oscillations with neutral current coherent neutrino-nucleus scattering. *Physical Review D - Particles, Fields, Gravitation and Cosmology*, 86(1):1–11, 2012.

[93] Marcus H. Mendenhall and Robert A. Weller. An algorithm for computing screened coulomb scattering in geant4. *Nucl. Instrum. Meth.*, B227:420–430, 2005.

[94] Wouter Verkerke and David P. Kirkby. The RooFit Toolkit for Data Modeling. *eConf*, C0303241:MOLT007, 2003. [,186(2003)].

[95] J. Billard, F. Mayet, and D. Santos. Markov chain monte carlo analysis to constrain dark matter properties with directional detection. *Phys. Rev. D*, 83:075002, Apr 2011.

[96] J Billard, R Carr, J Dawson, E Figueroa-Feliciano, J A Formaggio, J Gascon, S T Heine, M De Jesus, J Johnston, T Lasserre, A Leder, K J Palladino, V Sibille, M Vivier, and L Winslow. Coherent Neutrino Scattering with Low Temperature Bolometers at Chooz Reactor Complex. *Journal of Physics G: Nuclear and Particle Physics*, 44(10):105101, 2017.

[97] E. Armengaud, Q. Arnaud, C. Augier, et al. Constraints on low-mass WIMPs from the EDELWEISS-III dark matter search. *Journal of Cosmology and Astroparticle Physics*, 2016(5):019–019, may 2016.

[98] V. Tomasello, M. Robinson, and V.A. Kudryavtsev. Radioactive background in a cryogenic dark matter experiment. *Astroparticle Physics*, 34(2):70 – 79, 2010.

[99] D. Dietrich. *Studying the Muon Background Component in the Double Chooz Experiment.* PhD thesis, University of Tübingen, 2013.

[100] A. Aab, P. Abreu, M. Aglietta, et al. The Pierre Auger Cosmic Ray Observatory. *Nuclear Instruments and Methods in Physics Research, Section A: Accelerators, Spectrometers, Detectors and Associated Equipment*, 798:172–213, 2015.

[101] O Horn. *Simulations of the Muon-Induced Neutron Background of the EDELWEISS-II Experiment for Dark Matter Search.* PhD thesis, Karlsruher Insitut fuer Technologie, 2008.

[102] D-M Mei and A. Hime. Muon-induced background study for underground laboratories. *Physical Review D - Particles, Fields, Gravitation and Cosmology*, 73(5):1–18, 2006.

[103] S. Agostinelli et al. Geant4a simulation toolkit. *Nuclear Instruments and Methods in Physics Research Section A: Accelerators, Spectrometers, Detectors and Associated Equipment*, 506(3):250 – 303, 2003.

[104] Thiago Junqueira de Castro Bezerra. *Double Chooz and Reactor Neutrino Oscillation.* 2015.

[105] Maury Goodman Thierry Lasserre. Double Chooz, A Search for the Neutrino Mixing Angle theta-13. *Search*, 2006(2008):162, 2006.

[106] T. Abrahão, H. Almazan, J. C. Dos Anjos, et al. Cosmic-muon characterization and annual modulation measurement with Double Chooz detectors. *Journal of Cosmology and Astroparticle Physics*, 2017(2), 2017.

[107] A. Baldini, C. Bemporad, M. Grassi, S. Parlati, G. Pieri, R. Pazzi, F. Cei, D. Nicolo, E. Caffau, P. Cristaudo, G. Giannini, and Y. Zhang. Geology at the Chooz site. Technical report, INFN - Department of Physics University of Pisa, 1995.

[108] Frederic Boulvain and Noel Vandenberghe. An Introduction to the Geology of Belgium and Luxembourg. In Alain Demoulin, editor, *Landscapes and Landforms of Belgium and Luxembourg*, number 2, chapter 2, pages 9–34. Springer-Verlag, 2018.

[109] E. I. Esch, T. J. Bowles, A. Hime, A. Pichlmaier, R. Reifarth, and H. Wollnik. The cosmic ray muon flux at WIPP. *Nuclear Instruments and Methods in Physics Research, Section A: Accelerators, Spectrometers, Detectors and Associated Equipment*, 538(1-3):516–525, 2005.

[110] D. M. Mei, C. Zhang, and A. Hime. Evaluation of (alpha, n) induced neutrons as a background for dark matter experiments. *Nuclear Instruments and Methods in Physics Research, Section A: Accelerators, Spectrometers, Detectors and Associated Equipment*, 606(3):651–660, 2009.

[111] Alfred Tang, Glenn Horton-Smith, Vitaly A. Kudryavtsev, and Alessandra Tonazzo. Muon simulations for Super-Kamiokande, KamLAND, and CHOOZ. *Physical Review D - Particles, Fields, Gravitation and Cosmology*, 74(5):1–14, 2006.

[112] Joseph A. Formaggio and C.J. Martoff. Backgrounds To Sensitive Experiments Underground. *Annual Review of Nuclear and Particle Science*, 54(1):361–412, 2004.

[113] Masaki Ishitsuka. New results of double chooz. 51st Rencontres de Moriond, 2016.

[114] Anatael Cabrera. Double chooz improved multi-detector measurements. EP Seminar (CERN), 2016.

[115] Alfred Tang, Glenn Horton-Smith, Vitaly A. Kudryavtsev, and Alessandra Tonazzo. Muon simulations for Super-Kamiokande, KamLAND, and CHOOZ. *Physical Review D - Particles, Fields, Gravitation and Cosmology*, 74(5):1–14, 2006.

[116] J. A. Formaggio and C. J. Martoff. Backgrounds to sensitive experiments underground. *Ann. Rev. Nucl. Part. Sci.*, 54:361–412, 2004.

[117] C L Cowan, F Reines, F B Harris, H W Kruse, and A D Mcgu. Detection of the Free Neutrino : a Confirmation. *Science*, 124(3212):103–104, 1956.

[118] M. C. Gonzalez-Garcia and Yosef Nir. Neutrino masses and mixing: Evidence and implications. *Reviews of Modern Physics*, 75(2):345–402, 2003.

[119] B. T. Cleveland, T. Daily, R. Davis, et al. Measurement of the Solar Electron Neutrino Flux with the Homestake Chlorine Detector. *The Astrophysical Jounal*, 496(1-3):505–526, 1998.

[120] Q. R. Ahmad, R. C. Allen, T. C. Andersen, et al. Measurement of the Rate of Solar Neutrinos at the Sudbury Neutrino Observatory. *Physical Review Letters*, 87(7):071301, Jul 2001.

[121] K Eguchi, S Enomoto, K Furuno, et al. First Results from KamLAND: Evidence for Reactor Antineutrino Disappearance. *Physical Review Letters*, 90(2):021802, 2003.

[122] A. Gando, Y. Gando, K. Ichimura, et al. Constraints on θ_{13} from a three-flavor oscillation analysis of reactor antineutrinos at KamLAND. *Physical Review D - Particles, Fields, Gravitation and Cosmology*, 83(5):1–11, 2011.

[123] B. Pontecorvo. Inverse beta processes and nonconservation of lepton charge. *Sov. Phys. JETP*, 7:172–173, 1958. [Zh. Eksp. Teor. Fiz.34,247(1957)].

[124] Ziro I Maki, Masami Nakagawa, and Shoichi Sakata. Remarks on the Unified Model of Elementary Particles. *Progress of Theoretical Physics*, 28(5):870–880, 1962.

[125] Boris Kayser. *Neutrino Mass, Mixing, and Flavor Change*, pages 1–24. Springer Berlin Heidelberg, Berlin, Heidelberg, 2003.

[126] G. Pagliaroli, F. Rossi-Torres, and F. Vissani. Neutrino mass bound in the standard scenario for supernova electronic antineutrino emission. *Astroparticle Physics*, 33(5-6):287–291, 2010.

[127] G. Drexlin, V. Hannen, S. Mertens, and C. Weinheimer. Current direct neutrino mass experiments. *Advances in High Energy Physics*, 2013:1–66, 2013.

[128] A Osipowicz, H Bluemer, and Et al. KATRIN: A next generation tritium beta decay experiment with sub-eV sensitivity for the electron neutrino mass. Technical report, 2001.

[129] Hitoshi Murayama. Hitoshi Murayama, 2018.

[130] Manoj Kaplinghat, Lloyd Knox, and Yong-Seon Song. Determining Neutrino Mass from the Cosmic Microwave Background Alone. *Physical Review Letters*, 91(2):241301, 2003.

[131] Wayne Hu, Daniel J. Eisenstein, and Max Tegmark. Weighing neutrinos with galaxy surveys. *Physical Review Letters*, 80(24):5255–5258, 1998.

[132] Julien Lesgourgues and Sergio Pastor. Neutrino cosmology and Planck. *New Journal of Physics*, 16, 2014.

[133] M. Goeppert-Mayer. Double beta-disintegration. *Physical Review*, 48(6):512–516, 1935.

[134] W C Haxton and G J Stephenson Jr. Double beta decay. *Progress in Particle and Nuclear Physics*, 12(0):409–479, 1984.

[135] A S Barabash, V I Umatov, F Hubert, and P Hubert. New limits on the beta beta decay of Te-130 to excited states of Xe-130. *Eur. Phys. J.*, A11:143, 2001.

[136] H Primakoff and S Rosen. Double Beta Decay. *Report on Progress in Physics*, 22(1221), 1959.

[137] W. H. Furry. On transition probabilities in double beta-disintegration. *Physical Review*, 56(12):1184–1193, 1939.

[138] Simone Marcocci, Matteo Viel, and Francesco Vissani. Neutrinoless double beta decay: 2015 review. *Advances in High Energy Physics*, 2016:1–39, 2016.

[139] M. Goldhaber, L. Grodzins, and A. W. Sunyar. Helicity of neutrinos. *Physical Review*, 109(3):1015–1017, 1958.

[140] Lee Grodzins. The Tabletop Measurement of the Helicity of the Neutrino. *Nuclear Physics B - Proceedings Supplements*, 229-232:5–13, 2012.

[141] K. N. Abazajian, M. A. Acero, S. K. Agarwalla, et al. Light Sterile Neutrinos: A White Paper. 2012.

[142] A. S. Barabash. Average and recommended half-life values for two-neutrino double beta decay. *Nuclear Physics A*, 935:52–64, 2015.

[143] Oliver K Manuel. Geochemical measurements of double-beta decay. *Journal of Physics G: Nuclear and Particle Physics*, 17(S221), 1991.

[144] C. Alduino, K. Alfonso, D. R. Artusa, et al. Measurement of the Two-Neutrino Double Beta Decay Half-life of Te-130 with the CUORE-0 Experiment. 2016.

[145] Atsumichi Kawashima, Kazuya Takahashi, and Akimasa Masuda. Geochemical estimation of the half-life for the double beta decay of Zr96. *Physical Review C*, 47(6):2452–2456, 1993.

[146] J. Argyriades, R. Arnold, C. Augier, et al. Measurement of the two neutrino double beta decay half-life of Zr-96 with the NEMO-3 detector. *Nuclear Physics A*, 847(3-4):168–179, 2010.

[147] A. Gando, Y. Gando, T. Hachiya, et al. Search for Majorana Neutrinos Near the Inverted Mass Hierarchy Region with KamLAND-Zen. *Physical Review Letters*, 117(8):1–6, 2016.

[148] J. Barea, J. Kotila, and F. Iachello. Nuclear matrix elements for double beta decay. *Physical Review C*, 87(1):014315, 2013.

[149] Delia Tosi. The search for neutrino-less double-beta decay: summary of current experiments. In *Proceedings, 14th ICATPP Conference on Astroparticle, Particle, Space Physics and Detectors for Physics Applications (ICATPP 2013): Como, Italy, September 23-27, 2013*, pages 304–314, 2014.

[150] J. Kotila and F. Iachello. Phase-space factors for double-β decay. *Physical Review C*, 85(3):034316, mar 2012.

[151] F. Šimkovic, G. Pantis, J. D. Vergados, and Amand Faessler. Additional nucleon current contributions to neutrinoless double beta decay. *Physical Review C - Nuclear Physics*, 60(5):14, 1999.

[152] Jouni Suhonen. Value of the axial-vector coupling strength in β decays: A review. 5(November):1–35, 2017.

[153] Jouni Suhonen. Impact of the quenching of gA on the sensitivity of $0\nu\beta\beta$ experiments. *Physical Review C*, 96(5):1–5, 2017.

[154] Juhani Hyvärinen and Jouni Suhonen. Analysis of the Intermediate-State Contributions to Neutrinoless Double β - Decays. *Advances in High Energy Physics*, 2016, 2016.

[155] Jonathan Engel and Javier Menéndez. Status and Future of Nuclear Matrix Elements for Neutrinoless Double-Beta Decay: A Review. *Reports on Progress in Physics*, 80(4):1–35, 2016.

[156] E. Caurier, F. Nowacki, a. Poves, and J. Retamosa. Shell Model Study of the Double Beta Decays of Ge-76,Se-82 and Xe-136. *Physics Review Letters*, pages 82–85, 1996.

[157] A Arima and F Iachello. Collective Nuclear States as Representations of a SU(6) Group. *Physical Review Letters*, 35(16):874–877, 1975.

[158] N. Yoshida and F. Iachello. Two-neutrino double-β decay in the interacting boson-fermion model. *Progress of Theoretical and Experimental Physics*, 2013(4):1–25, 2013.

[159] Michel Baranger. Extension of the shell model for heavy spherical nuclei. *Physical Review*, 120(3):957–968, 1960.

[160] M. Haaranen, P. C. Srivastava, and J. Suhonen. Forbidden nonunique beta decays and effective values of weak coupling constants. *Physical Review C*, 93(3):034308, 2016.

[161] M. Haaranen, J. Kotila, and J. Suhonen. Spectrum-shape method and the next-to-leading-order terms of the β -decay shape factor. *Physical Review C*, 95(2), 2017.

[162] Loren Pfeiffer, Allen P. Mills, E. A. Chandross, and T. Kovacs. Beta spectrum of ^{115}In. *Phys. Rev. C*, 19:1035–1041, Mar 1979.

[163] Michael Schieber, R.B. James, and T.E. Schlesinger. Chapter 15 - summary and remaining issues for room temperature radiation spectrometers. In T.E. Schlesinger and Ralph B. James, editors, *Semiconductors and Semimetals*, volume 43 of *Semiconductors and Semimetals*, pages 561 – 583. Elsevier, 1995.

[164] F.A. Danevich, V.Ya. Degoda, L.L. Dulger, L. Dumoulin, A. Giuliani, et al. Growth and characterization of a $Li_2Mg_2(MoO_4)_3$ scintillating bolometer. *Nuclear Instruments and Methods in Physics Research Section A: Accelerators, Spectrometers, Detectors and Associated Equipment*, 889:89 – 96, 2018.

[165] C. Alduino, K. Alfonso, D. R. Artusa, et al. Low Energy Analysis Techniques for CUORE. *European Physical Journal C*, 77(857), 2017.

[166] S. Di Domizio, F. Orio, and M. Vignati. Lowering the energy threshold of large-mass bolometric detectors. *Journal of Instrumentation*, 6(2), 2011.

[167] Gabriele Piperno. Trigger and Analysis Tools for Dark Matter Search in CUORE-0. *Physics Procedia*, 61:759–765, 2015.